SCUOLA DI DOTTORATO
UNIVERSITÀ DEGLI STUDI DI MILANO-BICOCCA

Department of Materials Science

PhD program in Materials Science and Nanotechnology
Cycle XXXIV

Self-Assembly of Nanoparticles in Rubber Nanocomposites

Tripaldi Laura

Registration number: 847018

Tutor: Dr. Barbara Di Credico

Industrial supervisor: Dr. Luca Giannini

Coordinator: Prof. Marco Bernasconi

ACADEMIC YEAR 2020/2021

The only way to find a larger vision
is to be somewhere in particular.

Donna Haraway

Contents

Glossary

APTES	3-aminopropyltriethoxysilane
ATR-FTIR	Attenuated Total Reflection Fourier-Transform Infrared
BET	Brunauer-Emmett-Teller
BR	Butadiene Rubber
CBS	N-cyclohexyl-2-benzothiazole sulphenamide
CHNS	Elemental analysis
CPMAS	Cross-Polarization Magic Angle Spinning
HNP	Hairy Nanoparticle
LAOS	Large Amplitude Oscillatory Shear
MacroSil	Silane-terminated polybutadiene
NC	Nanocomposite
NMR	Nuclear Magnetic Resonance
NP	Nanoparticle
NR	Nanorod
PB	Polybutadiene
PP	Polypropylene

PS	Polystyrene
RPA	Rubber Process Analyzer
SAXS	Small Angle X-Ray Scattering
SBR	Styrene-butadiene rubber
SiO_2-ST	Stöber silica
SiO_2-APTES	APTES-functionalized silica
SiO_2-HNP_X	PB-grafted silica HNPs with X wt% PB
SiO_2-PS_HNP	PS-grafted silica HNPs
SiO_2-PP_HNP	PP-grafted silica HNPs
SiO_2-Y/SBR	Ex-situ rubber NC with Y=ST, APTES, HNP_X
SiO_2-TSX/SBR	In-situ rubber NC with X % MacroSil grafting density
SSA	Specific Surface Area
TEM	Transmission Electron Microscopy
TEOS	Tetraethoxysilane
TESPT	Bis[3-(triethoxysilyl)propyl] tetrasulfide
THF	Tetrahydrofuran
V-	Vulcanized at 170 °C for 30 min
V10-	Vulcanized at 170 °C for 10 min

Preface

Introduction and aims

i. Introduction

The addition of inorganic nanoparticles (NPs) to polymer matrices is one of the most promising strategies to produce materials with improved functional properties not displayed by the individual phases. These materials, known as polymer nanocomposites (PNCs), find their application in a variety of different fields, from mechanical reinforcement[1] to dielectrics,[2] from catalysis[3] to medical devices.[4] Among PNC, rubber NCs are widely used in tyres, where mechanical properties result from the synergetic interactions between polymer chains and reinforcing filler NPs, such as silica and carbon black.

Generally, the main issue concerning rubber NCs is the dispersion of the inorganic NPs within the polymer matrix, as well as the effective filler-rubber interaction, since inorganic NPs are hydrophilic, while polymer matrices are mostly nonpolar and hydrophobic. Typically, inorganic NPs, such as silica NPs, are chemically modified to anchor small organic molecules, also known as coupling agents, onto their surface. This chemical modification favors the dispersion of filler within the hydrophobic rubber by improving filler/matrix compatibility.

However, recently the functionalization of inorganic NPs with macromolecules, such as polymer chains, has attracted increasing attention as promising alternative to the well-established approach.[5–7] Hairy Nanoparticles (HNPs) are a class of hybrid NPs functionalized with polymer chains which can be designed for a variety of different applications, such as drug nanocarriers, smart materials and catalysts.[5] In the context of PNCs, HNPs can strongly improve filler/matrix interactions. Furthermore, it has been established that HNPs, although spherical, can self-organize within polymer matrices to produce ordered anisotropic structures, thus offering accurate control of filler

distribution. This self-assembly behavior, usually ascribable to anisotropic particles, can result in strongly improved mechanical and functional properties. With respect to this, while it has been exhaustively demonstrated that anisotropic NPs, like rod-like silica[8] and silicate nanofibers[9–12] in polymeric materials, are able to produce oriented and anisotropic filler assemblies, like sheets, vesicles, percolating clusters,[1,9,13] the control of both the spatial dispersion and distribution of spherical NPs in PNCs remains an open issue to investigate.

The impact of filler self-organization on the mechanical properties of rubber NCs has been the subject of in-depth investigation, particularly for tyre applications.[14–16] In fact, it has been demonstrated that, beside the hydrodynamic effect due to filler volume fraction, the reinforcement mechanism is strongly related to the filler network structure. In a given range of particle loading, filler NPs give rise to interconnected structures, through both direct interactions between NPs and their bridging by polymer chains, which enable the material to support large dynamic loads over millions of load cycles. Thus, the properties of such materials are strongly dependent not only on the geometrical characteristics of the NPs, such as size and shape, and the effective dispersion of the inorganic component, but also on the interfacial interactions between polymer and NPs and, overall, on the control of the morphology of NPs organization at the local scale within the NC. To design advanced rubber materials suitable for tyre applications, the reinforcement effect should go hand in hand with the formation of an extended percolative network, a good filler dispersion and distribution, and an effective interaction of NPs with rubber, producing filler network structures. This has important technical implications on the dynamic loading of tyre materials, especially for the reduction of rolling resistance (the mechanical energy converted

into heat by the tyre moving on the roadway), directly linked to fuel efficiency and emission reduction.

Consequently, despite the performing and established use of silica as a reinforcing filler in rubber NCs, the main challenge of the tyre industry is to identify possible design strategies and alternative fillers to improve the material reinforcement and reduce energy dissipation and rolling resistance. This allows simultaneously to reduce the environmental impact throughout the life cycle of the tyre, reducing energy consumption and CO_2 emissions. It has been demonstrated that the energy dissipated by the rubber in tyres is one of the main contributors to the CO_2 emissions of vehicles, amounting to more than 20% of the total carbon footprint from road transport. Furthermore, issues of durability and wear resistance, associated with environmental pollution and leaching of hazardous chemicals, have also been the focus of recent research in the field.[17]

Taking these issues into consideration, SiO_2 HNPs could be used as innovative fillers in rubber NCs as promising alternative to traditional fillers, by exploiting their self-organization capability in order to further improve reinforcement and simultaneously reduce the material energy dissipation associated with hysteresis effects occurring during deformation, and in turn increasing the lifetime of tyres and reducing abrasion during use.

ii. Aim of the Thesis

In this scenario, the aim of the Thesis was:

i) the development of an efficient synthesis of SiO_2 HNPs having tunable size, controlled morphology, and tailored surface chemistry.

ii) the preparation of rubber NCs based on SiO_2 HNPs as new functional fillers to improve the balance between high reinforcement and low hysteresis;

iii) the assessment of the self-organization effects of SiO_2 HNPs on the mechanical performance of the materials;

iv) the study of the interactions between polybutadiene (PB)-functionalized HNPs and of their self-assembly behavior both in the rubber matrix and in matrix-free conditions, in order to determine which parameters control the self-assembly processes.

In the first part, an effective procedure was established to produce PB-grafted SiO_2-HNPs based on a colloidal three-step grafting-to approach. Structure, morphology and surface chemistry were extensively investigated by a multi-technique analysis, confirming that the preparation is a simple and multi-gram scale synthesis, applicable to different kind of NPs and polymer matrices, in particular rubbery polymers, rarely considered until now.

Then, SiO_2 HNPs with different degrees of polymeric surface coverage were used to prepare rubber NCs. An exhaustive dynamo-mechanical characterization of the cured and uncured rubber NCs based on SiO_2 HNPs was performed. The effect of the self-assembly behavior of core-shell NPs was studied thanks to in-depth morphological characterization, to understand how the formation of anisotropic filler networking affects the reinforcement and hysteresis of rubber materials.

At last, to test the potential application of SiO_2 HNPs in the tyre perspective, technological formulation was optimized to adopt the HNPs model in a more scalable system. In detail, a commercial silane-terminated PB was selected to compatibilize commercial precipitated silica directly during the mixing process, by following an *in-situ*

approach. The effect of the macromolecular silane was compared to that of a standard, short-chain silane, studying its impact on the mechanical properties with a focus on the large-strain nonlinear mechanical behavior.

Finally, a more in-depth study of HNPs self-assembly was also conducted by a combination of theoretical modelling of HNPs interactions and small-angle X-ray scattering (SAXS) analysis, to gain additional understanding of the physical forces at play.

iii. Structure of the Thesis

The research described in this Thesis is subdivided with the following structure.

In *Chapter 1*, a general overview of the state-of-the-art of the use of inorganic NPs as fillers in PNCs is reported, with particular attention to silica and silica HNPs. A focus on the preparation and main properties of HNPs is presented with focusing on the self-organization capability and the impact on the material properties, in particular rubber NCs.

In *Chapter 2*, the synthesis of PB-grafted SiO_2 HNPs is described. The characterization of the materials is discussed to define the structure and morphology of the synthesized core-shell particles. Their self-assembly capability was studied by observing HNPs in both matrix-free conditions and introducing them in NC films prepared by solvent evaporation.

Chapter 3 illustrates the use of SiO_2 HNPs as fillers in rubber NCs and discusses their effects on the properties of uncured and cured NCs compared to bare silica, focusing on the mechanical properties and cross-linking density. These properties were correlated to filler

dispersion and distribution through morphological characterization and swelling tests.

In *Chapter 4*, the preparation of rubber NCs using a commercial macromolecular silane in a technical formulation, based on the HNPs model, is discussed. The effect of the macromolecular silane *versus* a typical short-chain silane is described, with a focus on the nonlinear mechanical properties.

Chapter 5 is dedicated to the discussion of a theoretical model for HNPs interactions, to determine the forces that predict the emerging HNPs superstructures. Data obtained from SAXS experiments on HNPs solution are included in this model.

Finally, *Chapter 6* sums up the main results and reports the conclusion of the research activity.

iv. Bibliography

1 L. Tadiello, M. D'Arienzo, B. Di Credico, T. Hanel, L. Matejka, M. Mauri, F. Morazzoni, R. Simonutti, M. Spirkova and R. Scotti, *Soft Matter*, 2015, **11**, 4022–4033.

2 M. Crippa, A. Bianchi, D. Cristofori, M. D'Arienzo, F. Merletti, F. Morazzoni, R. Scotti and R. Simonutti, *J. Mater. Chem. C*, 2013, **1**, 484–492.

3 S. Mostoni, M. D'Arienzo, B. Di Credico, L. Armelao, M. Rancan, S. Dirè, E. Callone, R. Donetti, A. Susanna and R. Scotti, *Ind. Eng. Chem. Res.*, 2021, **60**, 10180–10192.

4 P. Dwivedi, S. S. Narvi and R. P. Tewari, *J. Appl. Biomater. Funct. Mater.*, 2013, **11**, 129–142.

5 N. J. Fernandes, D. C. Company, H. Koerner, A. Force and E. Giannelis, *MRS Commun.*, 2013, **3**, 13–29.

6 L. Tripaldi, E. Callone, M. D'Arienzo, S. Dirè, L. Giannini, S. Mascotto, A. Meyer, R. Scotti, L. Tadiello and B. Di Credico, *Soft*

Matter, 2021, **17**, 9434–9446.

7 S. K. Kumar, N. Jouault, B. Benicewicz and T. Neely, *Macromolecules*, 2013, **46**, 3199–3214.

8 R. Scotti, L. Conzatti, M. D'Arienzo, B. Di Credico, L. Giannini, T. Hanel, P. Stagnaro, A. Susanna, L. Tadiello and F. Morazzoni, *Polymer (Guildf).*, 2014, **55**, 1497–1506.

9 B. Di Credico, E. Cobani, E. Callone, L. Conzatti, D. Cristofori, M. D'Arienzo, S. Dirè, L. Giannini, T. Hanel, R. Scotti, P. Stagnaro, L. Tadiello and F. Morazzoni, *Appl. Clay Sci.*, 2018, **152**, 51–64.

10 X. Zhao, C. Zhou and M. Liu, *J. Mater. Chem. B*, 2020, **8**, 838–851.

11 L. Bokobza and J. P. Chauvin, *Polymer (Guildf).*, 2005, **46**, 4144–4151.

12 M. Tian, L. Cheng, W. Liang and L. Zhang, *Macromol. Mater. Eng.*, 2005, **290**, 681–687.

13 J. Sharma, *ChemNanoMat*, 2017, **3**, 214–222.

14 S. Nie, J. Lacayo-Pineda and M. Wilhelm, *Soft Mater.*, 2019, **17**, 269–282.

15 J. L. Leblanc, *Prog. Polym. Sci.*, 2002, **27**, 627–687.

16 E. Cobani, I. Tagliaro, M. Geppi, L. Giannini, P. Leclère, F. Martini, T. C. Nguyen, R. Lazzaroni, R. Scotti, L. Tadiello and B. Di Credico, *Nanomaterials*, 2019, **9**, 486.

17 Mostoni, Milana, Credico, D'Arienzo and Scotti, *Catalysts*, 2019, **9**, 664.

Chapter 1.
Silica Hairy Nanoparticles. A promising material for functional nanocomposites

1.1. Overview

The addition of inorganic nanoparticles (NPs) to polymer matrices is one of the most promising strategies to produce materials with improved mechanical and functional properties. These materials, known as polymer nanocomposites (PNCs), find their application in a variety of different fields, from automotive[1] to dielectrics,[2] from catalysis[3] to medical devices.[4] The properties of such materials are strongly dependent not only on geometrical characteristics of the NPs, such as size and shape, and the effective dispersion of the inorganic component but also on the interfacial interactions between polymer and NPs and overall on the control of the morphology of NPs organization at the local scale within the NC.

Actually, the main issue concerning PNCs is the dispersion of the inorganic NPs, also known as filler particles, within the polymer matrix: since inorganic NPs are often hydrophilic, while polymer matrices are mostly nonpolar and hydrophobic, achieving the homogeneous distribution of filler particles can be a serious challenge. On the other hand, several properties of PNCs can be enhanced by controlling the spatial distribution of NPs within the polymer matrix, i.e. the creation of alternative structures like sheets, vesicles, percolating clusters, etc., with the goal of improving a range of other properties, *e.g.*, thermal conduction, selective permeation of gases.[5]

In this context, the properties of inorganic NPs, such as their size, shape and surface chemistry, need to be specifically tailored to achieve precise control of the NC's properties. Typically, inorganic NPs, such as silica NPs, are chemically modified to anchor small organic molecules, also known as coupling agents, onto their surface. This chemical modification favors the dispersion of filler NPs within the hydrophobic matrix by improving filler/matrix compatibility. As an alternative to these well-established approaches, the functionalization

of inorganic NPs with macromolecules, such as polymer chains, has recently attracted increasing attention.[6–8]

Hairy Nanoparticles (HNPs) are a class of hybrid NPs functionalized with polymer chains which can be designed for a variety of different applications, such as drug nanocarriers, smart materials and catalysts. In the context of polymer NCs, HNPs can strongly improve filler/matrix interactions. Furthermore, it has been established that HNPs, although consisting of spherical particles, can self-organize within polymer matrices to produce ordered anisotropic structures, thus offering accurate control of filler distribution.

This process arises because the immiscible particle core and grafted polymer layer attempt to phase separate but are constrained by chain connectivity — this is evidently analogous to 'microphase separation' in block copolymers and other amphiphiles.[9] Similar to these amphiphiles, these particles with a polymeric segmental cloud can self-assemble under a broad range of conditions into a variety of superstructures with beneficial effects on the mechanical and functional properties of hybrid materials.

However, while it has been exhaustively demonstrated that anisotropic NPs, like rod-like silica[10] and silicate nanofibers[11,12] in the polymeric materials are able to produce the oriented and anisotropic filler assemblies, like sheets, vesicles, percolating clusters, the issues that determine HNP spatial distribution and organization, and how they affect the macroscale properties of the hybrid, remain an open issue to investigate.

1.2. Rubber Nanocomposites

Introducing inorganic particles into polymer matrices is a common strategy to produce materials with improved functional properties and specific technological applications (Figure 1.1). Compared to traditional composites, where inorganic particles are in the micrometer

or millimeter size, polymer nanocomposites (PNCs) involve the use of nanoscale fillers. These fillers are characterized by at least one dimension in the nanometer scale: they can be 2D (nanosheets and nanoplatelets), 1D (nanofibers, nanorods) or have three dimensions in the nanoscale.[5] The combination of polymer and filler depends on the desired application of the final materials. Examples of 2D fillers are layered silicates and graphene, producing so-called layered PNCs. Examples of commonly used one-dimensional fillers are carbon nanotubes and halloysite nanotubes. Finally, spherical NPs often used as fillers are silica NPs (see Paragraph 1.3), carbon black (CB), metal oxide NPs, such as ZnO, TiO_2, and quantum dots.[13]

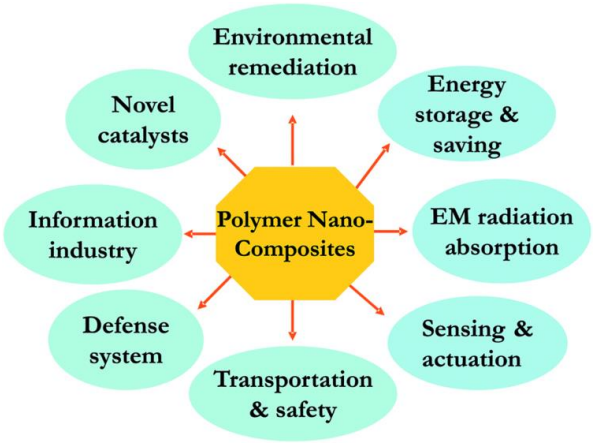

Figure 1.1 Different applications of PNCs.

Different types of polymer matrices can be used. The most common can be classified as follows.[14]

- Thermoplastics. These polymers soften upon heating. The curing process is reversible since they solidify and harden on cooling.

- Thermosets. They are composed of polymer chains that cross-link upon curing forming an irreversible chemical bond. These polymers do not soft or melt when heated.
- Elastomers or rubbers. These materials are characterized by a low glass transition temperature (T_g) and high elasticity. They require crosslinking (typically through the vulcanization process). This is the case of styrene-butadiene rubber (SBR), natural rubber (NR), isoprene rubber (IR) and polybutadiene (PB).

The main advantage of PNCs over conventional composites is the presence of an ultra-large interfacial area between the inorganic filler and the organic matrix. The prevalence of the interfacial regions in these materials is the result of the nanoscale size of filler particles, providing a very high surface to volume ratio. This phenomenon is commonly referred to as the "nano-effect" and produces enhanced mechanical and physical properties.[5,15]

Among PNCs, rubber NCs are widely used in tyres, technical parts, and consumer goods where elasticity is an important requirement. Reinforcing fillers are used in order to improve the properties of rubber compounds that derive many of their mechanical properties from the admixture of these reinforcing (active) fillers at quantities of 30% up to as much as 300% relative to the rubber part.

Filler compatibility with rubber polymer depends on the interactions producing low interfacial tension at the polymer–particle interface that can be achieved through previous structural and chemical modification of particles and rubber. Moreover, mechanochemical reactions take place during rubber compounding that can also make a positive contribution to rubber–filler low interfacial tension.

Carbon black and nanosilica are the most commonly used fillers in rubber NCs. However, recently novel filler systems have received attention such as polyhedral oligomeric silsesquioxane (POSS), carbon-nanotubes, graphene, layered double hydroxides, clays. Generally, as compared with microfiller-reinforced rubber, nanofiller-reinforced rubber exhibits high hardness, modulus, anti-aging and gas barrier properties. Therefore, the nanoconcept is highly relevant for rubber compounds since their applications require filler reinforcement.

1.2.1. Rubber NCs for green tyre technology

Materials for tyres are some of the most complex rubber NCs and they are still technologically evolving. Tyres have many different components with specific roles to play. They are composed of polymeric materials such as natural rubber and/or synthetic rubbers, chemicals which function as antioxidants, curing agents, processing aids and reinforcing fillers. These materials are selected based on their physico-chemical properties and their interactions with other constituent materials to provide a broad range of mechanical properties.

Individual compounds are designed and formulated to meet the specific set performance requirements of each tyre component. This is primarily accomplished through the selection of fillers, elastomer types, chemicals for vulcanization, materials for facile processing and tyre manufacturing, and materials for in-service performance.

In rubbers, fillers are used to achieve products with improved properties for end use applications. Taking into consideration the main contributions of reinforcing fillers to the mechanical properties of rubber composites, the first open challenge of the tyre industry is to identify possible design strategies and alternative fillers to reduce the environmental impact throughout the life cycle of the tyre by means

of both the use of environmentally friendly materials and the development of innovative products capable of reducing energy consumption and CO_2 emissions.

Design of materials for tyres has a great environmental impact. About 18% of the carbon emissions in the world are due to vehicles, and approximately 24% of this amount can be attributed to tyres.[16] The reason why tyres have such a significant impact on climate change is due to energy dissipation. The safety of tyres is related to the grip between the rubber and the road under dry and wet conditions.[17] However, grip is related to dissipation in high deformation and frequency regimes. Dissipation phenomena operate also in a regime of low deformation and frequency, generating a longitudinal force oriented in the opposite direction with respect to the rolling movement. As the tyre rolls, deformation of the rubber material takes place, thus generating a loss of mechanical energy as heat. This effect is defined as "rolling resistance".

Lowering rolling resistance is one of the main goals in the development of tyre technology due to its detrimental effects on the performance of the vehicle and its high environmental impact. As illustrated in the graph reported in Figure 1.2, rolling resistance is by far the main responsible for the CO_2 emitted from car tyres, accounting for 80% of the total emissions. However, a certain amount of rolling resistance is necessary to guarantee effective tyre grip and braking.[16]

Contributions to rolling resistance may be classified as follows.

- The tyre's cyclic deformation, causing loss in the internal mechanical energy of the material. This effect contributes up to 80-95% of the total rolling resistance. It is also known as "hysteresis" and it is related to the viscoelastic mechanical properties of the rubber NC (see Paragraph 1.2.2). Hysteresis can be minimized by

tailoring the filler-filler and filler-rubber interactions on the nanoscale.

- The "aerodynamic drag" due to the friction between the tyre and the surrounding air during rotation. Depending on speed, it can cause between 0 % and 15 % of total rolling resistance.
- The "frictional slip", due to the heat build-up when the tyre comes into contact with the road. This effect contributes only to 5 % of theoverall rolling resistance.

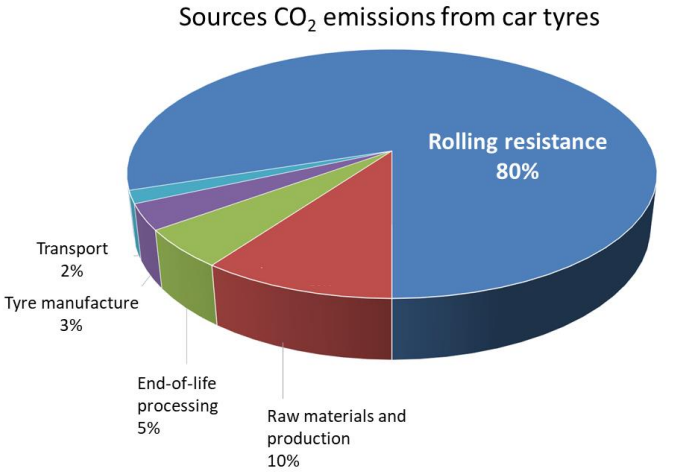

Figure 1.2 Origin of CO_2 emissions from tyres.

Furthermore, in addition to rolling resistance, also wet-grip and wear resistance are important parameters to be addressed. The wet-grip, meaning the ability of the tyre to adhere to the road in wet conditions, is crucial to the safety of tyres, while the wear resistance is associated with longer tyre lifetime and reduced pollution from the leaching of solid particles. Increasing wear resistance, which is associated with

higher rubber reinforcement, also leads to more sustainable tyre technology. Addressing these three challenges simultaneously is one of the biggest obstacles in the improvement of tyre technology. Visually, the balance between rolling resistance, wet-grip and wear resistance has been typically represented with the so-called “magic triangle”, illustrated in Figure 1.3.

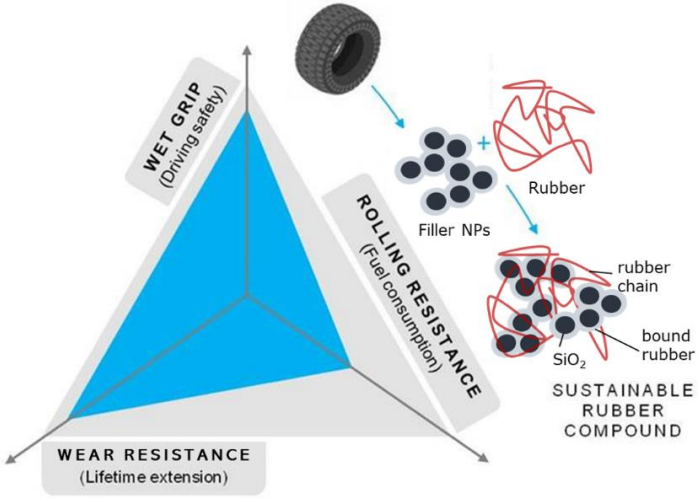

Figure 1.3 The "magic triangle" of tyres. The gray triangle represents the optimal balance between low rolling resistance, high wet grip and high wear resistance. Adapted from Araujo-Morera *et al.*[18]

1.2.2. Mechanical properties of rubber NCs

The properties of a system resulting from the combination of two components, such as polymer and filler in PNCs, can be defined mathematically by Equation 1.1:

$$P(NC) = \varphi P(f) + (1 - \varphi)P(m) \qquad (1.1)$$

where P(NC) are the properties of the composite system, P(f) are the properties of the filler, P(m) are the properties of the matrix and φ is the volume fraction of the filler. In general, this equation indicates that the properties of a composite system are the combination of the properties of each component weighted by each component's volume fraction. However, this expression does not consider the presence of nanoscale synergistic effects.

In this context, rubber NCs exhibit a combination of the mechanical behavior of filler and matrix, *i.e.* they act both as elastic solids and viscous fluids. For this reason, rubber NCs are defined as viscoelastic materials. During a deformation, a viscoelastic material will store part of the received energy, while the remaining is dissipated as heat due to internal friction of the microstructure of the material.

Typically, the characterization of the dynamic mechanical properties of viscoelastic materials is carried out in oscillatory shear tests. An oscillatory shear strain γ(t) with a fixed frequency ω is applied to the materials and the resulting torque is measured, obtaining information about the shear stress σ(t). The equation of the strain and stress curves is reported in Equations 1.2 and 1.3:

$$\gamma(t) = \gamma_0 + \sin(\omega t) \tag{1.2}$$

$$\sigma(t) = \sigma_0 \sin(\omega t + \delta) \tag{1.3}$$

where δ is a constant value. By developing Equation 1.3, we obtain the expression in Equation 1.4:

$$\sigma(t) = \sigma_0[\sin(\omega t)\cos(\delta) + cos(\omega t)\sin(\delta)] \tag{1.4}$$

Following from Equation 1.4, we can introduce two additional parameters, known as the storage modulus G' and the loss modulus G'', expressed in Equations 1.5 and 1.6:

$$G' = \frac{\sigma_0}{\gamma_0}\cos(\delta) \quad (1.5)$$

$$G'' = \frac{\sigma_0}{\gamma_0}\sin(\delta) \quad (1.6)$$

Then, the complex modulus is defined in Equation 1.7:

$$G^* = G' + iG'' \quad (1.7)$$

The complex modulus G* expresses the mechanical response of the viscoelastic material and it is composed of the in-phase elastic component G' and the out-of-phase viscous component G''. The ratio of G'' and G', known as tan δ, expresses the hysteresis of the material, *i.e.* the amount of energy lost per deformation cycle.

1.2.3. Filler dispersion and distribution

Filler NPs distribution and dispersion within the polymer matrix should be accurately controlled to obtained high-performance NCs. Excessive agglomeration, leading to phase-separation, strongly reduces the effect of the filler in the NCs by limiting the interfacial area between the two components.

In this context, it is crucial to keep in mind the distinction between filler dispersion and filler distribution, illustrated in Figure 1.4. While good dispersion indicates that individual filler NPs are separated from each other instead of forming aggregates or clusters, distribution refers to the homogeneous presence of filler in every region of the polymer matrix.[14]

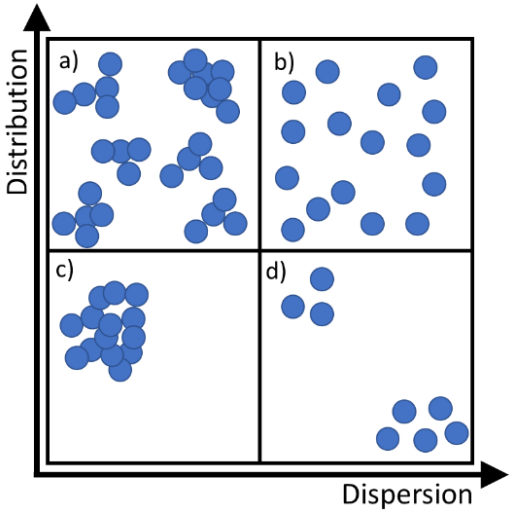

Figure 1.4 Schematic illustration of filler dispersion and distribution in PNCs: a) Poor dispersion, good distribution; b) good dispersion, good distribution; c) poor dispersion, poor distribution and d) good dispersion, poor distribution.

The balance between dispersion and distribution needs to be accurately controlled to tailor the properties of the rubber NC. While good distribution is always desirable to produce homogeneous properties in the final macroscopic material, the presence of filler-filler and filler-polymer interactions and their balance determines improved mechanical properties of the NCs.[1,10–12,19]

The reinforcement of rubber NCs depends on the hydrodynamic effect due to the addition of filler NPs; this effect is proportional to the filler volume fraction. The reinforcement mechanism, however, is not limited to this parameter but it depends on two additional factors. The first one is the filler network structure, participating to the total elastic modulus together with the crosslinked polymer matrix. Secondly,

another contribution is due to the interfacial interaction between the polymer and the filler. This filler-polymer interaction reduces the mobility of the matrix polymer chains by increasing the amount of rigid rubber in the material.[11] This is due to the increase of enclosed rubber between the individual NPs, resulting in higher stiffness and better reinforcement with reduced hysteretic effects, as will be discussed in detail in Paragraph 1.5.2.

1.2.4. Filler network and the Payne effect

The properties of PNCs are controlled by the formation of the so-called percolative network or filler network. Briefly, the properties of a NC drastically change upon a certain filler concentration threshold, also known as percolation threshold. Upon reaching this concentration, filler NPs begin interacting with each other producing a dramatic change in the properties of the materials. In a given range of particle loading, the filler gives rise to interconnected structures, through both the direct particles interaction, and their bridging by polymer chains.

The percolation threshold can impact several different functional properties of PNCs, such as thermal conductivity, electrical conductivity, dielectric constant as well as the mechanical properties. The properties of PNCs near percolation can be expressed by Equation 1.8:[20]

$$P(NC) \propto |\varphi - \varphi_c|^{\pm e} \qquad (1.8)$$

where φ_c is the critical filler concentration and *e* is a critical exponent specific of each property of the NC. The variation of the NC properties with filler concentration resulting from Equation 1.8 is illustrated in Figure 1.5.

In the case of the mechanical properties of filled elastomers, percolation results in the Payne effect, a shear-softening behavior typical of rubber NCs resulting from the breakdown of the filler-filler interactions in the materials. This effect takes the name from Payne, who first reported it in 1962.[21] The Payne effect is observed through oscillatory dynamic mechanical analysis of rubber NCs by monitoring the G' curve vs. strain.

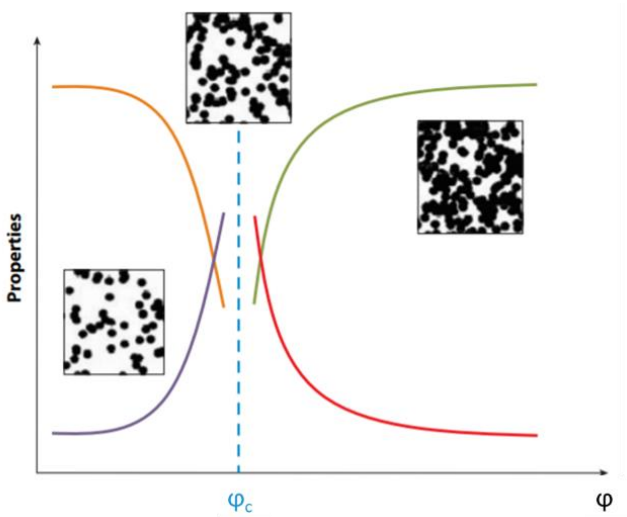

Figure 1.5 Variation of NC properties with filler volume fraction ϕ upon reaching the percolation threshold. Adapted from Nan *et al.*[20]

The typical G' behavior for cured filled rubber NCs is illustrated in Figure 1.6. The storage modulus results from different contributions:

- the formation of the rubber polymer network from the vulcanization process;
- the hydrodynamic effect due to the addition of inorganic NPs;

- the filler-rubber interaction, resulting from NPs compatibilization and assembly;
- the filler-filler interaction, due to interparticle forces such as hydrogen bonds, Van der Waals and electrostatic attraction.

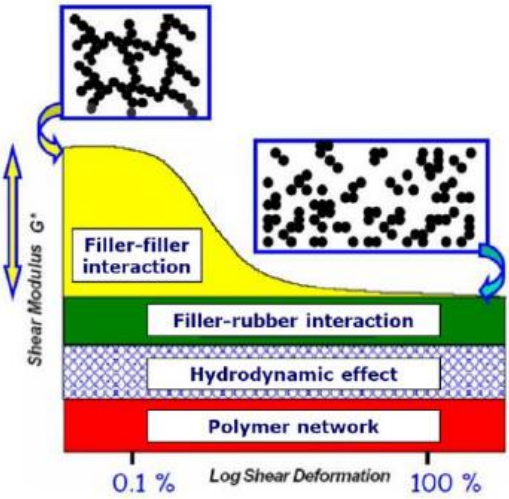

Figure 1.6 Typical G' vs. strain curve obtained for polymer NCs, highlighting the different contributions.

In this context, crucial parameters for the characterization of the mechanical properties of materials are the reinforcement, expressed as the value of G' at low strain, and the ΔG', expressed by the difference between G' at low strain and high strain. The ΔG' results from a phenomenon known as the Payne effect. The Payne effect is observed when, upon deformation, filler-filler interactions gradually break down, resulting in a loss of storage modulus.

Thus, in order to provide clay-based rubber materials suitable for tyre applications, the reinforcement effect should go hand in hand with the

formation of an extended percolative network, a good filler dispersion and distribution, and an effective interaction of NPs with rubber.

1.3. Silica nanoparticles

Silicon dioxide or silica is the most abundant component in the Earth's crust. The term silica refers to all solid materials with a general chemical formula SiO_2 or $SiO_2 \cdot nH_2O$. Silica is typically composed of tetrahedral units with a central silicon atom surrounded by four oxygen atoms. Because the oxygen ions are much larger than the Si^{4+} ion, the silicon ion occupies a tetrahedral hole within the four oxygens in the material's structure. The length of the Si-O bond, also known as siloxane bond, is 0.162 nm, larger than the sum of the Si and O radii. This indicates a partially polar bond, which is responsible for its higher stability compared to other Si-X bonds.[22,23]

Depending on the spatial organization of these tetrahedral units, both synthetic and natural silica can exist in either crystalline or amorphous states (Figure 1.7). Crystalline silica, in which the tetrahedral SiO_4 building blocks are disposed in an ordered structure, exists in nature in five possible polymorphs: quartz, tridymite, cristobalite and, less frequently, coesite and stishovite.

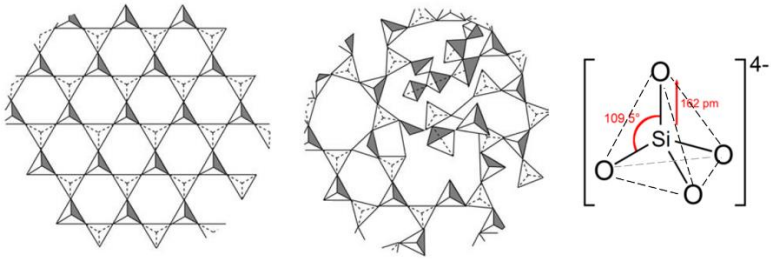

Figure 1.7 Schematic structure of crystalline and amorphous silica. Adapted from Bergna *et al.*[22]

Quartz is the most common form of silica and it is stable below 870 °C. It is also the densest form of crystalline silica. Tridymite is stable below 1470 °C and cristobalite is stable below 1710 °C, although both forms are metastable at room temperature and atmospheric pressure. Each of these three polymorphs exists in two variants, α and β, which differ only slightly in the orientation of the tetrahedral units. In the case of quartz, the α form is stable at room temperature but undergoes a transition to the β phase at 573 °C, in a phenomenon known as *inversion*.[22]

Within the biosphere, silica is soluble in water in its simplest form as silicic acid or $Si(OH)_4$. Silicic acid undergoes continuous condensation and hydrolysis reactions which determine the formation of natural amorphous silica, also known as opal. The conversion of silicic acid to silica and vice-versa is described in Equation 1.1.[24]

$$(SiO_2)_x + 2H_2O \leftrightarrow (SiO_2)_{x-1} + Si(OH)_4 \quad (1.1)$$

Amorphous silica can exist both in mineral form and in living organisms, like the stems and leaves of plants, sponges and microorganisms such as diatoms, which are the most common photosynthetic algae composing phytoplankton. This latter form of silica is also known as *biogenic silica* and it plays a crucial role in the formation of biological structures.

1.3.1. Industrial production of silica

Due to its low cost, large availability and great variety of industrial applications, silica is one of the most widespread synthetic materials. However, natural silica from mineral sources is often contaminated by other metal ions. Furthermore, natural silica is found mostly in its crystalline quartz form, a material which has raised some concerns regarding its detrimental effects on human health.[23] For this reason, silica is currently mostly produced synthetically by industrial or

chemical approaches. The most important aspect of the synthesis of nano-silica is the control of morphology and aggregation state, which are strongly dependent on the synthetic pathway.

In general, the most common approaches for the synthesis of silica can be divided based on the physical state of the precursors:[23]

- Gas-phase routes, such as pyrogenic silica, use gaseous precursors and typically involve high temperatures and industrial processes;
- Liquid-phase routes, such as the Stöber method, involve the synthesis of silica by controlled hydrolysis and condensation reactions, and are usually carried out at room temperature.

Several gas-phase methods have been developed for the synthesis of silica, although only two have retained commercial significance. The first method is arc silica, which involves the reduction of quartz to SiO with coke at 2000 °C. The obtained SiO is then oxidized by air or steam to form spherical, highly dispersed silica nanoparticles. However, this process is extremely energy intensive, involving very high temperatures. For this reason, this approach has been declining in popularity since the 1990s and has now very little commercial relevance.[22]

The most widely employed gas-phase approach for the synthesis of silica is pyrogenic or fumed silica. Historically, this is the first synthetic method for the commercial production of silica. It was first developed in Germany in the 1940s, when the chemist Harry Kloepfer was researching an alternative white filler material in the tyre industry for substituting carbon black. In this context, the first fumed silica, known as AEROSIL and still commercialized today, was manufactured by Evonik-Degussa.[23,24]

Fumed silica is produced by using silicon tetrachloride, $SiCl_4$, as a volatile liquid precursor. It is worth noting that $SiCl_4$ is a toxic byproduct of the polysilicon industry, and the possibility of repurposing this waste material still constitutes one of the main advantages of the fumed silica approach. The production process of fumed silica is schematized in Figure 1.8. First, $SiCl_4$ is vaporized in a flame composed of hydrogen and oxygen between 1100 and 1800 °C. Then, the silicon tetrachloride precursor undergoes condensation polymerization generating silica and hydrochloric acid as a byproduct.

The synthesis of fumed silica is described in Equation 1.2.

$$2\,H_{2\,(g)} + O_{2\,(g)} + SiCl_{4\,(g)} \xrightarrow{>1000\,^{\circ}C} SiO_{2\,(s)} + 4\,HCl_{\,(g)} \qquad (1.2)$$

Silica particles resulting from this process are formed as primary particles in the range of 7 to 40 nm, which are then aggregated into larger, "string-of-pearl"-like structures with fractal morphology, possessing specific surface areas in the range of 50-350 m^2/g.[23] Fumed silica is commercially employed in coatings, as a rheological additive, as a reinforcing filler for concrete and for the production of silicone for medical applications. Due to its high cost compared to other synthesis methods, however, its applications are still limited.

Besides fumed silica, most synthesis methods for silica are liquid-phase approaches. The most employed silica for industrial applications is precipitated silica, which is produced from sodium silicate ($Na_2O{\cdot}2.6\ SiO_2$) by reaction with sulfuric acid, as reported in Equation 1.3.[23]

$$Na_2O \cdot 2.6\,SiO_2 + H_2SO_4 \rightarrow 2.6\,SiO_2 + Na_2SO_4 + H_2O \qquad (1.3)$$

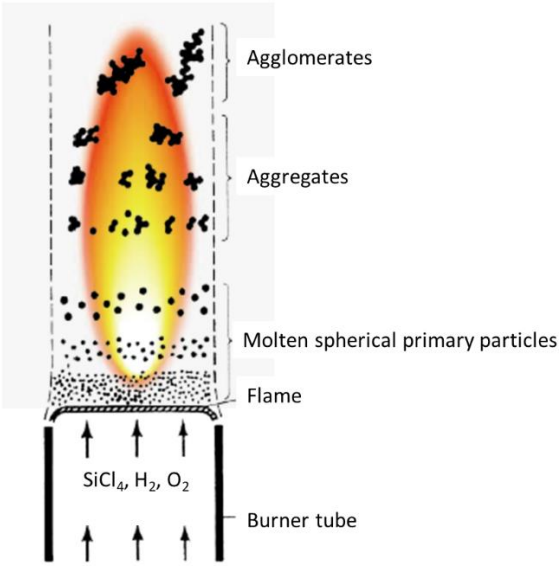

Figure 1.8 Production process of fumed SiO_2. Adapted from Bergna *et al*.[22]

This method involves the neutralization of the basic sodium silicate with sulfuric acid, thus increasing the concentration of silicic acid in the solution above the solubility threshold. Conditions such as pH, stirring rate, temperature and reactant concentrations influence the resulting silica morphology.

Typically, precipitated silica possesses a specific surface area in the range of 30 to 800 m^2/g and has primary particle sizes between 2 nm and 20 nm. Precipitated silica also has high water content (3-7 wt%) in the form of surface silanols, which are available for the chemical modification of the particles' surface.[23]

Precipitated silica is widely applied in the tyre industry, where it is used as a high reinforcement, low-hysteresis filler. In this context,

Zeosil grades by Solvay and Ultrasil grades by Evonik are some of the most utilized silicas for tyres.

1.3.2. Colloidal silica and the Stöber method

Although the above synthetic approaches can be employed to produce silica in its pure form, their application is affected by the harsh synthetic conditions and particles aggregation phenomena. For this, colloidal silica particles have received a widespread interest because they possess versatile surface chemistry and are non-toxic, expanding its use in drug delivery, biosensors, bioimaging, *etc.*

Colloidal systems are defined by the presence of particles with a size small enough to resist precipitation but large enough to exhibit different properties compared to chemical solutions.[22,25] More specifically, the colloidal range, as defined by the International Union of Pure and Applied Chemistry (IUPAC), is comprised between 1 nm and 1 μm. According to this definition, a colloidal dispersion is a system where particles of any physical state (solid, liquid or gaseous) in the colloidal range are dispersed in a distinct continuous phase.

The Stöber method is one of the most popular and versatile approaches for the synthesis of colloidal silica, offering great control of NPs morphology. It is well suited to produce well-defined, monodispersed, uniform silica spheres in a facile manner by simply adjusting reaction parameters such as reactant concentration, temperature, etc. After it was first developed in 1968 by Stober, Fink and Bohn,[26] the method was mostly neglected for the following thirty years. Only recently, the potential of this synthesis was finally recognized, and it now widely applied in the field of nanomaterials and soft matter.[25,27]

The Stöber synthesis is based on the hydrolysis and condensation reactions of a silicon alkoxide, typically tetraethylorthosilicate (TEOS), in a water and ethanol mixture, in the presence of ammonia

as a catalyst. The mechanism of the synthesis is illustrated in Figure 1.9.

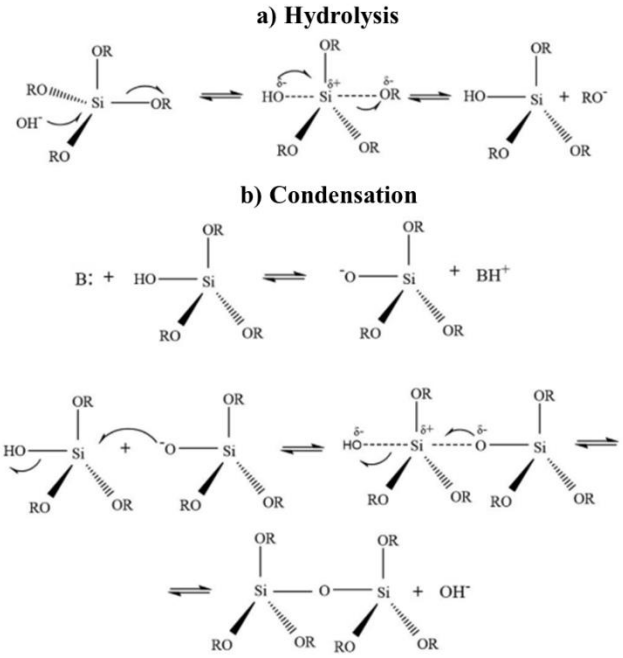

Figure 1.9 Reaction mechanism for Stober silica. Adapted from Ghimire *et al.*[25]

The first step of the reaction mechanism is the hydrolysis of TEOS, which takes place when the ethoxy group is converted into a silanol group via the nucleophilic attack of water. For the hydrolysis to be effective, the reaction needs to be catalyzed by an acid or, as in the case of the Stöber synthesis, by a base like ammonia. The hydrolysis is concluded once all the ethoxy groups have been converted to silanols. The second step of the reaction mechanism is condensation,

which takes place when the silanols (Si-OH) are converted to siloxane bonds (Si-O-Si).

Two main models have been proposed for the formation of Stöber silica particles. The first model, proposed by Matsoukas and Gulari,[28] is known as the monomer addition model. In this model, the limiting step of the particle formation is the hydrolysis of the precursor. It is assumed that once the presence of the monomer, i.e. the hydrolyzed alkoxysilane, reaches a certain critical concentration, fast nucleation takes place until the concentration of monomer decreases below the threshold. Then, nucleation is followed by a growth step, where the remaining monomers react with the silica nuclei.

Alternatively, Bogush and Zukoski[29] proposed an aggregation-based model, which involves the continuous nucleation of silica particles throughout the synthesis. In this model, small nuclei aggregate to form larger particles. The different aggregation rates between particles of different sizes result in a self-sharpening mechanism, so that the final particles are uniform in size.

Likely, the real mechanism for the formation of silica particles is a combination of both the monomer addition and controlled aggregation-based model.[30]

The size and morphology of silica obtained by the Stöber method is influenced by a variety of parameters:[31,32]

- concentration of silicon alkoxide precursor;
- NH_3 concentration;
- reaction temperature;
- choice of the solvent (alcohol);
- water concentration.

In their original paper,[26] Stöber, Fink and Bohn synthesized particles in the range between 0.05-2 μm and studied the effect of different silicon alkoxides (tetra -methyl, -ethyl, n-propyl and n-butyl orthosilicates), different alcohols (methanol, ethanol, n-propanol and n-butanol), ammonia and water concentrations on particle sizes.[26] They found that reaction rates were the fastest and particle sizes were the smallest for methanol, while both parameters increased with increasing solvent molecular weight. Similarly, smaller alkoxysilanes produced fastest reactions and smaller sizes compared to larger ones. However, solvents and precursors with higher molecular weights also led to higher particle polydispersity.

The presence of ammonia plays a crucial role in the control of NPs morphology. Stöber *et al.* found that in absence of ammonia, the silica particles showed inhomogeneous size and irregular shapes. As the concentration of ammonia was increased up to 8 M, the size of particles was also shown to increase accordingly, possibly due to an increase in the rate of hydrolysis and condensation.[26] Recently, the same trend was confirmed by Yan *et al.*,[33] who also showed an increase of polydispersity with decreasing ammonia concentration.

Stöber *et al.* also studied the effect of water concentration, showing that, while keeping the other parameters constant, maximum particle size was reached at a concentration of 6 M.[31] This is due to a balance between hydrolysis rate, which increases with water concentration, and dilution of the reactive monomers. The presence of water also influences the particles morphology by favoring the formation of hydrogen bonds between smaller particles, leading to the formation of larger aggregates.[34]

Effects of temperature on particle size was originally investigated by Tan *et al.* in 1987,[35] showing that increasing temperature reduced the size of particles. This was attributed to the increase in nucleation rate

according to the monomer addition model. A similar temperature dependence on SiO_2 NPs size was recently reported by our research group.[7]

1.3.3. Surface chemistry of silica

The surface of silica is characterized by the presence of a variety of chemical groups, depending on the synthetic pathway, humidity, thermal and chemical treatments. In general, the most significant chemical group on the surface of silica are silanols, a term which refers to hydroxyl groups covalently bound to Si atoms. In general, different types of silanol groups can be identified on the surface of silica: single silanol groups, geminal silanol groups or silanediols, where two silanols are bound to the same Si atom, and surface siloxanes.[22,24,36] Solid-state ^{29}Si magic-angle spinning nuclear magnetic resonance (MAS NMR) spectroscopy can be used to determine and quantify each type of surface silanol group by distinguishing between the number of siloxane bonds surrounding a central Si atom (Figure 1.10).

In detail, chemical groups are classified as Q^{0-4} depending on the number of siloxane bonds, so that, for example, Q^4 refers to siloxanes, Q^3 to single silanol groups and Q^2 to geminal silanols. Similarly, surface Si atoms can also be classified as T^{1-3} based on the presence of organic chains linked to the Si atom. This classification is particularly useful in the study of surface functionalization of silica.

In the case of silica synthesized by the Stöber method, the surface of silica is also characterized by the presence of unhydrolyzed alkoxy-groups, typically ethoxy- groups when TEOS is used as a precursor and ethanol as a solvent. The presence of ethoxy groups in the surface of Stöber silica has been observed in thermogravimetric analysis and confirmed by solid-state ^{13}C-NMR. Van Blaaderen *et al.*[37] found that the degree of condensation of siloxane bonds in silica varies between 55–85%, which leads to the presence of residual ethoxy groups instead

siloxane bonds. Suratwala *et al.*[38] have proposed that the amount of surface ethoxy groups can be controlled by modifying the EtOH:H_2O ratio in the reaction mixture. According to Kunc *et al.*,[39] the presence of such groups makes the estimation of surface functionalization in Stöber silica by thermogravimetric methods a challenging task.

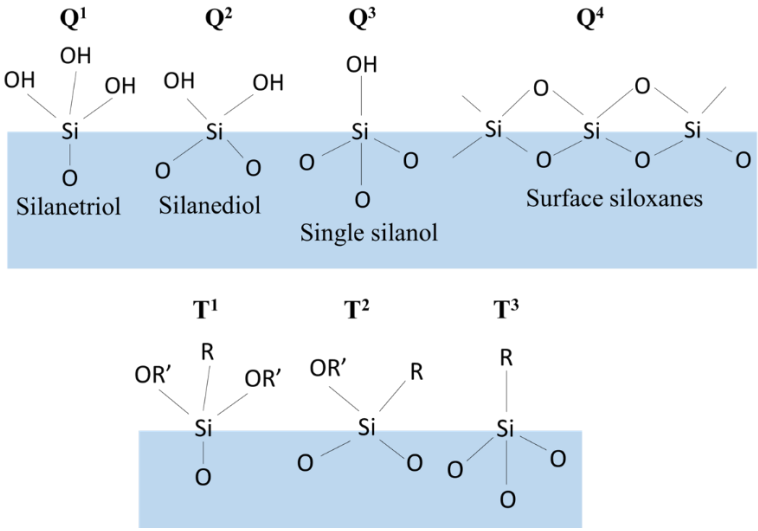

Figure 1.10 Classification of surface silanol groups and organosilane groups on the surface of silica.

1.3.4. Functionalization of SiO_2 NPs

Silica NPs are often chemically modified to improve their properties and control their dispersion and aggregation, in particular when are embedded in an organic matrix to produce NC material. The easiest and most used method for functionalization of the silica NP surface is the use of silanes as anchor chemistry. Many commercially available silanes exist and they cover a broad field of functional groups which can be used for further reactions. SiO_2 NPs are often functionalized

with organosilane molecules, also known as *coupling agents*, with a general chemical structure $R\text{-}(CH_2)_n\text{-}Si\text{-}X_3$. X is a hydrolizable chemical group, such as an alkoxy, halogen or amine group, while the R group is a non-hydrolizable organic chain. Depending on the required application, the R chain can introduce different functionalities which can further react with other molecules or with the polymer matrix itself.[40]

Silane chemistry allows the functionalization of SiO_2 NPs by following two possible alternative approaches: post-synthetic grafting, where the silane-silica covalent bond is formed after the NPs synthesis, and the co-condensation method, where the trialkoxysilane is used in combination with the tetraalkoxysilane precursors (e.g. TEOS) for the synthesis of silica (Figure 1.11).[41]

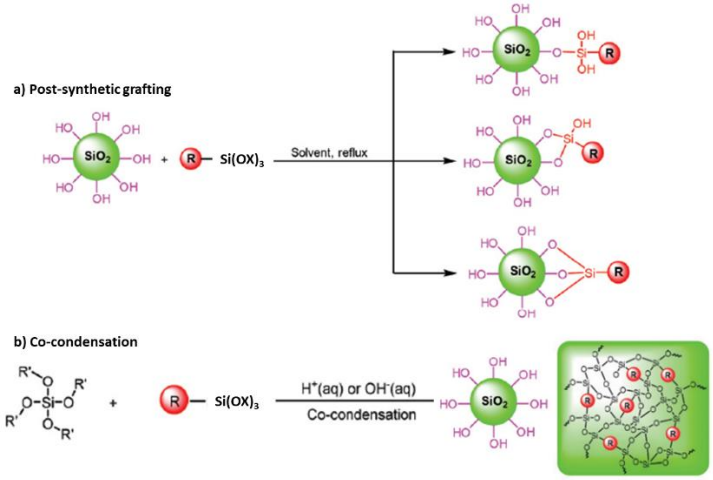

Figure 1.11 Schematic representation of a) post-sinthetic grafting and b) co-condensation of coupling agents for SiO_2 functionalization. Adapted from Li *et al.*[41]

Compared to post-synthetic grafting, co-condensation can offer improved surface distribution of silane and prevents pore blocking. For this reason, it has been employed for the high-density functionalization of mesoporous silica NPs for environmental and catalysis applications.[42–44]

Among the different types of organosilanes, aminosilanes, such as 3-aminopropyl triethoxysilane (APTES), N-2-aminoethyl 3-aminopropyltrimethoxysilane (EDA), and 3-trimethoxysilylpropyl diethylenetriamine (DETA), are widely used to modify the surface of silica for a variety of applications (Figure 1.12).[45] Often, such molecules are used in the field of catalysis, as ligands for the anchoring of metal ions. [44] Amino-silanes are also often applied in the absorption of environmental pollutants,[46,47] in the field of nanomedicine to design drug carriers[48,49] and as anchors to bind additional functionalities.[50,51]

Another widely used class of silane compounds are sulfur containing coupling agents, which are often included in silica-filled rubber systems. These molecules are also known as bifunctional silanes and have been commercially introduced in the tyre industry by Michelin in the 1990s. In addition to the hydrophobization of the silica surface, which leads to improved filler/rubber compatibilization, bifunctional coupling agents are characterized by the ability to form chemical bonds both with the silica surface and the rubber chains, by participating in the crosslinking process. For this reason, their introduction has revolutionized rubber technology by strongly improving the performance and mileage of tyres.[52]

The most important sulfur containing coupling agents are bis(3-triethoxysilylpropyl)tetrasulfide (TESPT) and bis(3-triethoxysililpropyl)disulfide (TESPD) (Figure 1.12). The disulfide bond of TESPD and the tetrasulfide bond of TESPT is decomposed by heat, reacting with elastomer chains and releasing sulfur. However, it

can lead to premature vulcanization, with undesirable consequences on rubber processing.[53]

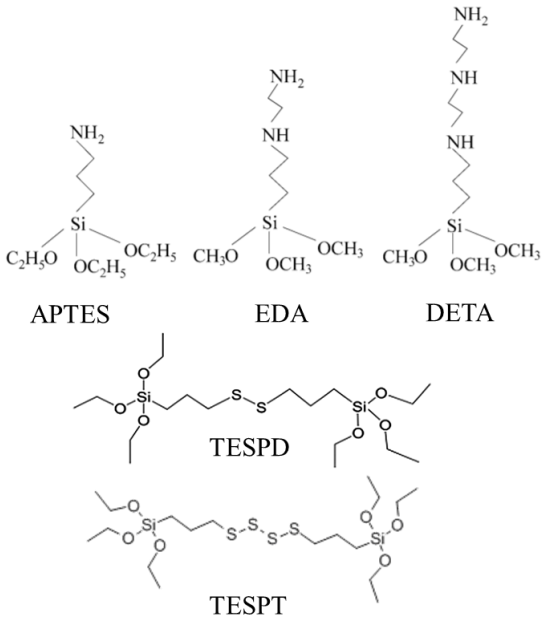

Figure 1.12 Chemical structure of the most common silane sulfur coupling agents.

In addition to TESPT and TESPD, other bifunctional, sulfur-containing coupling agents used in silica-filled rubber are mercaptopropyl triethoxysilane (MPTES), which induces strong filler-rubber interaction but is unstable due to a highly reactive thiol group, and S-3-triethoxysilylpropul octanethioate, also known as NXT, trademarked by Momentive Performance Materials *Inc.* NXT combines high filler/rubber compatibilization with good control of the vulcanization process.[54]

1.4. Hairy Nanoparticles

In recent years, the functionalization of NPs with polymer chains has attracted increasing attention because provides higher affinity between the inorganic particle and the organic component compared with NPs compatibilized with smaller molecules, drastically improving the interfacial interactions between the NC phases. In addition, HNPs are able to self-assemble into a variety of anisotropic structures, when they are dispersed in the corresponding homopolymer matrix, and thus improve the functional properties of NCs in a similar manner of anisotropic NPs.

The earliest examples of functionalization of inorganic particles with organic macromolecules date back to the 1950s, when polymers were used as stabilizing agents for colloidal dispersions.[55] Originally, polymers were used as steric stabilizers by exploiting physisorption. The idea of grafting polymers onto particles by forming chemical bonds was only developed in the 1980s.[56]

In the context of this thesis, the definition of Fernandes *et al.*,[57] and thus the Hairy Nanoparticles (HNPs) term was considered to refer to particles with the following properties:

i) the NP core has a size between 1-200 nm;

ii) the NP core is inorganic, or otherwise a rigid crosslinked polymer (e.g. polystyrene, PS), and has a well-defined interface with the corona;

iii) the corona is composed of non-crosslinked organic macromolecules, anchored to the surface of the core by a covalent or ionic bond.

HNPs can be classified based on several different parameters, such as:

- the chemical nature of the core (silica, gold, titanium dioxide, Fe_2O_3, quantum dots);
- the chemical nature of the polymer corona: biomolecules, polymers with high glass transition temperature (T_g) such as polystyrene, polymers with low T_g (elastomers), hydrophilic polymers such as polyethylene oxide (PEO), polypropylene oxide (PPO), polyvinyl alcohol (PVA), responsive polymers, block co-polymers;
- the type of polymer grafting: homopolymer grafting, bimodal grafting, "patchy" NPs, Janus NPs;
- the synthetic approach for grafting the polymer chains: grafting-from, grafting-to, one-pot or templated synthesis (Figure 1.13).

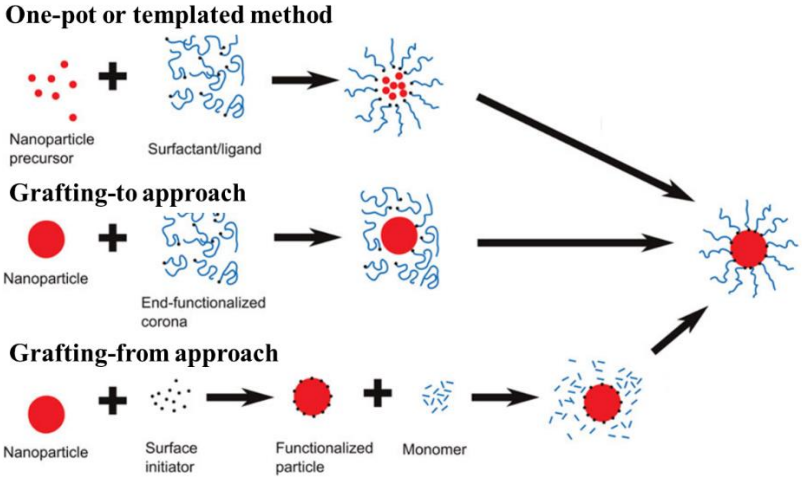

Figure 1.13 Grafting approaches for the synthesis of HNPs. Adapted from Fernandes *et al.*[57]

In this context, we will focus on the synthetic approach as a classification parameter for HNPs.[57] The grafting-from approach involves the growth of the polymer chains from a solution of the monomer, starting from chemical initiators, anchored onto the surface of the particles. The grafting-to approach, on the other hand, involves the anchoring of a pre-formed, end-functionalized polymer onto the surface of silica. It is important to note that this process might also require the functionalization of the NPs surface with a suitable anchoring molecule. Finally, the one-pot approach involves the anchoring of polymers with the simultaneous synthesis of the NPs core.[8,58,59]

1.4.1. Synthesis of HNPs by "grafting-from" approach

Starting from the early 2000s, the "grafting from" approach has acquired increasing popularity as a method for the synthesis of HNPs, particularly because it allows to synthesize polymer brushes with high grafting densities and offers optimal control of molecular weight and polydispersity of the polymer chains.[57,60,61] In "grafting from" approach, the polymer is synthesized by a class of chemical methods known as controlled radical polymerization (CRP).

CRP differs from the conventional free-radical polymerization (FRP) due to the presence of reversible activation/deactivation processes mediated by a specific activator species. In FRP, irreversible termination processes result in a statistical distribution of polymer length. Conversely, in CRP the *dispersity* Đ, namely the width of the molecular weight distribution of the polymer, is very low (≈ 1).[61] Among CRP methods, the two most popular approaches for the grafting of NPs are Atom Transfer Radical Polymerization (ATRP) and Reversible Addition-Fragmentation Chain Transfer (RAFT) polymerization.[61]

The ATRP mechanism (a in Figure 1.14) involves an *initiator*, typically an alkyl halide R-X, which produces activated R· radicals and from which the polymer chains grow. The *activator* is a transition metal complex, usually a Cu complex of an N-donor ligand, with formula LCu^{I}-X, that can exist in two different oxidation states. The activator reacts with the halogen atom in the initiator producing R· radicals and a *deactivator* LCu^{II}-X_2.

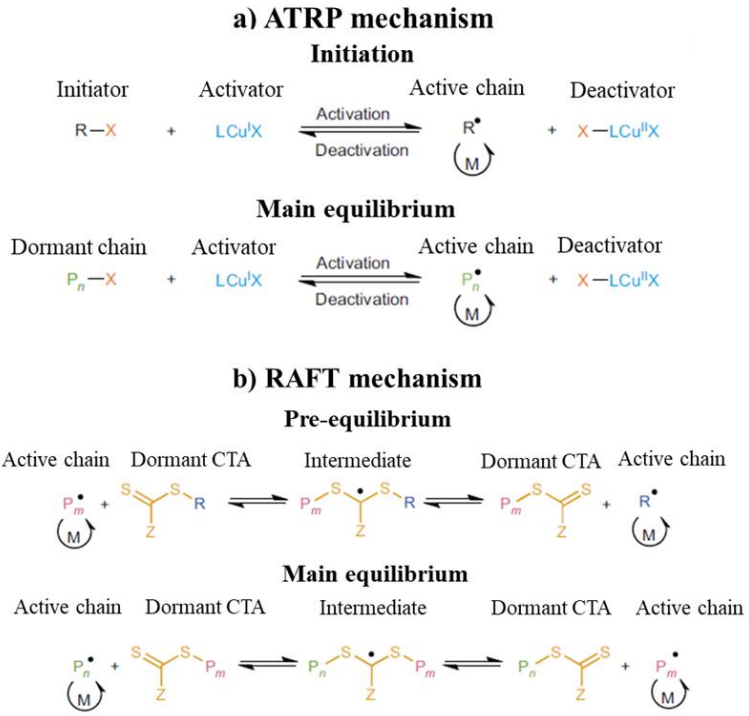

Figure 1.14 Mechanism of a) ATRP polymerization and b) RAFT polymerization used for the grafting-from synthesis of HNPs. Adapted from Truong *et al.*[61]

R· radicals react with monomer molecules, typically alkenes or substituted alkenes, until the activating radical is capped by the deactivator, forming P_n-X and LCu^I-X. This reversible redox reaction, in which "living" polymer radicals are intermittently activated and deactivated, constitutes the main ATRP equilibrium. A balance between activation and deactivation rates ensures that during each activation cycle each chain reacts with only one monomer molecule before being deactivated, while several activation cycles take place during the reaction. Therefore, uniform growth of polymer chains is achieved.

In the RAFT mechanism (b in Figure 1.14), radicals are generated in the same way as FRP, by fragmentation of a radical initiator like azobisisobutyronitrile (AIBN) which reacts with monomer molecules. The reversible activation/deactivation balance is guaranteed by the presence of a Chain Transfer Agent (CTA), typically a thiocarbonylthio- or thiocarbonylsulfanyl- molecule. One example is the dithioester R'S(S)CZ, where Z is a substituent modulating the CTA reactivity. The RAFT mechanism can be divided in two steps:

- Pre-equilibrium: the CTA molecule R'S(S)CZ reacts with the activated radicals P_n·, producing the intermediate R'S(P_nS)C·Z, which then fragments into P_nS(S)CZ and R'· radicals;
- Equilibrium: once R'S(S)CZ is consumed, the reaction proceeds by cycles of chain transfer between activated radicals: P_nS(S)CZ reacts with P_m·, giving P_mS(S)CZ and P_n·, where *n* and *m* are identical in the ideal case of the lowest dispersity (Đ = 1).

Similarly to ATRP, RAFT offers control of the polymerization process by favoring chain-transfer processes over propagation and termination. Since it does not involve the use of transition metals,

polymers produced by RAFT often require easier cleaning steps and are therefore frequently preferred for the synthesis of HNPs.[61]

Overall, "grafting-from" synthesis of HNPs is preferred in those conditions where very high grafting densities (*i.e.* number of chains per nm^2) are desirable, since these approaches can produce HNPs with up to 1.2 chains/nm^2.[58] Furthermore, "grafting-from" can allow the direct synthesis of block co-polymer shells with specific composition, and NPs with bimodal brushes, *i.e.* different polymers anchored onto the same NP core.[62,63] However, due to the much easier synthetic conditions, lack of contaminants and easier characterization of the polymer shell, "grafting-to" approach may be preferrable when lower grafting densities are required.

1.4.2. Synthesis of HNPs by "grafting-to" approach

In the "grafting-to" synthesis of HNPs, pre-synthesized polymer chains are covalently bound onto the surface of inorganic NPs by using a variety of anchoring approaches, depending on the nature of the inorganic core and the polymer shell. In principle, it is possible directly anchor a polymer chain onto the surface of the NPs by using adequately end-functionalized polymers. Alternatively, smaller anchoring molecules (*e.g.* organosilanes in the case of SiO_2 HNPs) can be used to modify the surface of inorganic NPs with reactive functional groups, which can further react with polymer chains.

One-step grafting with end-functionalized polymers can be achieved in the case of Au NPs, which can directly react with thiol-terminated polymer chains (a in Figure 1.15). Often, thiol-therminated polymers are previously synthesized with the RAFT technique, exploiting the presence of the thioester CTA, which is readily converted to a thiol group.[64,65] For example, Li *et al.*[66] recently reported the grafting of poly(N-isopropylacrylamide) (PNIPAM) and PNIPAM-PEG block co-polymers onto Au NPs. Alternatively, thiol-terminated commercial

polymers can be used. By this approach, Li *et al.*[67] recently studied the regioselective functionalization of "hairy" Au nanorods with a variety of polymers.

Iron oxide (Fe_3O_4) NPs can also be directly grafted with polymer chains by using catecholamines, particularly nitrodopamine, as anchoring groups (b in Figure 1.15). By exploiting this approach, Fe_3O_4 NPs were grafted with polyethylene glycol (PEG) chains, producing highly stabilized NP dispersions.[68–70] Similarly, SiO_2 NPs can be grafted with polymers by exploiting the reaction of surface silanols with succinic anhydride-modified chains (c in Figure 1.15), as reported by Tai *et al.*[71]

Instead of directly grafting polymers onto inorganic NPs, exploiting a two-step anchoring approach can offer increased control and tuning of the grafting process. In this context, several grafting techniques involve the use of "click" chemistry, such as alkyne-azide (d in Figure 1.15), Diels-Alder or thiol-ene reactions.[72] The concept of 'click'-chemistry was introduced by Sharpless *et al.*[73] to refer to universal linkage of molecules without the use of highly reactive intermediates. The so-called "click"-reactions are easily applicable to the functionalization of inorganic NPs with polymers due to the high efficiency, selectivity and mild conditions required for the process.[74]

"Click"-chemistry has been applied to the grafting of various kinds of inorganic NPs with different polymers. For SiO_2 NPs, typically the surface of the NP is functionalized with 3-bromopropyltrichlorosilane, which is then substituted by an azide group. Then, the azide group reacts with alkyne-terminated polymers.[75,76] By following the same approach, Zhang and co-workers reported the synthesis of bioconjugated silica Janus NPs, functionalized on one hemisphere with biotin molecules and on the other with poly(ethylene oxide) (PEO). Mixed functionalization approaches of silica, combining

"grafting-to" by "click" reactions and RAFT/ATRP, have also been reported in the literature.[77–79] Similarly, HNPs with gold[80] and magnetite[81] cores were synthesized by following the "click"-chemistry approach.

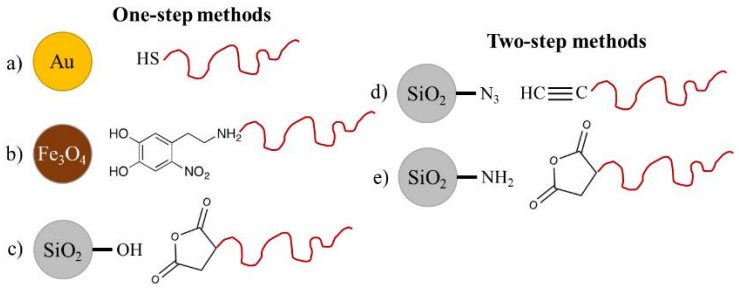

Figure 1.15 The most common "grafting-to" approaches for the synthesis of HNPs. a) Gold-thiol reaction; b) Fe_3O_4-nitrodopamine; c) SiO_2-succinic anhydride; d) alkyne-azide "click" chemistry; e) amine-succinic anhydride reaction.

Recently, an alternative "grafting-to" approach was proposed in the literature exploiting the amine-succinic anhydride reaction (e in Figure 1.15). The amino-groups on the surface of SiO_2 NPs modified with APTES react with succinic anhydride-functionalized polymers. For example, Yuan *et al.*[82] followed this route for the synthesis of SiO_2 HNPs with polypropylene (PP) shells, while Wei *et al.*[83] reported the same approach for polystyrene. Recently, our group has reported a synthesis of SiO_2 HNPs with polybutadiene (PB) shells exploiting the amine-succinic anhydride reaction.[7]

An interesting alternative to traditional "grafting-to" approach is the use of Nanoscale Ionic Materials (NIMs), where the NP/polymer interaction is a ionic bond instead of a covalent bond.[6] This approach

has several advantages, such as the stabilization of the inorganic NP cores during the synthesis process and the possibility of tuning the NP/shell interaction with different strength compared to the typical silane bonds.

1.4.3. "One-pot" synthesis of HNPs

"One-pot" synthesis, also defined "grafting-through", involves the synthesis of the inorganic cores and the simultaneous anchoring of the polymer shells in a single reaction step. Due to the versatile colloidal synthesis of SiO_2 NPs (*see* Paragraph 1.3.2), this grafting approach is often used for silica in combination with modified versions of the Stöber synthesis. The main advantage of this method, compared to other approaches, is the possibility of achieving high dispersion of the NP cores, preventing the aggregation issues that arise with the other two grafting methods. However, this approach can only be applied to polymers that are soluble in the same solvent where the colloidal synthesis of SiO_2 NPs takes place. For this reason, it is mostly applied to the synthesis of SiO_2 with hydrophilic brushes such as PEG.

Different approaches have been developed for the one-pot synthesis of PEGylated SiO_2 NPs. Rio-Echevarria *et al.*[84] designed molecular precursors composed of a hydrophilic PEG chain and a hydrophobic tail with a terminal triethoxysilane group (Figure 1.16). These molecules self-organize in the aqueous reaction mixture in the presence of a surfactant, forming spherical micelles with the lipophilic silane-terminated tail in the center. Once ammonia was added as a catalyst, the core of the HNPs was formed by hydrolysis and condensation while the hydrophilic PEG remains anchored forming the polymer shell. Interestingly, this approach allows the simultaneous doping of SiO_2 NPs with other lipophilic organic molecules for additional functionality, such as drug delivery and signaling.[84]

A mixture of traditional tetraalkoxysilane precursors and PEG without the addition of surfactants were tested.[33,85] Akbari and co-workers[86] studied the effect of ammonia concentration and PEG/TEOS molar ratio on the morphology and wettability of PEGylated SiO_2 HNPs. Similarly, Zhang *et al.* investigated the effect of catalyst concentration on the one-pot synthesis of PEGylated mesoporous SiO_2 HNPs, prepared by using TEOS in combination with a silane-terminated PEG polymer.[87]

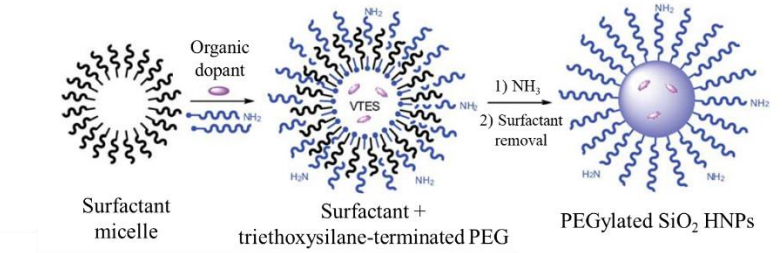

Figure 1.16 Example of one-pot synthesis of PEGylated SiO_2 HNPs. Adapted from Rio-Echevarria *et al.*[84]

1.4.4. Brush conformation: theoretical and empirical models

Among the properties of HNPs, the most significant parameter is the grafting density, σ, previously defined as the number of polymer chains per each unit of surface area (Equation 1.4).

$$\sigma = \frac{chains}{nm^2} \tag{1.4}$$

The conformation of grafted polymer chains is affected by various parameters, such as polymer grafting density, NP size, degree of polymerization of the polymer shell, as well as on the solvent or matrix in which the HNPs are dispersed. The study of the polymer shell

conformation is crucial because it affects the behavior and properties of HNPs. Several studies have been dedicated to understanding and modelling the conformation of polymer chains tethered to NP cores.

The first theoretical model of the conformation of polymer brushes, developped by De Gennes and Alexander in the 1970s,[59,88] predicted that the conformation of a grafted polymer chain and therefore the thickness h of the grafted polymer layer onto a flat surface depended on the grafting density σ of the polymer. When the radius of gyration R_g of the grafted chains is smaller than the average distance between grafting points, the molecules are stretched, and their length is proportional to N, which is the degree of polymerization of the polymer chains.[59] This conformation is known as the concentrated polymer brush (CPB), or simply "brush" regime.

Conversely, when grafting points are placed at a sufficient distance from each other, polymer chains form random coils onto the grafted surface, creating the so-called dilute polymer brush (DPB) or "mushroom" regime. In this case, the thickness of the polymer layer scales like $N^{3/5}$.

Daoud and Cotton[89] extended this model to star polymers, consisting of a spherical polymer core with radius r_0 with f polymer chains of monomer length l grafted around it. The degree of polymerization of the polymer chains N is uniform and the polymers are considered to be immersed in a good solvent. Due to curvature effects in the case of star polymers (differently from polymers grafted onto a flat surface), the polymer conformation is also a function of the distance from the core. By dividing the polymer branches into spherical "blobs", Daoud and Cotton distinguished two different regions in the star polymer regime: the unswollen region, close to the star polymer core, where the polymer is more concentrated, and the swollen region, far from the core, where the polymer is more diluted.

Star polymers are similar to HNPs, because they are both constituted by polymer chains grafted to a spherical core. Ohno *et al.*[90] and Dukes *et al.*[91] extended this theoretical framework to the case of HNPs, studying the effect of the degree of polymerization N and grafting density σ on chain conformation. In particular, they introduced the reduced grafting density σ* (Equation 4.5).

$$\sigma^* = \sigma \cdot l^2 \tag{1.5}$$

where l is the monomer length.

Based on these two parameters, their results are summarized in Table 1.1. Briefly, three possible regimes were identified for polymer chains grafted onto NPs (Figure 1.17): the "mushroom" regime, the semi-dilute polymer brush or SDPB regime and the concentrated polymer brush or CPB regime, each of which shows a different dependence on grafting density and polymerization degree.

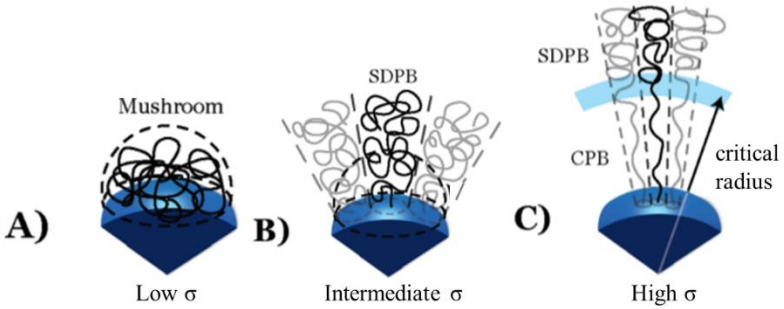

Figure 1.17 Schematic representation of a) mushroom regime, b) semi-dilute polymer brush and c) concentrated polymer brush for HNPs. Adapted from Dukes *et al.*[91]

Table 1.1 Conformation of polymer brushes and scaling of the polymer shell thickness *h* as a function of polymerization degree *N* and reduced grafting density σ^* for flat and spherical surfaces.

Curvature	**Conformation**	**Scaling of *h* with *N*, σ^***
flat/spherical	Mushroom	$N^{3/5}$
flat	SDPB	$N^{1}\sigma^{*1/3}$
flat	CPB	$N^{1}\sigma^{*1/2}$
spherical	SDPB	$(N\sigma^{*1/3})^{3/5}$
spherical	CPB	$(N\sigma^{*1/2})^{x}$, $3/5 < x \leq 1$

Since the HNPs surface is curved, the polymer chains are more densely packed close to the surface of the core. For this reason, Ohno *et al.*[90] determined the presence of a critical radius r_c that marks the transition between the CPB regime (closer to the core) and SDPB regime in HNPs (Equation 1.6):

$$r_c = r_0\sigma^{*1/2}\nu^{*-1} \tag{1.6}$$

where ν^* is a steric parameter, and r_0 is the radius of the HNP core.

As a general rule, sparsely grafted HNPs will exhibit "mushroom"-type conformation of polymer chains. Because of steric effects, HNPs synthesized by "grafting-to" will be generally in the mushroom regime, while HNPs synthesized by "grafting-from" will exhibit SDPB or CPB conformations. A good way to easily estimate the polymer shell regime of HNPs based on grafting density and radius of gyration R_g of the polymer shell was proposed by Brittain *et al*,[92]

introducing the *reduced tethered density* Σ, defined as follows (Equation 1.7):

$$\Sigma = \sigma \, \pi \, R_g^2 \qquad (1.7)$$

Then, based on the average results from several studies, they identified three possible regimes depending on the value of Σ: the mushroom regime at $\Sigma < 1$, mushroom-to-brush transition regime at $1 < \Sigma < 5$, and brush regime at $\Sigma > 5$. It is important to point out that R_g of the polymer depends on the solvent, and thus solvent effects can impact the polymer conformation in HNPs.

1.4.5. Applications of HNPs

Due to their combination of unique properties, HNPs can be applied to a plethora of different fields: catalysis, nanomedicine, smart materials, coatings and so on. HNPs find their most promising applications in the field of NCs, to enhance their mechanical and functional properties. Their applications in PNCs will be discussed in the following section.

Although metallic NPs (MNPs) and nanoalloys are used in solution, commonly as aqueous suspensions of MNPs, the use of free MNPs as catalysts poses several issues, such as the difficulty of retrieving and re-using the catalysts, stability issues related to aggregation and ripening phenomena of the MNPs, as well as environmental and health hazards. To overcome this drawback, Ballauf and co-workers designed several systems composed of MNPs anchored to the polymer corona of HNPs (a in Figure 1.18).[93] They used NPs of PP, coated with a polyelectrolyte shell, such as poly(aminoethyl methacrylate hydrochloride) (PAEMH), which was grafted by using a photopolymerization "grafting-from" approach. Metallic ions were introduced into the cationic shell by substitution of the Cl^- counterions with $AuCl_4^-$ ions. Once introduced, the gold ions were reduced by

$NaBH_4$ to their metallic state, generating fine gold NPs anchored to the polyelectrolyte shell (b in Figure 1.18). The same approach was later reproduced with other noble metal NPs, such as Pt,[94] Ag,[95,96] and Rh.[96]

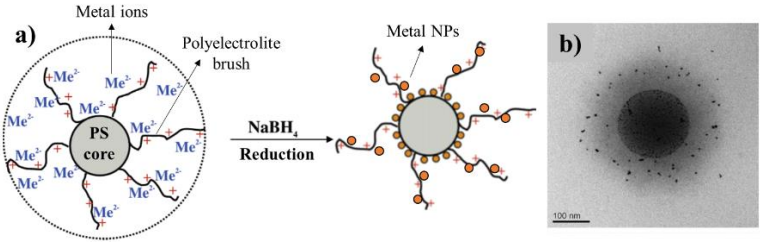

Figure 1.18 a) Schematic representation of the synthesis of metal NPs supported on HNPs (adapted from Mei *et al.*[94]) and b) TEM image of Au NPs embedded within an HNP polymer shell (adapted from Lu *et al.*[96]).

Recent developments of this approach consist in the use of HNPs not only as passive carriers, but also as active carrier of catalytically active MNPs. Stimuli-responsive brushes, such as thermosensitive poly(N-isopropylacrylamide) (PNIPAM), were used to control catalytic processes. Furthermore, this approach has recently been extended to SiO_2 HNPs[97] and Janus SiO_2 HNPs.[98]

Mesoporous silica NPs (MSNs) grafted with various stimuli-responsive polymers (e.g. pH, temperature, ultrasound…) were considered as carriers for targeted drug delivery.[99,100] By exploiting the change of conformation of the polymer shell in response to the environment, the mesopores of drug-loaded MSNs can be selectively opened and closed to release molecules in targeted areas of the body.

For example, Tian *et al.* prepared pH-responsive drug carriers for chemotherapy by anchoring polyacrylamide (PAA) onto MSNs in a two-step "grafting-to" approach.[101] In the case of nonporous NPs,

polymer shells may also be used to encapsulate and selectively release specific molecules. Dutta *et al.*[102] grafted a temperature and pH dual-responsive block co-polymer onto the surface of magnetic iron oxide NPs by using a RAFT polymerization approach. HNPs were used to load and release doxorubicin, a model anticancer drug.

1.5. Self-assembly

Self-assembly, also referred to as self-organization, is one of the most pervasive and fascinating phenomena in nature and technology. In an article published in 2002 in Science, Whitesides and Grzybowski[103] defined self-assembly as *the autonomous organization of components into patterns or structures without human intervention*. This definition is very general and can be applied at all scales, from molecules and nanomaterials to the macroscopic and planetary scale. Self-assembly can be seen in action across a variety of different phenomena, from the growth of crystals to viruses, from flocks of birds to living cells.

In general, as Iyer *et al.*[104] have highlighted, self-assembly is interesting because of three main reasons:

- Self-assembly is central to the understanding of the behavior of living organism.
- Self-assembly opens new possibilities for technology by offering an alternative approach to building structures. This is particularly useful on the nanoscale, where direct manipulation is challenging.
- Self-assembly is not restricted to the molecular scale or nanoscale, but can also be applied to macroscopic systems, finding applications in fields such as robotics and computer science.

Self-assembly emerged as an important concept in theoretical and applied sciences during the 1970s. The origins of this idea may be

traced back to the work of von Bertalanffy,[105] who suggested that systems composed of a number of interacting elements, i.e. complex systems, could show emergent properties of self-organization. This idea was later extended by Maturana and Varela,[106] who introduced the concept of *autopoiesis* to refer to the ability of material structures, such as living systems, to self-organize in ordered and dynamic systems.

Although there are several examples of the application of the principles of self-assembly to macroscopic structures, the interest in the concept of self-assembly has increased due to the rise of nanomaterials starting from the 2000s. Indeed, the large potential of nanomaterials lies in the possibility of exploiting the interactions of multiple components in a very small volume. In contrast with early conceptions of nanotechnology, which favored direct molecular manipulation, nanotechnology now relies on a variety of self-assembly approaches to achieve control on the nanoscale.

Self-assembly phenomena are typically classified as either static or dynamic.[103] In static self-assembly, structures are in a local or global state of equilibrium, and thus, once formed, they don't exchange energy or matter with the surrounding environment. This is the case of molecular crystals, colloidal crystals, liquid crystals and certain biological structures such as viruses and cell membranes. One of the first examples of "in-vitro" static self-assembly was the study of the self-organization of the Tobacco Mosaic Virus (TMV) protein capsid, realized by in 1955 by Fraenkel-Conrat and Williams.[107]

Dynamic self-assembly, on the other hand, requires energy dissipation to sustain the system in an ordered state. For this reason, the structures formed by processes of dynamic self-assembly are also defined as "dissipative structures" and were first studied in the 1970s by Prigogine.[108] Although dynamic self-assembly is mostly associated to

living systems, there are examples of this phenomenon in inorganic systems as well. For example, Rayleigh-Bénard convection cells are ordered structures that spontaneously form when a liquid in a dish is heated from below and immediately disassemble once the heat source is removed.

1.5.1. Self-assembly of inorganic NPs

Self-assembly in systems composed of objects in the nanoscale always results from a balance between attractive and repulsive interactions, as well as from the impact of external forces on the system. Understanding the nature of these interactions and controlling them by tuning the properties of the building blocks is crucial to exploit the full potential of self-assembly.[109]

In general, depending on the properties of the building blocks and the type of interactions taking place, the resulting NPs assemblies can be either isotropic or anisotropic. Typically, isotropic building blocks, *e.g.* bare spherical NPs, will self-organize in isotropic, close-packed structures such as face-centered cubic (*fcc*) or hexagonal close-packed (*hcp*) superlattices. Conversely, in the case of anisotropic building blocks, or as a result of a specific balance of attractive and repulsive forces in the case of spherical NPs, anisotropic self-assembly can occur.[110]

Depending on the driving force of the organization, self-assembly of NPs can be classified as either spontaneous[110] or directed.[111] Spontaneous self-assembly can result from a balance of Van der Waals, electrostatic, steric and depletion forces, as well as elastic and osmotic effects.[109] It is very common in anisotropic NPs.

Anisotropic NPs are some of the most effective building blocks for self-assembly.[112] Amongst inorganic NPs, self-organization of gold nanorods (Au NRs) has been widely investigated, for example by Sau *et al.*[113] It is established that NRs tend to spontaneously form side-by-

side assemblies as a result of increased Van der Waals attraction. In addition, self-assembly of NRs is driven by "depletion attraction", an effect of entropic origin produced by the exclusion of macromolecules from the volume between two particles.[109,114] By exploiting this mechanism, Baranov *et al.* was able to trigger self-assembly of CdSe NRs in presence of macromolecular additives, as shown in Figure 1.19.[115]

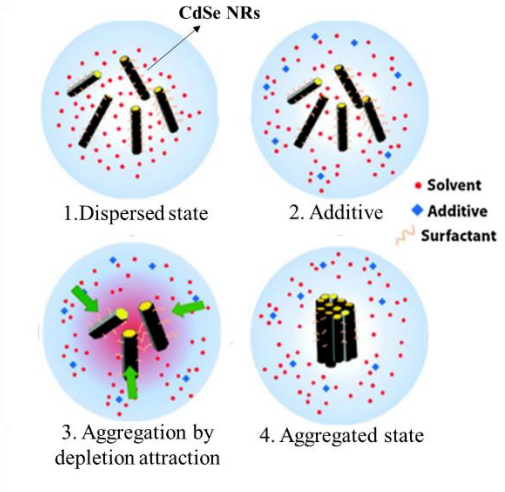

Figure 1.19 Example of aggregation by depletion attraction of CdSe NRs due to the presence of an organic additive. Adapted from Baranov *et al.*[115]

Spontaneous self-assembly of spherical NPs may result from electrostatic interactions. Kalsin and co-workers[116] functionalized spherical Au and Ag NPs with two oppositely charged organic moieties and observed their spontaneous self-organization into three-dimensional diamond-like structures. In these structures, each charged NP was surrounded by four oppositely charged neighbors.

Alternatively, the self-assembly of spherical NPs was achieved by exploiting fluid interfaces, as in the case of Pickering emulsions.[60] In 1907, firstly Pickering discovered that paraffin-in-water emulsions could be stabilized by the presence of colloidal particles.[117] In Pickering emulsions, the stabilization of the dispersed phase is produced by the presence of inorganic NPs located at the interface between the two liquid phases. Pickering emulsions are often used as stabilizers, as well as to design novel composite nanomaterials with hierarchical structures[118] and for the synthesis of Janus NPs.[119]

Directed self-assembly, on the other hand, takes place in response to external fields or templates which drive the self-organization of NPs.[110] Singh *et al.* found that magnetite nanocubes deposited on a liquid-air interface and immersed in a magnetic field self-assemble in helical structures as a result of a balance between the magnetic and Van der Waals interactions.[120]

Self-assembly of NPs can also be directed by the presence of templating agents such as block co-polymers (BCPs). Recently, Yu *et al.* proposed a co-assembly strategy of polystyrene (PS)-grafted Au NPs and a polystyrene-block-poly (4-vinylpyridine) BCP.[121] By exploiting the affinity of the BCP and PS-grafted NPs, they were able to prepare spherical BCP vesicles with Au NPs confined within the vesicle walls.

Finally, it is significant to point out that NP assemblies can also exhibit stimuli-responsive properties. Reversible self-assembly of NPs can arise from solvent effects, changes in pH, temperature, light and presence of metal ions, to name a few.[122] For example, Chan *et al.*[123] investigated the self-assembly, disassembly and re-assembly of Au NRs mediated by [(disulfide-modified terpyridine)$_2$–M^{II}] complexes. They found that upon addition of Fe(II) or Cd(II), in the presence of a

terpyridine linker, the Au NRs could spontaneously organize in self-assembled and reversible string-like structures.

1.5.2. NPs self-assembly in PNCs

Self-assembly of inorganic NPs in PNCs is a promising strategy to tailor and enhance the mechanical and functional properties (e.g. dielectric properties,[2] thermal conductivity,[124] electrical conductivity[125]) of materials. There are several strategies to achieve self-assembly in PNCs.

One possible approach is the "bricks and mortar" strategy defined by Arumugam *et al.*,[126] where the self-assembly of inorganic NPs (the "bricks") is produced by hydrogen bonding or electrostatic interactions with specific functional groups on the polymer matrix (the "mortar"). Alternative approaches do not require the functionalization of the polymer matrix but rely on the balance of weak attractive and repulsive interactions between filler NPs.

In this context, two different strategies can be identified, namely i) the use of anisotropic filler NPs and ii) the use of spherical HNPs in homopolymer matrices.

1.5.2.1. Self-assembly of anisotropic NPs in PNCs

The simplest approach to obtain self-organization in PNCs is to use anisotropic NPs. Anisotropic NPs, such as nanofibers and NRs, can spontaneously align forming ordered domains within the polymer matrix. This may lead to an improvement of the PNC's functional properties.

For example, Modestino and co-workers[127] have studied the self-assembly of semiconductive CdSe NRs coated with alkyl chains and dispersed in thin films. They found that the NRs align along the longest axis forming an ordered filler network independent of the chemical nature of the polymer matrix, as shown in Figure 1.20 a. This

self-assembly behavior can be switched off by changing the surface chemistry of the NRs, e.g. by addition of pyridine ligands.

Similarly, Zhang *et al.*[128] used an electrospinning technique to prepare PNCs containing Au NRs dispersed in a PVA matrix. They found that the NRs preferentially arrange themselves along the axial direction of the electrospun PVA nanofibers, forming highly ordered anisotropic domains (b in Figure 1.20). This self-assembly provided enhanced optical properties in the final materials.

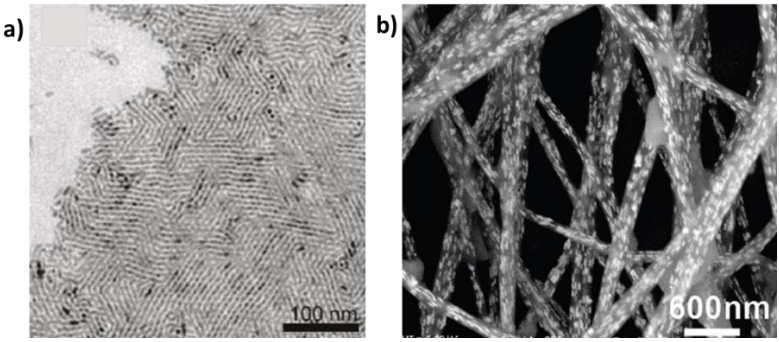

Figure 1.20 a) Anisotropic self-assembly of CdSe NRs in a poly(3-hexylthiophene) (P3HT) matrix. Adapted from Modestino et al.[127] b) Anisotropic arrangement of Au NRs in PVA electrospun fibers. Adapted from Zhang et al.[128]

The effect of anisotropic SiO_2 NPs in styrene-butadiene rubber (SBR) NCs was investigated recently in our group by Tadiello *et al.*[10] Rod-like SiO_2 NPs with varying aspect ratio (AR from 1 to 5)[10] as fillers in SBR NCs, and investigated their morphological and dynamic mechanical properties. They found that increasing the aspect ratio of SiO_2 NPs increased the reinforcement of NCs (a in Figure 1.21). TEM analysis revealed that this improvement of the mechanical properties was related to the self-organization of SiO_2 NPs in ordered domains

within the polymer matrix, which in turn increased the amount of rigid rubber enclosed within the NPs clusters (a' in Figure 1.21).

Similarly, Di Credico *et al.*[11] found that clay fibers, after acid treatment, produced nanosized sepiolite (NS-Sep), that dispersed within SBR NCs self-organize in ordered structures. NCs prepared with NS-Sep, also modified with silane coupling agent, produced a significant improvement on dynamic mechanical properties respect to those prepared with untreated Sep, especially reinforcement (storage modulus G' at low strain) and Payne effect (difference between G' at high strain and G' at low strain) (b in Figure 1.21). By testing the morphology of the NCs with both TEM and AFM analysis, Cobani *et al.*[12] found that this improvement of the mechanical properties was related to the formation of anisotropic domains, characterized by an increased amount of rigid rubber in the NCs (b' in Figure 1.21).

These two examples indicate that the control of filler distribution within rubber NCs via self-assembly is crucial to obtain materials with desired mechanical properties, such as high reinforcement, low Payne effect and low hysteresis.

Literature evidence suggests that the self-assembly of anisotropic NPs in ordered structures is the spontaneous result of entropic effects even in the absence of attractive potentials between the NPs.[129,130] This effect, also known as depletion attraction, is due to the maximization of the free volume available for the polymer matrix or solvent, which in turn increases the degree of conformational entropy of the medium of the NPs suspension. However, in the case of rubber NCs, there are additional forces at play. Enthalpic effects, such as electrostatic and Van der Waals interactions, may play a role depending on the surface chemistry of the NPs. In the case of silica, hydrophilic surface silanol groups exert a short-range attractive force, favoring aggregation, while surface modification with organosilane molecules favors the

dispersion of the NPs within the polymer matrix.[11] Overall, the self-organization of anisotropic NPs results from a delicate balance of all these interactions.

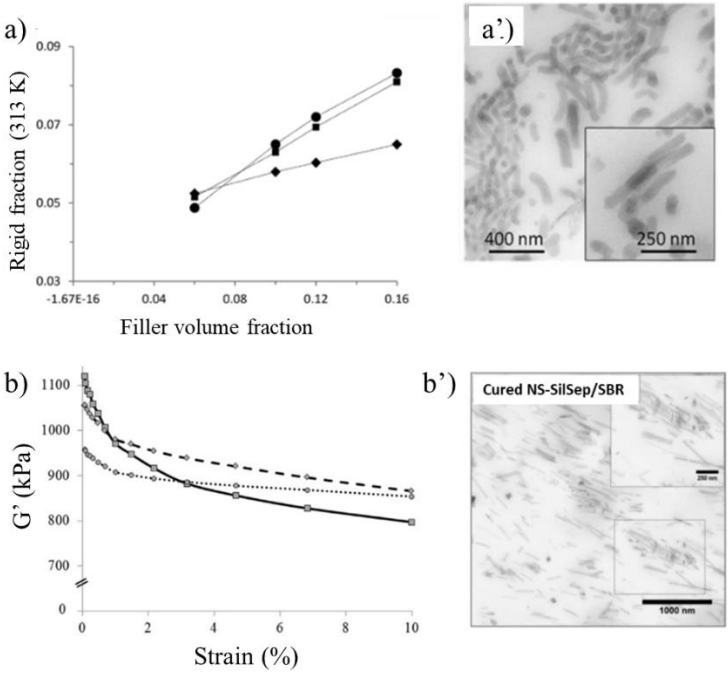

Figure 1.21 a) Fraction of rigid rubber for SiO_2 with aspect ratio 1 (♦), 3 (■) and 5 (●) vs. volume fraction of filler and a') TEM image of cured NC prepared with SiO_2 with aspect ratio 5, showing evidence of self-assembly (adapted from Tadiello *et al.*).[10] b) Storage modulus G' vs. strain for NCs filled with untreated Sep (full line), NS Sep (dotted line) and silanized NS Sep (dashed line) and b') TEM image of cured NC prepared with silanized NS Sep, showing evidence of self-assembly (adapted from Di Credico *et al.*).[11]

1.5.2.2. Self-assembly of spherical HNPs

While the self-assembly of anisotropic NPs in PNCs is an established strategy, accurately controlling the distribution of spherical NPs in polymer matrices remains a challenge. In this context, several papers have reported the use of directed assembly approaches to induce the formation of ordered domains of NPs within PNCs.

One common strategy of directed assembly is the use of block co-polymers. Zhao and co-workers[131] exploited hydrogen bonding to direct the assembly of surface-modified CdSe and PbS NPs in a polystyrene-block-poly(4-vinyl pyridine) (PS-b-P4VP) block co-polymer matrix. They obtained anisotropic assemblies of spherical NPs with thermal- and light-responsive properties. Shear stress has also been shown to generate directed self-assembly of spherical NPs in PNCs. Zhang *et al.*[132] used a soft-shear dynamic zone annealing (DZA-SS) process to generate unidirectionally aligned AuNPs domain structures in nanocomposite films. In detail, Au HNPs densely grafted with polystyrene (PS) were mixed in a poly(methylmethacrylate) (PMMA) matrix, resulting in phase-separated morphologies. Application of oscillatory shear stress resulted in the formation of stable string-like anisotropic structures.

SiO_2 HNPs are known to produce spontaneous self-assembly in homopolymer matrices. In 2009, Akcora and co-workers[9] found that spherical SiO_2 HNPs sparsely grafted with PS chains and dispersed in a PS matrix can self-organize higher order in anisotropic structures. The formation and morphology of the self-assembled HNP structures depends on several crucial parameters:

- HNPs grafting density σ (chains/nm^2);
- length of grafted polymer, N;
- length of matrix polymer, P;

- concentration of HNPs in the polymer matrix;
- size and dispersity[133] of SiO_2 cores.

In detail, they used colloidal SiO_2 NPs of 14±4 nm grafted by a RAFT grafting-from approach and fixed the concentration of HNPs at 5 wt%. The grafting density, molecular weight of tethered polymer and molecular weight of the matrix were varied to achieve different self-assembly conditions resulting in the formation of various structures, namely small clusters, strings, sheets and well-dispersed HNPs (Figure 1.22).

Combining these results with others found in the literature, Kumar *et al.* proposed a morphology diagram predicting the formation of self-assembled HNPs structures in polymer NCs. They found that the self-organization process was controlled by two parameters: the ratio between the polymerization degree of grafted chains (N) and the polymerization degree of the matrix (P), $\alpha \equiv N/P$, and the product $\sigma \cdot N^{0.5}$ (Figure 1.22).

Although the study of self-assembly of spherical HNPs in polymer NCs was mostly focused on high glass transition temperature (T_g) polymers, such as PS, recently Bonnevide *et al.*[134] prepared polyisoprene (PI)-grafted SiO_2 HNPs via RAFT and dispersed them in PI and styrene-butadiene rubber (SBR) matrices. They found that the PI-grafted SiO_2 HNPs self-organize in anisotropic structures like those predicted by Kumar and co-workers.[8]

Several theoretical studies have investigated the interactions that determine the formation of anisotropic self-assembled structures of SiO_2 HNPs. Most models agree that self-assembly of sparsely grafted NPs results from a balance of attractive and repulsive interactions of both enthalpic and entropic origin.

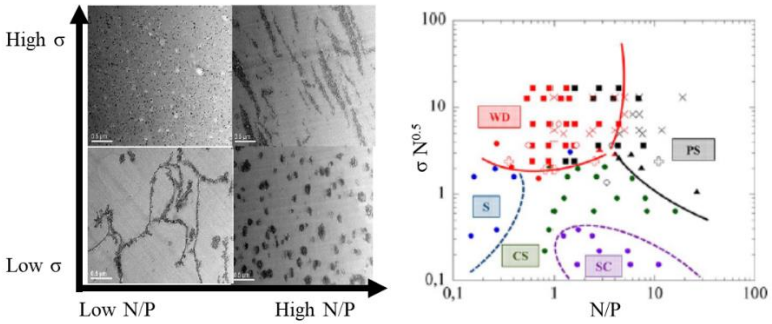

Figure 1.22 Self-organized structures of PS-grafted SiO_2 HNPs dispersed in PS matrices. WD: well-dispersed, PS: phase separated, S: strings, CS: connected sheets, SC: small clusters. Adapted from Kumar *et al*.[8]

In detail, the interaction of grafted polymer chains with a chemically identical polymer matrix depends on an effect known as *autophobic dewetting*.[135–137] When the ratio between grafted chain length N and matrix length P is sufficiently small, an increase in mixing entropy drives the free matrix chains within the grafted polymer brush, producing a repulsive effect. On the other hand, when N/P is large enough, the loss of conformational entropy of the polymer brush drives the matrix chains away from the HNPs, producing aggregation.

In this framework, it is important to note that in the case of low grafting densities, the energetic contribution due to Van der Waals attraction between the inorganic cores can play a significant role, driving the HNPs towards phase separation.[8,138] This effect is particularly significant for smaller NPs with higher surface area. A balance of these repulsive and attractive interactions is believed to produce the variety of self-assembled structures observed experimentally.

Interestingly, it has been found that these self-organized structures influence the mechanical properties of polymer NCs. Moll and co-workers[139] investigated the mechanical properties of PS NCs prepared with PS-grafted SiO_2 at varying grafting density and found that maximum reinforcement was achieved with intermediate grafting densities, resulting in the formation of an extended self-organized filler network. However, an in-depth investigation of the impact of self-assembly on reinforcement and hysteresis in rubber NCs has yet to be conducted.

1.6. Bibliography

1 L. Tadiello, M. D'Arienzo, B. Di Credico, T. Hanel, L. Matejka, M. Mauri, F. Morazzoni, R. Simonutti, M. Spirkova and R. Scotti, *Soft Matter*, 2015, **11**, 4022–4033.

2 M. Crippa, A. Bianchi, D. Cristofori, M. D'Arienzo, F. Merletti, F. Morazzoni, R. Scotti and R. Simonutti, *J. Mater. Chem. C*, 2013, **1**, 484–492.

3 S. Mostoni, M. D'Arienzo, B. Di Credico, L. Armelao, M. Rancan, S. Dirè, E. Callone, R. Donetti, A. Susanna and R. Scotti, *Ind. Eng. Chem. Res.*, 2021, **60**, 10180–10192.

4 P. Dwivedi, S. S. Narvi and R. P. Tewari, *J. Appl. Biomater. Funct. Mater.*, 2013, **11**, 129–142.

5 S. Fu, Z. Sun, P. Huang, Y. Li and N. Hu, *Nano Mater. Sci.*, 2019, **1**, 2–30.

6 N. J. Fernandes, D. C. Company, H. Koerner, A. Force and E. Giannelis, *MRS Commun.*, 2013, **3**, 13–29.

7 L. Tripaldi, E. Callone, M. D'Arienzo, S. Dirè, L. Giannini, S. Mascotto, A. Meyer, R. Scotti, L. Tadiello and B. Di Credico, *Soft Matter*, 2021, **17**, 9434–9446.

8 S. K. Kumar, N. Jouault, B. Benicewicz and T. Neely, *Macromolecules*, 2013, **46**, 3199–3214.

9 P. Akcora, H. Liu, S. K. Kumar, J. Moll, Y. Li, B. C. Benicewicz, L. S. Schadler, D. Acehan, A. Z. Panagiotopoulos, V. Pryamitsyn, V.

Ganesan, J. Ilavsky, P. Thiyagarajan, R. H. Colby and J. F. Douglas, *Nat. Mater.*, 2009, **8**, 354–359.

10 R. Scotti, L. Conzatti, M. D'Arienzo, B. Di Credico, L. Giannini, T. Hanel, P. Stagnaro, A. Susanna, L. Tadiello and F. Morazzoni, *Polymer (Guildf).*, 2014, **55**, 1497–1506.

11 B. Di Credico, E. Cobani, E. Callone, L. Conzatti, D. Cristofori, M. D'Arienzo, S. Dirè, L. Giannini, T. Hanel, R. Scotti, P. Stagnaro, L. Tadiello and F. Morazzoni, *Appl. Clay Sci.*, 2018, **152**, 51–64.

12 E. Cobani, I. Tagliaro, M. Geppi, L. Giannini, P. Leclère, F. Martini, T. C. Nguyen, R. Lazzaroni, R. Scotti, L. Tadiello and B. Di Credico, *Nanomaterials*, 2019, **9**, 486.

13 M. M. Shameem, S. M. Sasikanth, R. Annamalai and R. G. Raman, *Mater. Today Proc.*, 2021, **45**, 2536–2539.

14 W. S. Khan, N. N. Hamadneh and W. A. Khan, *Sci. Appl. Tailored Nanostructures*, 2016, 50–67.

15 B. M. Novak, *Adv. Mater.*, 1993, **5**, 422–433.

16 H. S. Aldhufairi and O. A. Olatunbosun, *Proc. Inst. Mech. Eng. Part D J. Automob. Eng.*, 2018, **232**, 1865–1882.

17 X. Qin, B. Han, J. Lu, Z. Wang, Z. Sun, D. Wang, T. P. Russell, L. Zhang and J. Liu, *Nano Energy*, 2018, **48**, 180–188.

18 J. Araujo-Morera, M. H. Santana, R. Verdejo and M. A. López-Manchado, *Polymers (Basel).*, 2019, **11**, 1–13.

19 S. Nie, J. Lacayo-Pineda and M. Wilhelm, *Soft Mater.*, 2019, **17**, 269–282.

20 C. W. Nan, Y. Shen and J. Ma, *Annu. Rev. Mater. Res.*, 2010, **40**, 131–151.

21 A. R. Payne, *J. Appl. Polym. Sci.*, 1962, **6**, 368–372.

22 H. E. Bergna and W. O. Roberts, *Colloid. Silica Fundam. Appl.*, 2005, 1–897.

23 E. D. E. R. Hyde, A. Seyfaee, F. Neville and R. Moreno-Atanasio, *Ind. Eng. Chem. Res.*, 2016, **55**, 8891–8913.

24 J. G. Croissant, K. S. Butler, J. I. Zink and C. J. Brinker, *Nat. Rev.*

Mater., 2020, **5**, 886–909.

25 P. P. Ghimire and M. Jaroniec, *J. Colloid Interface Sci.*, 2021, **584**, 838–865.

26 W. Stöber, A. Fink and E. Bohn, *J. Colloid Interface Sci.*, 1968, **26**, 62–69.

27 I. A. Rahman and V. Padavettan, *J. Nanomater.*, , DOI:10.1155/2012/132424.

28 T. Matsoukas and E. Gulari, *J. Colloid Interface Sci.*, 1988, **124**, 252–261.

29 G. H. Bogush and C. F. Zukoski IV, *J. Colloid Interface Sci.*, 1991, **142**, 1–18.

30 S. Li, Q. Wan, Z. Qin, Y. Fu and Y. Gu, *Langmuir*, 2015, **31**, 824–832.

31 G. H. Bogush, M. A. Tracy and C. F. Zukoski, *J. Non. Cryst. Solids*, 1988, **104**, 95–106.

32 R. S. Fernandes, I. M. Raimundo and M. F. Pimentel, *Colloids Surfaces A Physicochem. Eng. Asp.*, 2019, **577**, 1–7.

33 H. Xu, F. Yan, E. E. Monson and R. Kopelman, *J. Biomed. Mater. Res. - Part A*, 2003, **66**, 870–879.

34 S. K. Park, K. Do Kim and H. T. Kim, *Colloids Surfaces A Physicochem. Eng. Asp.*, 2002, **197**, 7–17.

35 C. G. Tan, B. D. Bowen and N. Epstein, *J. Colloid Interface Sci.*, 1987, **118**, 290–293.

36 L. T. Zhuravlev, *Colloids Surfaces A Physicochem. Eng. Asp.*, 2000, **173**, 1–38.

37 A. van Blaaderen and A. P. M. Kentgens, *J. Non. Cryst. Solids*, 1992, **149**, 161–178.

38 T. I. Suratwala, M. L. Hanna, E. L. Miller, P. K. Whitman, I. M. Thomas, P. R. Ehrmann, R. S. Maxwell and A. K. Burnham, *J. Non. Cryst. Solids*, 2003, **316**, 349–363.

39 F. Kunc, V. Balhara, Y. Sun, M. Daroszewska, Z. J. Jakubek, M. Hill, A. Brinkmann and L. J. Johnston, *Analyst*, 2019, **144**, 5589–5599.

40 S. Kango, S. Kalia, A. Celli, J. Njuguna, Y. Habibi and R. Kumar, *Prog. Polym. Sci.*, 2013, **38**, 1232–1261.

41 H. Li, X. Chen, D. Shen, F. Wu, R. Pleixats and J. Pan, *Nanoscale*, 2021, **13**, 15998–16016.

42 T. Yokoi, H. Yoshitake and T. Tatsumi, *J. Mater. Chem.*, 2004, 951–957.

43 N. Tang, X. Liu, M.-R. Jia, X.-Y. Shi, J.-W. Fu, D.-X. Guan and L. Q. Ma, *Chemosphere*, 2021, 132771.

44 M. Z. Sarker, M. M. Rahman, H. Minami, T. Suzuki and H. Ahmad, *Colloid Polym. Sci.*, , DOI:10.1007/s00396-021-04910-w.

45 E. Metwalli, D. Haines, O. Becker, S. Conzone and C. G. Pantano, *J. Colloid Interface Sci.*, 2006, **298**, 825–831.

46 C. Jiang, R. Lyu, T. Zhang and Z. Yang, *Environ. Technol. Innov.*, 2021, **24**, 101925.

47 V. Rizzi, J. Gubitosa, P. Fini, S. Nuzzo and P. Cosma, *Sustain. Mater. Technol.*, 2020, **26**, e00231.

48 Y. He, L. Luo, S. Liang, M. Long and H. Xu, *J. Biomater. Appl.*, 2017, **32**, 524–532.

49 X. Wang, C. Li, N. Fan, J. Li, H. Zhang, L. Shang, Z. He and J. Sun, *Asian J. Pharm. Sci.*, 2019, **14**, 405–412.

50 H. Aghahosseini, M. R. Saadati, S. J. T. Rezaei, A. Ramazani, N. Asadi, H. Yahiro, M. Mori, N. Shajari and A. R. Kazemizadeh, *Sci. Rep.*, 2021, **11**, 1–11.

51 P. M. Dietrich, C. Streeck, S. Glamsch, C. Ehlert, A. Lippitz, A. Nutsch, N. Kulak, B. Beckhoff and W. E. S. Unger, *Anal. Chem.*, 2015, **87**, 10117–10124.

52 K. J. Kim, *J. Appl. Polym. Sci.*, 2012, **124**, 2937–2944.

53 J. W. ten Brinke, S. C. Debnath, L. A. E. M. Reuvekamp and J. W. M. Noordermeer, *Compos. Sci. Technol.*, 2003, **63**, 1165–1174.

54 B. Ahn, J. Y. Lee, D. Kim, I. J. Kim, S. Han and W. Kim, *Rubber Chem. Technol.*, 2020, **93**, 414–428.

55 D. H. Napper, *Polymeric Stabilization of Colloidal Dispersions*,

Academic Press, London, 1984.

56 B. Vincent, *Chem. Eng. Sci.*, 1993, **48**, 429–436.

57 N. J. Fernandes, H. Koerner, E. P. Giannelis and R. A. Vaia, *MRS Commun.*, 2013, **3**, 13–29.

58 A. J. Chancellor, B. T. Seymour and B. Zhao, *Anal. Chem.*, 2019, **91**, 6391–6402.

59 P. G. de Gennes, *Macromolecules*, 1980, **13**, 1069–1075.

60 S. K. Ghosh and A. Böker, *Macromol. Chem. Phys.*, , DOI:10.1002/macp.201900196.

61 N. P. Truong, G. R. Jones, K. G. E. Bradford, D. Konkolewicz and A. Anastasaki, *Nat. Rev. Chem.*, , DOI:10.1038/s41570-021-00328-8.

62 A. Rungta, B. Natarajan, T. Neely, D. Dukes, L. S. Schadler and B. C. Benicewicz, *Macromolecules*, 2012, **45**, 9303–9311.

63 D. Zhao, M. Di Nicola, M. M. Khani, J. Jestin, B. C. Benicewicz and S. K. Kumar, *ACS Macro Lett.*, 2016, **5**, 790–795.

64 K. Kusolkamabot, P. Sae-Ung, N. Niamnont, K. Wongravee, M. Sukwattanasinitt and V. P. Hoven, *Langmuir*, 2013, **29**, 12317–12327.

65 B. J. Kim, G. H. Fredrickson, C. J. Hawker and E. J. Kramer, *Langmuir*, 2007, **23**, 7804–7809.

66 C. Li, C. Wang, Z. Ji, N. Jiang, W. Lin and D. Li, *Eur. Polym. J.*, 2019, **113**, 404–410.

67 F. Li, K. Wang, Z. Tan, C. Guo, Y. Liu, H. Tan, L. Zhang and J. Zhu, *Langmuir*, 2020, **36**, 15162–15168.

68 E. Amstad, T. Gillich, I. Bilecka, M. Textor and E. Reimhult, *Nano Lett.*, 2009, **9**, 4042–4048.

69 N. Gal, V. Charwat, B. Städler and E. Reimhult, *ACS Biomater. Sci. Eng.*, 2019, **5**, 4355–4365.

70 A. Lassenberger, O. Bixner, T. Gruenewald, H. Lichtenegger, R. Zirbs and E. Reimhult, *Langmuir*, 2016, **32**, 4259–4269.

71 Y. Tai, J. Qian, Y. Zhang and J. Huang, *Chem. Eng. J.*, 2008, **141**,

354–361.

72 S. Srivastava, S. Choudhury, A. Agrawal and L. A. Archer, *Curr. Opin. Chem. Eng.*, 2017, **16**, 92–101.

73 H. C. Kolb, M. G. Finn and K. B. Sharpless, *Angew. Chemie - Int. Ed.*, 2001, **40**, 2004–2021.

74 N. Li and W. H. Binder, *J. Mater. Chem.*, 2011, **21**, 16717–16734.

75 G. Bissadi and R. Weberskirch, *Polym. Chem.*, 2016, **7**, 1271–1280.

76 S. S. Balamurugan, E. Soto-Cantu, R. Cueto and P. S. Russo, *Macromolecules*, 2010, **43**, 62–70.

77 J. Chen, M. Liu, C. Chen, H. Gong and C. Gao, *ACS Appl. Mater. Interfaces*, 2011, **3**, 3215–3223.

78 W. Li, Y. Xu, Y. Zhou, W. Ma, S. Wang and Y. Dai, *Nanoscale Res. Lett.*, 2012, **7**, 1.

79 Y. Huang, T. Hou, X. Cao, S. Perrier and Y. Zhao, *Polym. Chem.*, 2010, **1**, 1615–1623.

80 V. Poonthiyil, T. K. Lindhorst, V. B. Golovko and A. J. Fairbanks, *Beilstein J. Org. Chem.*, 2017, **14**, 11–24.

81 J. Amici, M. U. Kahveci, P. Allia, P. Tiberto, Y. Yagci and M. Sangermano, *J. Mater. Sci.*, 2012, **47**, 412–419.

82 W. Yuan, F. Wang, Z. Chen, C. Gao, P. Liu, Y. Ding, S. Zhang and M. Yang, *Polym. (United Kingdom)*, 2018, **151**, 242–249.

83 W. Wei, Y. Zhao, B. Zhang, Y. Cui, X. Li, X. Fei and X. Liu, *J. Appl. Polym. Sci.*, , DOI:10.1002/app.48986.

84 I. M. Rio-Echevarria, F. Selvestrel, D. Segat, G. Guarino, R. Tavano, V. Causin, E. Reddi, E. Papini and F. Mancin, *J. Mater. Chem.*, 2010, **20**, 2780–2787.

85 F. Branda, B. Silvestri, G. Luciani, A. Costantini and F. Tescione, *Colloids Surfaces A Physicochem. Eng. Asp.*, 2010, **367**, 12–16.

86 A. Akbari, R. Yegani and B. Pourabbas, *Colloids Surfaces A Physicochem. Eng. Asp.*, 2015, **484**, 206–215.

87 Q. Zhang, Z. Ye, S. T. Wang and J. Yin, *Chinese Chem. Lett.*, 2014, **25**, 257–260.

88 S. Alexander, *J Phys*, 1977, **38**, 983–987.

89 M. Daoud and J. P. Cotton, *J. Phys. Paris*, 1982, **43**, 531–538.

90 K. Ohno, T. Morinaga, S. Takeno, Y. Tsujii and T. Fukuda, *Macromolecules*, 2007, **40**, 9143–9150.

91 D. Dukes, Y. Li, S. Lewis, B. Benicewicz, L. Schadler and S. K. Kumar, *Macromolecules*, 2010, **43**, 1564–1570.

92 W. J. Brittain and S. Minko, *J. Polym. Sci. Part A Polym. Chem.*, 2007, **45**, 3505–3512.

93 G. Sharma and M. Ballauff, *Macromol. Rapid Commun.*, 2004, **25**, 547–552.

94 Y. Mei, G. Sharma, Y. Lu, M. Ballauff, M. Drechsler, T. Irrgang and R. Kempe, *Langmuir*, 2005, **21**, 12229–12234.

95 Y. Lu, Y. Mei, M. Ballauff and M. Drechsler, *J. Phys. Chem. B*, 2006, **110**, 3930–3937.

96 Y. Lu, S. Proch, M. Schrinner, M. Drechsler, R. Kempe and M. Ballauff, *J. Mater. Chem.*, 2009, **19**, 3955–3961.

97 X. Chen, L. Zhang, B. Xu, T. Chen, L. Hu, W. Yao, M. Zhou and H. Xu, *Nanoscale Adv.*, 2021, **3**, 2879–2886.

98 A. Kirillova, C. Schliebe, G. Stoychev, A. Jakob, H. Lang and A. Synytska, *ACS Appl. Mater. Interfaces*, 2015, **7**, 21224–21225.

99 B. Fortuni, T. Inose, M. Ricci, Y. Fujita, I. Van Zundert, A. Masuhara, E. Fron, H. Mizuno, L. Latterini, S. Rocha and H. Uji-i, *Sci. Rep.*, 2019, **9**, 1–13.

100 L. Zhang, H. P. Bei, Y. Piao, Y. Wang, M. Yang and X. Zhao, *ChemPhysChem*, 2018, **19**, 1956–1964.

101 B. Tian, S. Liu, S. Wu, W. Lu, D. Wang, L. Jin, B. Hu, K. Li, Z. Wang and Z. Quan, *Colloids Surfaces B Biointerfaces*, 2017, **154**, 287–296.

102 S. Dutta, S. Parida, C. Maiti, R. Banerjee, M. Mandal and D. Dhara, *J. Colloid Interface Sci.*, 2016, **467**, 70–80.

103 G. M. Whitesides and B. Grzybowski, *Science (80-.).*, 2002, **295**, 2418–2421.

104 A. S. Iyer and K. Paul, *IET Nanobiotechnology*, 2015, **9**, 122–135.

105 L. von Bertalanffy, *General System Theory*, George Braziller, New York, 1968.

106 H. R. Maturana and F. J. Varela, *Autopoiesis and cognition: the realization of the living*, D. Reidel Publishing Company, Boston, 1980.

107 H. Fraenkel-Conrat and R. C. Williams, *Proc. Natl. Acad. Sci.*, 1955, **41**, 690–698.

108 I. Prigogine and R. Lefever, in *Synergetics*, Vieweg+Teubner Verlag, Wiesbaden, 1973, pp. 124–135.

109 R. Thiruvengadathan, V. Korampally, A. Ghosh, N. Chanda, K. Gangopadhyay and S. Gangopadhyay, *Reports Prog. Phys.*, , DOI:10.1088/0034-4885/76/6/066501.

110 K. Deng, Z. Luo, L. Tan and Z. Quan, *Chem. Soc. Rev.*, 2020, **49**, 6002–6038.

111 M. Grzelczak, J. Vermant, E. M. Furst and L. M. Liz-Marzán, *ACS Nano*, 2010, **4**, 3591–3605.

112 S. C. Glotzer and M. J. Solomon, *Nat. Mater.*, 2007, **6**, 557–562.

113 T. K. Sau and C. J. Murphy, *Langmuir*, 2005, **21**, 2923–2929.

114 K. Thorkelsson, P. Bai and T. Xu, *Nano Today*, 2015, **10**, 48–66.

115 D. Baranov, A. Fiore, M. Van Huis, C. Giannini, A. Falqui, U. Lafont, H. Zandbergen, M. Zanella, R. Cingolani and L. Manna, *Nano Lett.*, 2010, **10**, 743–749.

116 A. M. Kalsin, M. Fialkowski, M. Paszewski, S. K. Smoukov, K. J. M. Bishop and B. A. Grzybowski, *Science (80-.).*, 2006, **312**, 420–424.

117 S. U. Pickering, *J. Chem. Soc., Trans.*, 1907, **91**, 2001–2021.

118 D. Gonzalez Ortiz, C. Pochat-Bohatier, J. Cambedouzou, M. Bechelany and P. Miele, *Engineering*, 2020, **6**, 468–482.

119 C. Kaewsaneha, P. Tangboriboonrat, D. Polpanich, M. Eissa and A. Elaissari, *Colloids Surfaces A Physicochem. Eng. Asp.*, 2013, **439**, 35–42.

120 G. Singh, H. Chan, A. Baskin, E. Gelman, N. Repnin, P. Král and R. Klajn, *Science (80-.).*, 2014, **345**, 1149–1153.

121 Q. Yu, N. Sun, D. Hu, Y. Wang, X. Chang, N. Yan, Y. Zhu and Y. Li, *Polym. Chem.*, 2021, **12**, 4184–4192.

122 M. Grzelczak, L. M. Liz-Marzán and R. Klajn, *Chem. Soc. Rev.*, 2019, **48**, 1342–1361.

123 Y. T. Chan, S. Li, C. N. Moorefield, P. Wang, C. D. Shreiner and G. R. Newkome, *Chem. - A Eur. J.*, 2010, **16**, 4164–4168.

124 D. Liu, C. Ma, H. Chi, S. Li, P. Zhang and P. Dai, *RSC Adv.*, 2020, **10**, 42584–42595.

125 C. Tang, G. Long, X. Hu, K. W. Wong, W. M. Lau, M. Fan, J. Mei, T. Xu, B. Wang and D. Hui, *Nanoscale*, 2014, **6**, 7877–7888.

126 P. Arumugam, H. Xu, S. Srivastava and V. M. Rotello, *Polym. Int.*, 2007, **56**, 461–466.

127 M. A. Modestino, E. R. Chan, A. Hexemer, J. J. Urban and R. A. Segalman, *Macromolecules*, 2011, **44**, 7364–7371.

128 C. L. Zhang, K. P. Lv, H. P. Cong and S. H. Yu, *Small*, 2012, **8**, 648–653.

129 S. Mann, *Nat. Mater.*, 2009, **8**, 781–792.

130 M. Adams, Z. Dogic, S. L. Keller and S. Fraden, *Nature*, 1998, **393**, 349–352.

131 Y. Zhao, K. Thorkelsson, A. J. Mastroianni, T. Schilling, J. M. Luther, B. J. Rancatore, K. Matsunaga, H. Jinnai, Y. Wu, D. Poulsen, J. M. J. Fréchet, A. Paul Alivisatos and T. Xu, *Nat. Mater.*, 2009, **8**, 979–985.

132 R. Zhang, B. Lee, M. R. Bockstaller, A. M. Al-Enizi, A. Elzatahry, B. C. Berry and A. Karim, *Faraday Discuss.*, 2016, **186**, 31–43.

133 N. Bachhar, G. Kumaraswamy and S. K. Kumar, *Macromolecules*, 2019, **52**, 4888–4894.

134 M. Bonnevide, A. M. Jimenez, D. Dhara, T. N. T. Phan, N. Malicki, Z. M. Abbas, B. Benicewicz, S. K. Kumar, M. Couty, D. Gigmes and J. Jestin, *Macromolecules*, 2019, **52**, 7638–7645.

135 D. Sunday, J. Ilavsky and D. L. Green, *Macromolecules*, 2012, **45**, 4007–4011.

136 C. Chevigny, F. Dalmas, E. Di Cola, D. Gigmes, D. Bertin, F. Boué and J. Jestin, *Macromolecules*, 2011, **44**, 122–133.

137 P. G. Ferreira, A. Ajdari and L. Leibler, *Macromolecules*, 1998, **31**, 3994–4003.

138 C. Koh, G. S. Grest and S. K. Kumar, *ACS Nano*, 2020, **14**, 13491–13499.

139 J. F. Moll, P. Akcora, A. Rungta, S. Gong, R. H. Colby, B. C. Benicewicz and S. K. Kumar, *Macromolecules*, 2011, **44**, 7473–7477.

Chapter 2.
Synthesis and characterization of SiO_2 HNPs

2.1. Overview

Chapter 2 reports the development of a multi-gram colloidal synthesis of maleated polybutadiene (PB) functionalized SiO_2-HNPs having tunable size, controlled morphology and tailored surface chemistry. Their characterization is also reported.[1]

Our synthetic strategy consists of a multistep preparation. Firstly, shape- and size- controlled SiO_2 NPs were obtained by a modified Stöber synthesis.[2] Commercial silica is typically highly and irreversibly aggregated due to the formation of hydrogen bonds between surface silanols.[3,4] This prevents the synthesis of functionalized core-shell SiO_2 HNPs. On the other hand, the use of SiO_2 NPs prepared by a colloidal, wet-chemistry approach results in well-dispersed and uniformly coated HNPs.[5] For this reason, the synthesis conditions for the SiO_2 NPs cores were fine-tuned to achieve the required size, dispersion state and surface chemistry.

PB chains functionalized with succinic anhydride groups were grafted onto the surface of SiO_2 NPs by following a two-step "grafting to" approach. First, the NPs were functionalized with APTES. Then, PB was anchored by exploiting the reaction between the APTES amino-group and the succinic anhydride functionalities. By this approach, different degrees of surface coverage were obtained. It is worth noting that the majority of HNPs syntheses in the literature focus on polymers with high glass transition temperatures (T_g), such as PS, while HNPs functionalized with rubbery polymers having low glass transition temperature, such as PB[5,6] or PI, has not been widely investigated.

The synthesis was also modulated for producing HNPs having a different polymeric shell with lower T_g (PS and polypropylene, PP) to test the versatility of the method.

The surface chemistry of bare SiO_2 NPs was thoroughly characterized by FT-IR spectroscopy, thermogravimetric analysis (TGA) and CHNS elemental analysis, which allowed the accurate quantification of residual surface ethoxy groups and silanol groups available for functionalization. The morphology of the obtained SiO_2 NPs was characterized by dynamic light scattering (DLS) measurements, transmission electron microscopy (TEM) and scanning electron microscopy (SEM).

APTES-functionalized NPs and PB-coated SiO_2 HNPs were characterized by TGA, FT-IR and solid-state ^{13}C- and ^{29}Si-NMR to study their surface chemistry. Their morphology and self-assembly behavior were studied, both in matrix-free conditions and in cis-PB matrices, by SEM, TEM, Brunauer-Emmett-Teller (BET) specific surface area analysis and Small Angle X-Ray Scattering (SAXS) analysis.

The overall outcomes indicate the efficacy of the methodological approach adopted in providing tailored SiO_2 HNPs which can be considered a promising filler system for preparing functional NCs characterized by a network of NPs self-assembled structures.

2.2. Sample preparation

2.2.1. Materials

Tetraethyl orthosilicate (TEOS, ≥ 99%), 25% aqueous ammonia solution, 37% aqueous hydrochloric acid and 3-aminopropyltriethoxysilane (APTES, ≥ 98%) were purchased from Sigma-Aldrich. Ethanol (≥99.8%) was purchased from Honeywell. Toluene (99%) was purchased from Alfa-Aesar. Liquid maleated polybutadiene (Polyvest MA75, MW ~3000 g/mol, PB, full characterization reported in Paragraph 2.3.2.3) was purchased from Evonik. Poly(styrene-co-maleic anhydride), cumene terminated (MW

≈ 1900, PS), polypropylene-graft-maleic anhydride (MW ≈ 9100, PP), cis–1,4–polybutadiene (average MW ≈ 200,000 – 300,000, cis-PB) and tetrahydrofuran (anhydrous, ≥99.9%, with 250 ppm BHT as inhibitor) (THF) were purchased from Sigma-Aldrich and used without further purification.

2.2.2. Colloidal synthesis of SiO_2 NPs

The Stöber synthesis of silica NPs was performed following a modified method reported by Wu *et al.*[5] 62.5 mL of an aqueous solution of ammonium hydroxide (25 wt% in H_2O) and 1250 mL of EtOH were added to a 2000 mL two-necked flask equipped with a reflux condenser. The mixture was stirred at 300 rounds per minute (rpm) and heated at 60 °C. Two additional reaction temperatures were tested: 25 °C and 40 °C.

A mixture of 31.2 mL of TEOS and 35.0 mL of ethanol was then transferred to a dropping funnel and added dropwise in ~ 60 min. The molar ratio of ammonia, water and TEOS in the final mixture was NH_3 : H_2O : TEOS = 6 : 17 : 1. The mixture was then left to react under magnetic stirring for 20 h. After the reaction was completed, 25 mL of 2 M HCl aqueous solution were added to the flask to induce the precipitation of the NPs.

The obtained NPs were then isolated by centrifugation at 9000 rpm and washed four times with 240 mL of ethanol. Then, SiO_2 NPs (with a reaction yield of 68 %) were dispersed in 125 mL of ethanol (step a in Figure 2.1) by ultrasonication and the resulting colloidal SiO_2 NPs dispersion was utilized for the next functionalization step (see Paragraph 2.2.3). SiO_2 NPs were labeled SiO_2-ST. Dry SiO_2-ST for physico-chemical characterization were obtained by drying at 85 °C overnight.

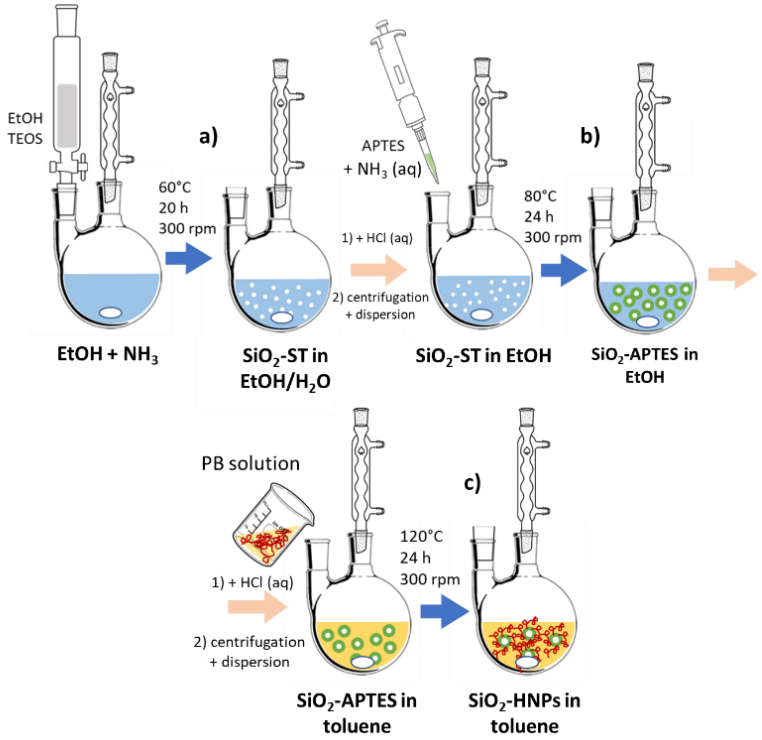

Figure 2.1 Scheme for the three-step synthesis of SiO_2-HNPs. Adapted from Tripaldi *et al*.[1]

2.2.3. Functionalization with APTES

The suspension of SiO_2 NPs in ethanol was heated at reflux under stirring at 300 rpm. Then, 50 µL of 25 wt% of ammonia solution and 0.799 mL of APTES were added and the mixture was stirred at 80 °C for 24 h. 5 mL of 2 M HCl aqueous solution were added to favor the NPs separation. After separation by centrifugation at 9000 rpm, NPs were washed three times with 240 mL of toluene.

The APTES-functionalized SiO_2 NPs (step b in Figure 2.1) were re-dispersed in 120 mL of toluene by ultrasonication and were utilized for the next polymer grafting step. SiO_2-ST NPs functionalized with APTES were labeled SiO_2-APTES. Dry SiO_2-APTES was obtained by drying functionalized SiO_2 NPs in vacuo at 85 °C overnight.

2.2.4. Synthesis of SiO_2 HNPs

Three different amounts of PB (reported in Table 2.1) were dissolved in 5 mL of toluene. SiO_2-APTES dispersion in toluene and the PB mixture were refluxed under stirring at 300 rpm for 24 h (step c in Figure 2.1). The particles were then recovered by centrifugation at 9000 rpm and washed three times with 240 mL of toluene.

SiO_2 HNPs were obtained after drying at 85 °C under vacuum overnight and labeled SiO_2-HNP_X, where X = PB wt% (determined by TGA and CHNS, see Paragraph 2.3.2.3). To test the versatility of the synthetic method, the procedure was repeated also with PS (SiO_2-PS_HNP) and PP (SiO_2-PP_HNP) polymers (amounts reported in Table 2.1).

Table 2.1 Amounts of PB added for the synthesis of SiO_2 HNPs.

Sample	Grafted polymer	Polymer amount (g)
SiO_2-HNP_3	PB	0.4680
SiO_2-HNP_4	PB	0.9360
SiO_2-HNP_6	PB	1.8720
SiO_2-PS_HNP_PS	PS	1.8720
SiO_2-PP_HNP	PP	1.8720

2.2.5. Preparation of cis-PB NCs

SiO_2-ST, SiO_2-APTES and SiO_2-HNP_3 were used to prepare cis-PB/SiO_2-Y NCs (Y = ST, APTES, HNP_X) according to the following procedure.

0.2 g of cis-PB were finely cut and transferred to a round bottom flask. X NPs (5 wt % of SiO_2 in cis-PB, accounting for functionalization) were dispersed in 100 mL of THF by ultrasonication for 15 min. The NPs dispersion was added to the flask and the mixture was stirred at room temperature until the polymer was fully dissolved (2-3 h). THF was selected as the solvent for the preparation of the NCs because it provides good solubility of the polymer matrix and excellent dispersion of both bare and functionalized SiO_2 NPs. Overall, the morphology of HNPs aggregates is not impacted by the solvent choice.[7] Finally, the mixture was deposited over TEM grids and SEM stubs, and the solvent was evaporated at room temperature overnight, giving rise to cis-PB/SiO_2-Y NCs.

2.3. Results and discussion

In this paragraph, the morphological and physico-chemical characterization of bare SiO_2-ST and functionalized SiO_2-HNP_X, SiO_2-PS_HNP and SiO_2-PP_HNP is discussed. Experimental details of all characterization techniques are reported in Appendix A.

2.3.1. SiO_2-ST NPs

The synthesis of SiO_2-ST NPs was performed at three different temperatures: 25, 40, and 60 °C, to test the optimal conditions for the synthesis of NPs with desired size and shape. The morphology of SiO_2-ST was investigated by DLS, as shown in Figure 2.2, and by SEM, reported in Figure 2.3. NPs diameters obtained by both techniques are reported in Table 2.2.

Morphological analysis confirms that the size of silica NPs, at constant reactant concentrations and pH, decreases monotonically when the temperature of the synthesis is increased, as expected based on the literature.[8,9] In particular, SEM images show that, as the synthesis temperature is increased from 25 to 40 and 60 °C, the average particle diameter decreases from 65 ± 6 nm to 51 ± 6 nm and 32 ± 3 nm respectively. Diameters obtained from DLS analysis were derived from the average number distributions and are comparable to SEM diameters.

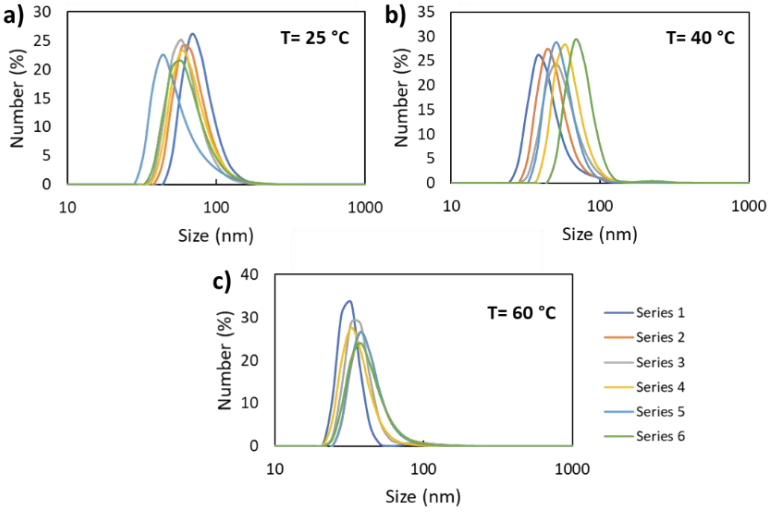

Figure 2.2 Number distribution curves from DLS analysis of SiO_2-ST synthesized at a) 25 °C, b) 40 °C and c) 60 °C. Six measurements were performed for each sample. Adapted from Tripaldi *et al.*[1]

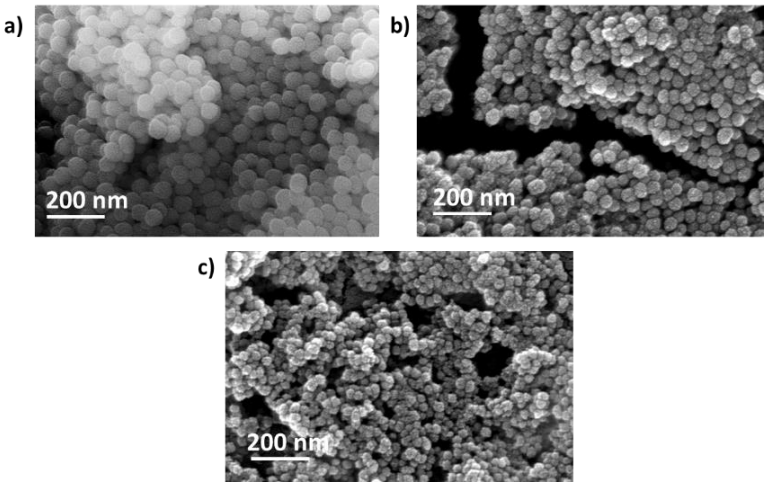

Figure 2.3 SEM images of SiO_2-ST synthesized at a) 25 °C, b) 40 °C and c) 60 °C. Adapted from Tripaldi *et al.*[1]

Table 2.2 SiO_2-ST diameters from SEM and DLS analysis.

Reaction temperature (°C)	**DLS hydrodynamic diameter* (nm)**	**SEM diameter (nm)**
25	62 ± 5	65 ± 6
40	52 ± 3	51 ± 6
60	36 ± 3	32 ± 3

*reported diameter is the number average of six subsequent measurements, the uncertainty is the standard deviation.

DLS results suggest that NPs are well dispersed in ethanol and do not form aggregates, which is essential to achieve core-shell

functionalization. The diameter of silica NPs reported in the literature for self-assembly in PNCs ranges between 7 nm and 27 nm.[10] Following this requirement, the final synthesis was conducted at 60 °C in order to optimize the morphology of the NPs in the following steps.

The surface chemistry of SiO_2-ST was studied by TGA and CHNS analyses, reported in Figure 2.4. TGA analysis (a in Figure 2.4) reveals a significant weight loss between 150 and 1000 °C, associated with the degradation of both surface silanols and non-hydrolyzed ethoxy groups. CHNS analysis (b in Figure 2.4) confirms the presence of carbon deriving from residual ethoxy- groups on the surface of SiO_2-ST. [11–14]

a)

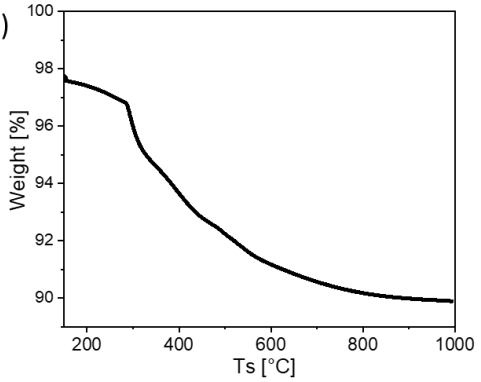

b)

Elemental analysis (% wt)			
% C	% H	% N	% S
3.50	1.38	0.21	0.22

Figure 2.4 a) TGA analysis and b) CHNS elemental analysis of SiO_2-ST. Adapted from Tripaldi *et al.*[1]

The amount of surface ethoxy groups was estimated from CHNS elemental analysis based on Equation 2.1.

$$EtO\ wt\% = \frac{\%\ C}{2 \cdot 12.0\ \ g/mol}\ 45.1\ g/mol \qquad (2.1)$$

From this equation, the resulting total weight percentage of ethoxy groups in SiO_2-ST is 6.56 wt%.

Assuming that the ethoxy groups embedded within the particle core are negligible with respect to the amount on the surface, the concentration of surface silanols groups can be estimated by subtracting the weight percentage of residual ethoxy groups from the total TGA weight loss, as shown in Equation 2.2:

$$mol\ OH/_{g\ SiO_2} = \frac{(\Delta wt\ \%_{150-1000°C}^{TGA} - EtO\ wt\%) \cdot 2}{MW\ H_2O} \qquad (2.2)$$

where $\Delta wt\ \%_{150-1000°C}^{TGA}$ is the weight loss percentage between 150 and 1000 °C determined by TGA, EtO wt% is the weight percentage of surface ethoxy groups determined by CHNS analysis and MW H_2O is the M_w of water.

For SiO_2-ST, this calculation yields 2.39×10^{-3} mol OH/g SiO_2. By comparison, the estimated quantity of ethoxy groups is 1.45×10^{-3} mol/g, indicating that there is a large amount of free silanol groups to be exploited in the subsequent functionalization step.

Figure 2.5 reports the SiO_2-ST FT-IR spectrum, where characteristic peaks of SiO_2 can be identified. The spectrum shows an intense absorption peak at 1060-1050 cm^{-1}, assigned to Si-O-Si asymmetric stretching, while the absorption peaks at 950 cm^{-1} and 790 cm^{-1} are associated to Si-OH and Si-O stretching vibrations respectively. FT-IR analysis also confirms the presence of surface ethoxy groups.

Signals associated with aliphatic C-H stretching can be identified in the region between 3000 and 2950 cm^{-1}.

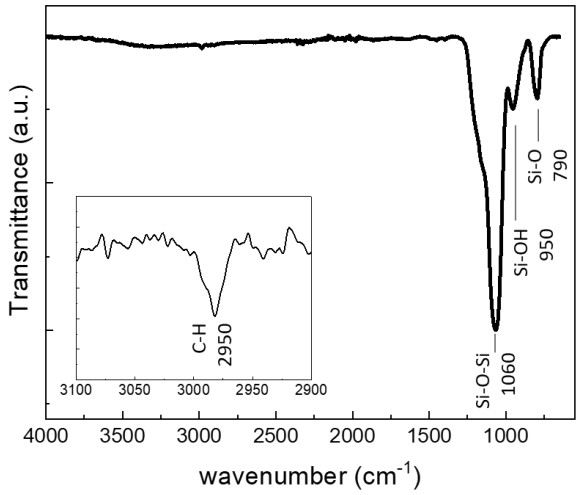

Figure 2.5 FT-IR spectrum of SiO_2-ST. Adapted from Tripaldi *et al.*[1]

2.3.2. SiO_2 HNPs

SiO_2-ST synthesized at 60 °C was selected to prepare HNPs, having the optimal size in line with commercial silica utilized in rubber NCs. Therefore, it was first modified with APTES, while the subsequent PB grafting was realized by exploiting the reaction between succinic anhydride groups on PB chains with the APTES amino group. While succinic anhydride groups can also react directly with the silica surface silanols, and this reaction has been previously used to graft polymer chains onto the silica surface,[6] succinic anhydride reacts preferentially with the nucleophilic primary amine of APTES by forming an amide bond.[15] Another crucial function of the first silanization step is to favor the homogenous dispersion of the highly

hydrophilic SiO_2-ST in toluene. The full reaction scheme is reported in Figure 2.6.

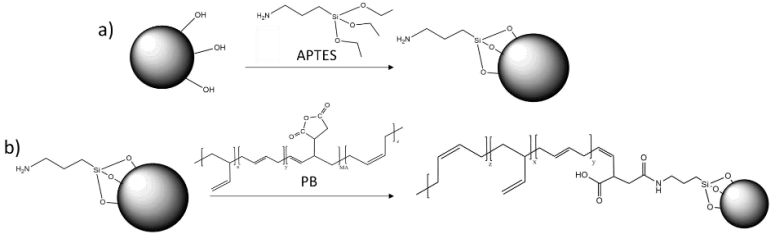

Figure 2.6 Reaction scheme for the two-step: a) SiO_2-ST functionalization with APTES and b) grafting of PB chains. Adapted from Tripaldi *et al.*[1]

2.3.2.1. Morphological characterization of SiO_2 HNPs

The morphology of SiO_2 HNPs was investigated by SEM and TEM analyses. Figure 2.7 shows preliminary investigation of SiO_2-Y NPs by SEM. SiO_2-ST and SiO_2-APTES are both well dispersed and uniform in size and shape. SiO_2-APTES NPs are slightly less aggregated, possibly due to electrostatic repulsion after silanization, while SiO_2-HNP_3 shows very high aggregation, confirming the presence of polymeric shell which completely neutralize the surface charge due to Van der Waals attraction between the PB chains on the HNPs surface.

More accurate indication of NPs diameter and assembly behavior were obtained by TEM analysis (Figure). Particle diameter of SiO_2-ST was estimated to be about 24±5 nm, while SiO_2-APTES particles and SiO_2-HNP_X have a diameter of 25±4 nm and 27±5 nm, respectively for X = 3, 4 and 6. The slightly larger diameter (of about 2 nm) of SiO_2-HNP_X is due to the presence of PB chains grafted around the NP cores. In SiO_2-HNP_X, particularly in SiO_2-HNP_3, the PB layer around the NPs can be clearly identified, and polymer filaments are

also present between the NPs, indicating that their interaction is mediated by the polymer. TEM micrographs of SiO_2-PS_HNP and SiO_2-PP_HNP are reported in Figure 2.8.

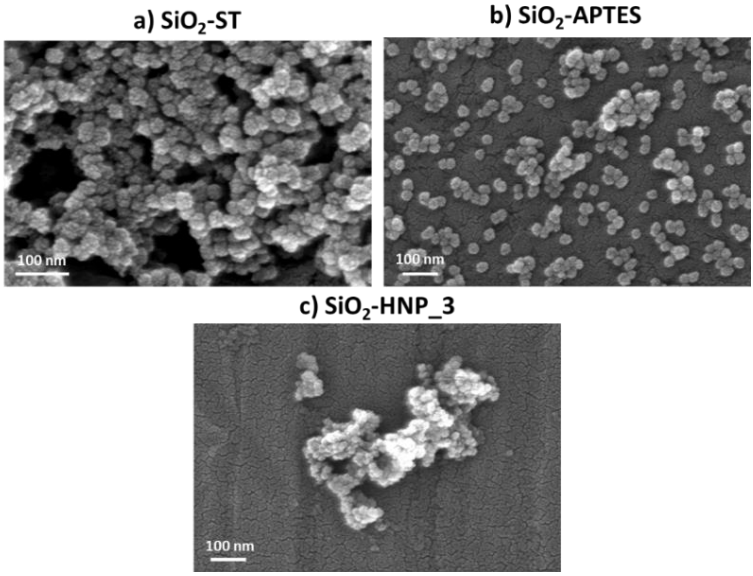

Figure 2.7 SEM images of a) SiO_2-ST, b) SiO_2-APTES and c) SiO_2-HNP_3, as rapresentative of SiO_2-HNP_X NPs. Adapted from Tripaldi *et al.*[1]

Similarly to HNPs grafted with PB, they clearly show a polymer layer surrounding the SiO_2 cores. Interestingly, TEM micrographs also show differences in packing of the NPs as surface functionalization is modified. While SiO_2-ST and SiO_2-APTES tend to show the typical close-packing behavior of spherical NPs, in SiO_2-HNP_3 the NPs tend to self-organize in string-like anisotropic structures. Similar strings are observed in SiO_2-HNP_4, while in SiO_2-HNP_6 NPs tend to form small clusters.

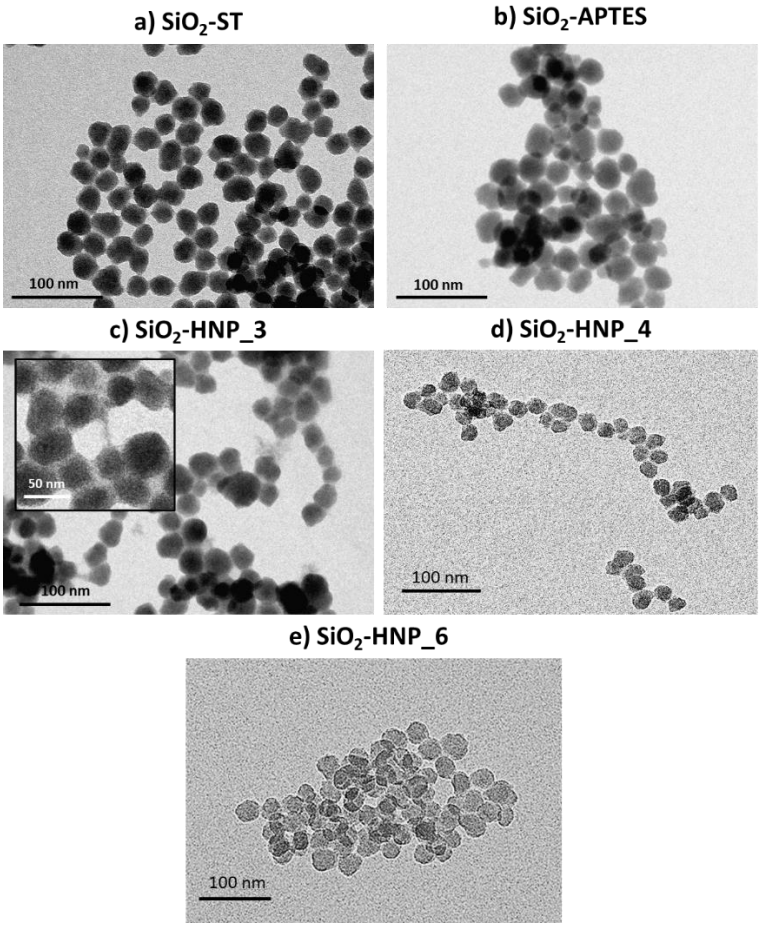

Figure 2.8 TEM micrographs of a) SiO_2-ST, b) SiO_2-APTES, c) SiO_2-HNP_3, d) SiO_2-HNP_4 and e) SiO_2-HNP_6. Adapted from Tripaldi *et al.*[1]

This spontaneous self-assembly behavior of sparsely grafted HNPs, as previously explained, is due to a balance between attractive and repulsive interactions, particularly short-range core-core attractive

interactions and long-range brush-brush repulsive interactions. This self-assembly behavior, originally observed in homopolymer matrices,[10,16] varies depending on polymer grafting density and has been predicted to take place also in solvent-free and matrix-free conditions.[17–19]

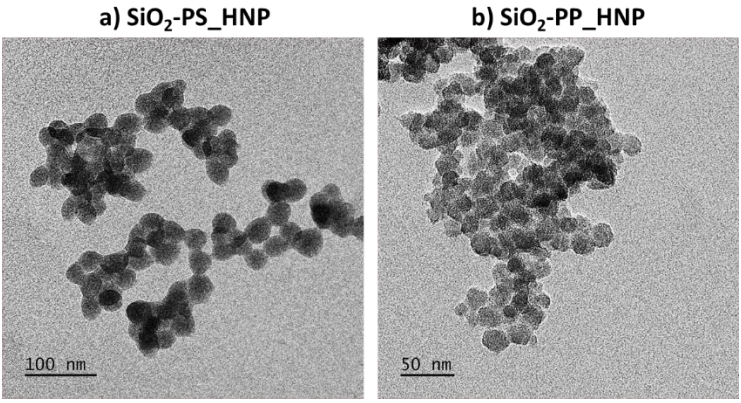

Figure 2.8 TEM micrographs of a) SiO_2-PS_HNP and b) SiO_2-PP_HNP.

2.3.2.2. N_2 physisorption and BET SSA analyses

SiO_2-Y NPs were also characterized by BET analysis. Adsorption/desorption isotherms obtained from N_2 physisorption are reported in Figure 2.9. Values of specific surface area (SSA) and cumulative pore volume V_{pore} obtained from BET analysis of the samples are reported in Table 2.3.

All samples show isotherms of type IV, with hysteresis loops of type H2(b). Such isotherms are typical of materials with irregular and polydisperse mesopores, as indicated in the IUPAC classification.[20] However, SiO_2 NPs obtained with the Stöber method are typically either microporous or nonporous.

Furthermore, adsorption/desorption isotherms show that as bare SiO_2 is functionalized first with APTES and then with PB, the hysteresis loop becomes narrower and shifts to higher values of p/p_0. Typically, when mesoporous materials are functionalized with organic molecules and polymers the hysteresis loop becomes wider and is shifted to lower values of p/p0. This was demonstrated, for example, by Torabinejad and co-workers,[21] who functionalized MCM-41 mesoporous silica with polymer chains.

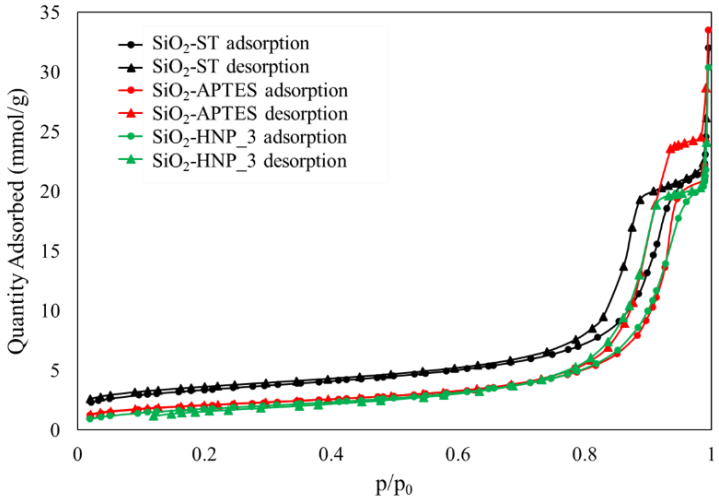

Figure 2.9 Adsorption/desorption isotherms of SiO_2-ST, SiO_2-APTES and SiO_2-HNP_3 obtained from BET N_2 physisorption. Adapted from Tripaldi *et al.*[1]

From these considerations, it follows that the hysteresis loops observed in the N_2 adsorption/desorption isotherms are not related to the presence of mesopores. Conversely, the presence of type IV isotherms is due to gas condensation in interparticle spaces, a phenomenon which has been observed previously in Stöber silica

NPs.[20,22,23] Interestingly, the differences in isotherm shapes in bare NPs, APTES-functionalized NPs and HNPs may point to a different packing of NPs, as was already observed in TEM micrographs.

Table 2.3 Values of SSA and cumulative pore volume obtained from BET analysis of SiO_2-ST, SiO_2-APTES and SiO_2-HNP_3.

Sample	**SSA (m^2/g)**	**V_{pore} (cm^3/g)**
SiO_2-ST	272.7 ± 0.6	0.834
SiO_2-APTES	166.4 ± 0.4	0.932
SiO_2-HNP_3	148.9 ± 0.6	0.733

As shown in Table 2.3, values of SSA decrease as the SiO_2 NPs are functionalized. This is due both to the obstruction of pores as the surface of NPs is coated with organic molecules, and to the increase in NPs sizes due to functionalization.

2.3.2.3. Determination of SiO_2 HNPs grafting density

The evaluation of SiO_2-ST SSA by BET analysis allowed the calculation of the surface density of silanol groups. In detail, knowing the amount of Si-OH expressed as mol/g (see Paragraph 2.3.1), the surface density of silanols, expressed as OH/nm^2, can be calculated with Equation 2.3:

$$\sigma_{OH}[OH/nm^2] = \frac{nOH\ [mol/g] \cdot N_A[OH/mol]}{SSA\ [m^2/g]10^{18}[nm^2/m^2]} \qquad (2.3)$$

The surface density of silanols on SiO_2-ST, considering the uncertainty due to possible solvent residues and incomplete condensation, was estimated to be in the order of 50 OH/nm^2. This

value can be compared to SiO_2 NPs typically used for the study of self-assembly, such as those provided by Nissan Chemicals.[7,16,24,25] These NPs were characterized in the literature by Madathingal *et al.*,[26] who estimated the Si-OH surface density of Nissan SiO_2 NPs in isopropanol with various primary particle sizes and reported values in the range of 1.7 – 7.8 SiOH/nm^2. This value is much lower than the value determined for SiO_2-ST.

Similarly, Barabanova *et al.*[27] determined the surface silanol density for Nissan SiO_2 NPs (d ≈ 10-15 nm) in methyl ethyl ketone by volumetric and titration methods. They concluded that the silanol surface density ranges between 0.210 and 0.500 mmol OH/g SiO_2, significantly below the value of 2.39 mmol OH/g SiO_2 calculated for our colloidal SiO_2-ST (see Paragraph 2.3.1). Overall, this comparison confirms that synthesizing colloidal NPs by the Stöber method can strongly increase the available sites for functionalization compared to commercial silica.

Grafting densities of APTES and PB were determined by TGA analysis. TGA curves of the PB-functionalized samples, reported in Figure 2.10, clearly show increasing weight loss between 150 and 1000 °C, indicating an increasing degree of surface functionalization.

TGA curves of the PS and PP functionalized samples are reported in Figure 2.11, showing the effective functionalization of the SiO_2 NPs with the polymer chains. The higher grafting density obtained for PP may be attributed to a higher degree of functionalization of the polymer chains with succinic anhydride groups. The weight loss between 30 and 150 °C (not reported) is attributed to the loss of adsorbed solvents and water and is not accounted for in the estimation of polymer grafting density.

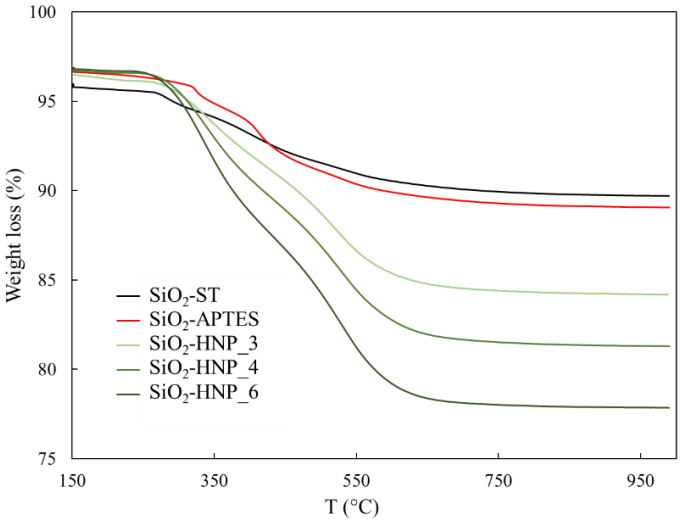

Figure 2.10 TGA curves of SiO_2-ST, SiO_2-APTES and SiO_2-HNP_X samples.[1]

To determine the grafting density, the weight loss obtained from TGA needs to be divided into different contributions, as shown in Equation 2.4:

$$\Delta wt\%_{150-1000°C}^{TGA} = wt\%_{OH+OEt} + wt\%_{APTES} - \\ - \frac{wt\%_{APTES}}{MW_{APTES}} \left(3 \times \frac{MW_{H2O}}{2}\right) + wt\%_P \qquad (2.4)$$

where:

- $\Delta wt\%_{150-1000}$ is the TGA weight loss between 150-1000 °C;
- $wt\%_{OH+OEt}$ is the weight percentage of silanol and ethoxy groups obtained from the TGA weight loss of bare SiO_2-ST;

- $wt\%_{APTES}$ is the weight percentage of APTES;
- MW_{APTES} is the M_w of APTES after functionalization;
- MW_{H2O} is the M_w of water;

$wt\%_P$ is the weight percentage of polymer (PB, PS or PP).

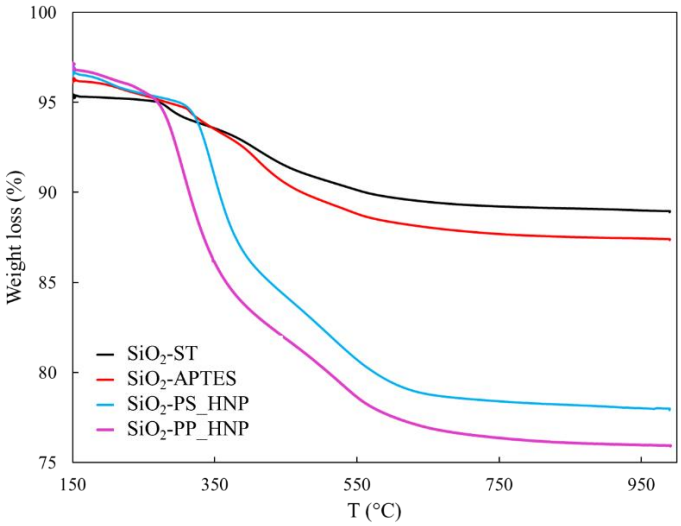

Figure 2.11 TGA curves of SiO_2-ST, SiO_2-APTES, SiO_2-PS_HNP and SiO_2-PP_HNP.

This calculation considers the loss of three surface silanols for each APTES molecule, assuming that APTES is anchored onto the SiO_2 surface with all its three ethoxysilane groups.

Following Equation 2.4, first the weight percentage of APTES is determined from the TGA curve of SiO_2-APTES by Equation 2.5.

$$wt\%_{APTES} = \frac{\Delta wt\%_{150-1000°C}^{TGA} - wt\%_{OH+OEt}}{1 - 3MW_{H2O}/2MW_{APTES}} \quad (2.5)$$

Finally, knowing $wt\%_{APTES}$, the weight percentage of polymer (PB, PS or PP) is obtained from the TGA curves of SiO_2-HNP_X (X = 3, 4, 6) and SiO_2-PP_HNP and SiO_2-PS_HNP by following Equation 2.6.

$$wt\%_P = \Delta wt\%_{150-1000°C}^{TGA} - wt\%_{OH+OEt} - wt\%_{APTES} + \\ + \frac{wt\%_{APTES}}{MW_{APTES}}\left(3 \times \frac{MW_{H2O}}{2}\right) \quad (2.6)$$

Once the wt% is determined, the grafting density for HNPs is obtained by considering the SiO_2 NPs SSA (273 m^2/g obtained from BET analysis, see Paragraph 0), as shown in Equation 2.7:

$$\sigma_X[chains/nm^2] = \frac{wt\%_X \cdot MW_X \cdot N_A[chains/mol]}{SSA\ [m^2/g]\ 10^{18}[nm^2/m^2]} \quad (2.7)$$

The resulting values of functionalization percentage and grafting density for all samples are reported in Table 2.4.

The values of grafting densities obtained for PB-grafted HNPs are in a range compatible with self-assembly according to the data reported in the literature.[7,10,16]

Based on these values, the conformation of polymer chains on the surface of SiO_2 HNPs was estimated according to the approach suggested by Brittain and co-workers (Paragraph 1.1.3).[28] The reduced grafting density Σ was calculated by Equation 2.8:

$$\Sigma = \sigma \pi R_g^2 \quad (2.8)$$

where R_g is the radius of gyration of the PB chain. R_g and polydispersivity of maleate PB chain were determined by GPC analysis as reported in Table 2.5.

Table 2.4 Degrees of functionalization for SiO_2-APTES, SiO_2-HNP_X, SiO_2-PS_HNP and SiO_2-PP_HNP an expressed in terms of weight percentage and grafting density.

Sample	Grafted molecule	Polymeric shell (wt%)	σ_X (chains/nm^2)
SiO_2-APTES	APTES	1.58	0.60
SiO_2-HNP_3	PB	2.82	0.02
SiO_2-HNP_4	PB	4.11	0.03
SiO_2-HNP_6	PB	6.26	0.05
SiO_2-PS_HNP	PS	9.47	0.07
SiO_2-PP_HNP	PP	11.4	0.08

Table 2.5 Specifications of maleate terminated PB: a) PB microsctructure; b) specifications from commercial data sheet ; c) results of GPC analysis.

Specifications from GPC	
Polydispersity*	1.561 ± 2%
R_g**	2.072 ± 2%

*Polydispersity index = Mw/Mn of PB

**Estimated from the hydrodynamic radius of PB solution in THF from GPC analysis

According to the model proposed by Brittain *et al.*, the different regimes are defined as follows:

1. $\Sigma < 1$, "mushroom" or weakly interacting regime;
2. $1 < \Sigma < 5$, crossover regime;
3. $\Sigma > 5$, "brush" or strongly interacting regime.

By considering R_g=2.072 for PB in THF, the resulting values of reduced grafting density for SiO_2-HNP_3, SiO_2-HNP_4 and SiO_2-HNP_6 are Σ=0.40, 0.67 and 1.1, respectively. This indicates that the polymer chains are mostly in the "mushroom" regime, as expected due to the low grafting density of HNPs.

2.3.2.4. Spectroscopic analysis of SiO_2 HNPs

HNPs surface chemistry was characterized by FT-IR spectroscopy. Infrared spectra are reported in Figure 2.12. Since all SiO_2-HNP_X samples show similar features, only SiO_2-HNP_3 is reported.

Compared to SiO_2-ST, the spectra of SiO_2-APTES and SiO_2-HNP_3 indicate a partial substitution of surface silanols following functionalization. In detail, the signal at 1068 cm^{-1} associated to the Si-O-Si stretching becomes broader, while the peak at 958 cm^{-1}, corresponding to the Si-O-H stretching of surface silanols, decreases in intensity and becomes a shoulder of the adjacent peak.

The spectrum of SiO_2-APTES also shows the characteristic peaks associated with APTES functionalization. In detail, the peak at 1625 cm^{-1} is associated to the N-H bend of primary amines and the peaks in the range 3000-2900 cm^{-1} are attributed to the asymmetric stretching of CH_2 groups, overlapping with the signals corresponding to the SiO_2-ST surface ethoxy groups.

In the SiO_2-HNP_3 spectrum, signals associated with the presence of PB can be identified. In particular, the presence of the peak at

1699 cm^{-1}, associated with the carbonyl stretching of the amide group, confirms that the reaction between succinic anhydride of PB and APTES amine has taken place, indicating the successful grafting of the polymer chains.

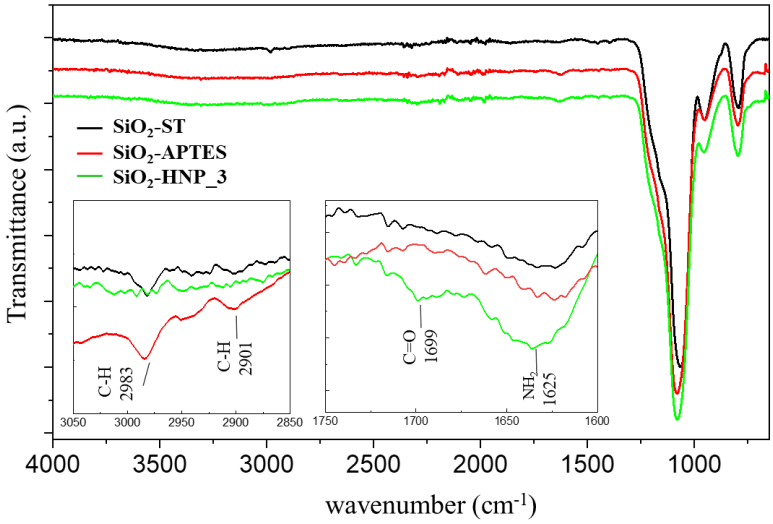

Figure 2.12 FT-IR spectra of SiO_2-ST, SiO_2-APTES and SiO_2-HNP_3. Adapted from Tripaldi *et al.*[1]

SiO_2-ST, SiO_2-APTES and SiO_2-HNP_3 (as representative sample for silica PB-grafted HNPs) were also characterized by solid-state ^{13}C and ^{29}Si NMR analyses to confirm the functionalization of silica. The ^{13}C cross-polarization magic angle spinning (CPMAS) spectra are reported in Figure 2.13. ^{13}C NMR of SiO_2-ST confirms the presence of surface ethoxy groups, demonstrated by two peaks at 59.6 ppm and 16.8 ppm. SiO_2-APTES shows peaks associated with the propyl chain (α, β and γ) as well as signals due to ethoxy groups (δ and ε),

associated with both SiO_2-ST surface ethoxy groups and unhydrolyzed APTES ethoxysilane chains.[29]

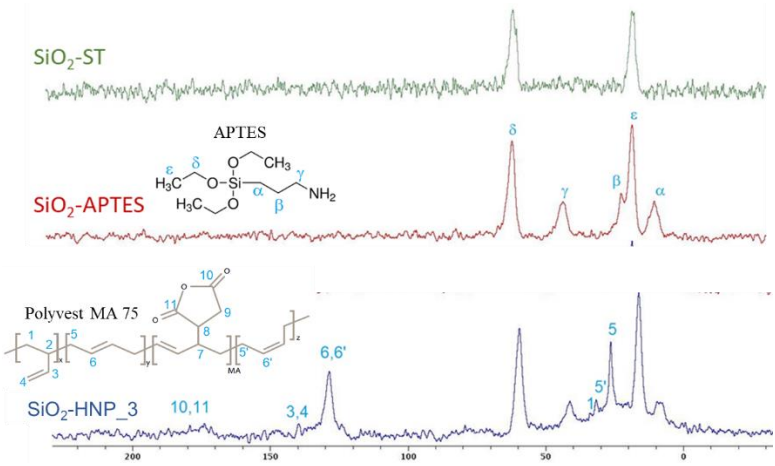

Figure 2.13 ^{13}C CPMAS solid-state NMR spectra of SiO_2-ST, SiO_2-APTES and SiO_2-HNP_3. Adapted from Tripaldi *et al.*[1]

The SiO_2-HNP_3 spectrum clearly shows the main signals attributed to the PB backbone, namely methylene (5, 5') and olefinic (6, 6') carbon atoms of cis and trans PB. The minor presence of 1,2 vinyl groups is also detected (1, 3, 4),[30] while the C=O groups of the succinic anhydride moieties are clearly identified (10, 11). These results are confirmed by comparing the spectrum of SiO_2-HNP_3 to that of pure PB,[31] reported in Figure 2.14. Overall, these spectra show that the functionalization of SiO_2-ST was successful.

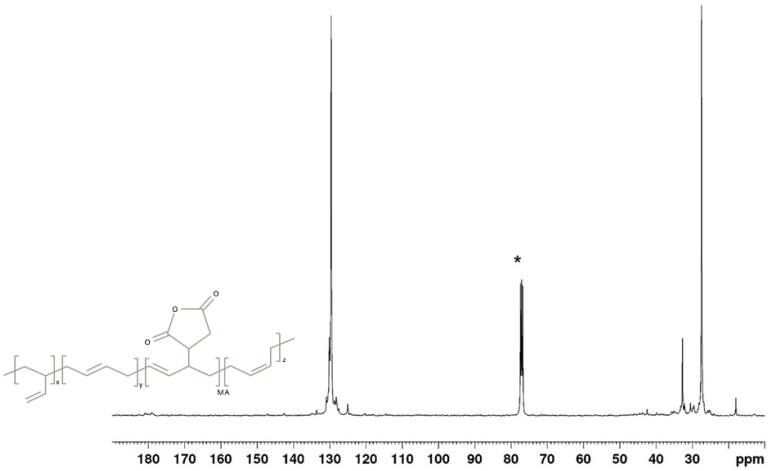

Figure 2.14 ^{13}C spectrum of PB. Solvent peaks are marked with (*). Adapted from Tripaldi *et al*.[1]

^{29}Si CPMAS NMR spectra of SiO_2-ST, SiO_2-APTES and SiO_2-HNP_3 are reported in Figure 2.15. All samples exhibit the typical Q^4, Q^3 and Q^2 signals, respectively associated with siloxanes, single silanols and geminal silanols, at -109.1, -100.5 and -91.6 ppm. In addition, SiO_2-APTES and SiO_2-HNPs also show T^3 and T^2 peaks at -65.1 and -56.5 ppm, respectively. These signals are due to APTES functionalization and to the formation of Si-O-Si-C bonds.

Comparing peak intensities of the SiO_2-ST and SiO_2-APTES spectra reveals that Q^2 units almost disappear and Q^3 decrease significantly upon functionalization with APTES, indicating that surface silanols of bare silica are partially substituted by the aminosilane. On the other hand, the subsequent PB grafting in sample SiO_2-HNPs does not impact the ^{29}Si spectrum, strongly indicating that PB is preferentially

anchored to the APTES amino group rather than directly reacting with surface silanols.

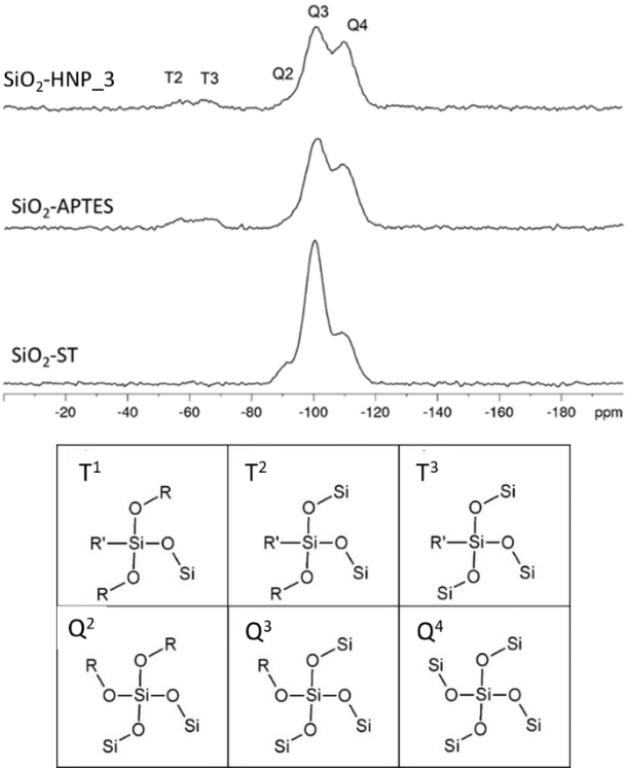

Figure 2.15 a)^{29}Si CPMAS NMR spectra of SiO_2-ST, SiO_2-APTES and SiO_2-HNP_3 and b) different chemical groups (T^1-T^3, Q^2-Q^3) present on the surface of SiO_2, for reference. Adapted from Tripaldi *et al.*[1]

Single pulse magic angle spinning (MAS) ^{29}Si NMR spectra were also acquired to obtain a quantitative measure of different surface groups (Figure 2.16). Although no apparent change in the signals shape is detected, quantitative analysis of the spectra, reported in Table 2.6,

detected significant differences in the surface chemistry of the analyzed samples.

Table 2.6 Chemical shifts and relative amounts of Q^n structural units in SiO_2-ST, SiO_2-APTES and SiO_2-HNP_3, obtained thought profile-fitting analysis. Confidence level > 97%.

structural unit	**Q^2**	**Q^3**	**Q^4**
δ (ppm)	*-92.7*	*-100.5*	*-109.5*
SiO_2-ST	3.8	23.4	72.8
SiO_2-APTES	4.6	21.7	73.7
SiO_2-HNP_3	1.5	22.4	76.1

In detail, the increase of Q^4 intensity upon functionalization is expected due to the increase of condensation. In contrast with the CPMAS spectra, where Q^2 and Q^3 drastically decreased upon functionalization, in MAS spectra the amount of Q^2 and Q^3 detected in SiO_2-ST is almost unchanged in SiO_2-APTES. This could be explained by the re-esterification of Si-O-Si to form additional surface ethoxy groups. MAS NMR results also reveal that the grafting of PB chains leads to an increase of condensation and a strong reduction of Q^2. This difference of CPMAS and MAS could be explained by the formation of additional Si-O-C bonds and increase of condensation, since CPMAS is more sensitive to Si-OH functionalities.

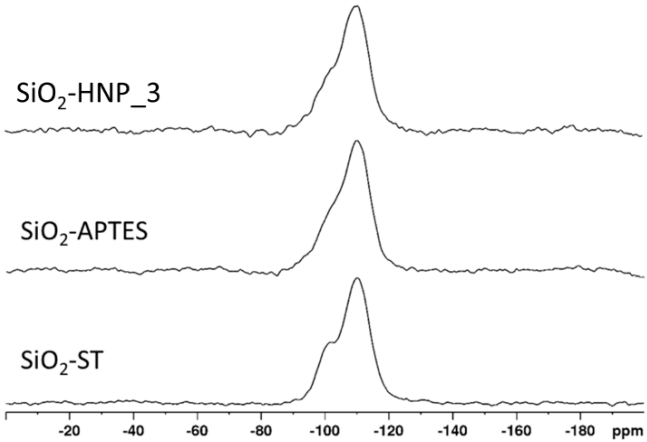

Figure 2.16 ^{29}Si proton decoupled MAS NMR spectra of SiO_2-ST, SiO_2-APTES and SiO_2-HNP_3. Adapted from Tripaldi *et al.*[1]

2.3.2.5. Small Angle X-ray Scattering (SAXS)

SAXS is often used as an effective method for the study of NPs and HNPs self-assembly since it allows the determination of morphological features and the study of the formation of NPs superstructures.[30,32,33]

SAXS curves of dry SiO_2-ST, SiO_2-APTES and SiO_2-HNP_3 powders are reported in Figure 2.17. Results for all samples show the typical behavior of spherical nano-objects,[34,35] i.e., the oscillations of the form factor. These oscillations become less sharp as SiO_2-ST are functionalized, especially after PB grafting, due to the increase in size polydispersity and alteration of the spherical NP shape.

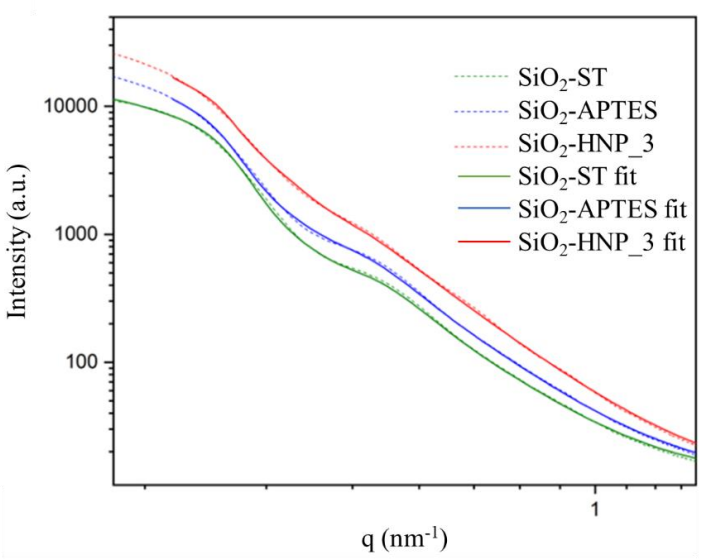

Figure 2.17 SAXS curves of SiO_2-ST, SiO_2-APTES and SiO_2-HNP_3 dry powders. Adapted from Tripaldi *et al.*[1]

Furthermore, all samples show a shift of the curve inflections to increasingly *q* values as functionalization is introduced, indicating that NPs sizes are increasing and confirming the presence of polymeric shell. An estimation of NPs sizes, dispersity and interparticle distance was obtained from fitting of SAXS data and is reported in Table 2.7. Particle sizes (D) increase from 27 nm in SiO_2-ST to 29 in SiO_2-APTES and reach 31 nm for SiO_2-HNP_3, confirming the trends observed from TEM analysis. Particle-to-particle distance (DC) reports the same trend. Size polydispersity (ζ) becomes significantly larger in SiO_2-HNP due to the higher aggregation of silica particles induced by the interaction between the grafted polymer chains.

Table 2.7 Particle size (D), size polydispersity (ζ) and average particle-particle distance (D_C) of SiO_2-ST, SiO_2-APTES and SiO_2-HNP_3 obtained from fitting of SAXS data.

Sample	D (nm)	ζ (%)	D_C (nm)
SiO_2-ST	27	18.2	34.8
SiO_2-APTES	29	18.8	35.5
SiO_2-HNPs	31	22	36

2.3.3. Characterization of cis-PB NCs

SiO_2-ST, SiO_2-APTES and SiO_2-HNP_3 samples were used to prepare NC films by a solvent-casting approach, using a cis-PB matrix. The obtained NCs were characterized by SEM and TEM, as shown in Figure 2.18, to provide a preliminary indication of their distribution and assembly behavior in polymer matrices.

SEM images of cis-PB NC films provide an indication of the HNPs organization in a polymer matrix. In detail, SEM of SiO_2-ST shows very strong aggregation in large clusters due to the attractive short-range interactions of non-functionalized silica NPs. Functionalization with APTES improves NPs distribution and dispersion within the matrix by increasing the filler/matrix compatibilization due to the higher hydrophobicity of SiO_2-APTES surface. Therefore, SEM analysis of SiO_2-APTES reveals smaller and well-dispersed clusters of NPs. Finally, after the grafting of PB chains, SEM images of SiO_2-HNP_3 show that the filler distribution is further improved, and the presence of string-like anisotropic domains can be detected.

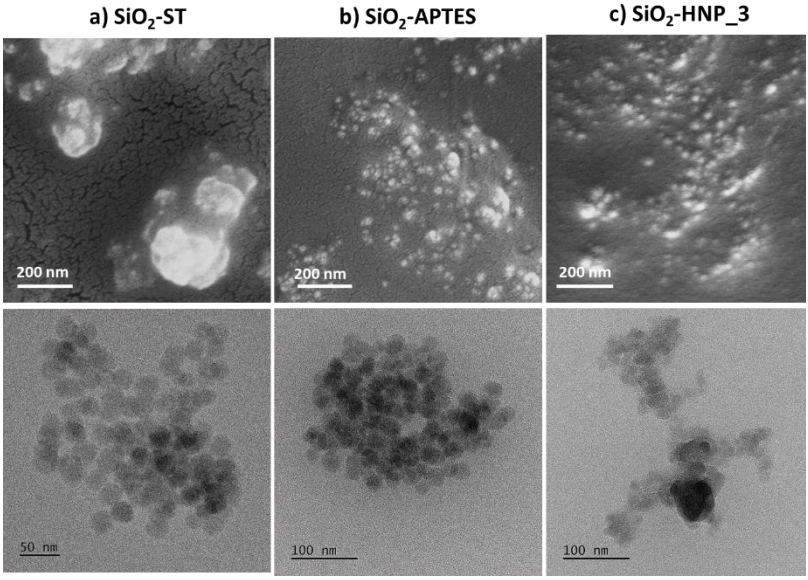

Figure 2.18 SEM (top) images and TEM (bottom) micrographs of a) SiO_2-ST, b) SiO_2-APTES and c) SiO_2-HNP_3 dispersed in cis-PB NCs. Adapted from Tripaldi *et al.*[1]

TEM analysis was used to investigate the presence of organized structures of HNPs in cis-PB NCs. TEM images of SiO_2-ST and SiO_2-APTES both show the presence of mostly spherical aggregates with close-packing organization of NPs. On the other hand, TEM micrographs of SiO_2-HNP_3 show that PB-grafted NPs dispersed in cis-PB produce anisotropic domains that recall those observed in TEM images of matrix-free SiO_2-HNP_3 (see Paragraph 2.3.2.1).

Overall, these preliminary results suggest that functionalizing SiO_2 NPs with polymer chains not only improves the filler interaction between inorganic particle and polymer, but also results in self-assembly.

2.4. Bibliography

1 L. Tripaldi, E. Callone, M. D'Arienzo, S. Dirè, L. Giannini, S. Mascotto, A. Meyer, R. Scotti, L. Tadiello and B. Di Credico, *Soft Matter*, 2021, **17**, 9434–9446.

2 W. Stöber, A. Fink and E. Bohn, *J. Colloid Interface Sci.*, 1968, **26**, 62–69.

3 E. Pratsinis, *Fuel Energy Abstr.*, 1998, **39**, 384.

4 D. Boldridge, *Aerosol Sci. Technol.*, 2010, **44**, 182–186.

5 T. Wu, Y. Zhang, X. Wang and S. Liu, *Chem. Mater.*, 2008, **20**, 101–109.

6 Y. Tai, J. Qian, Y. Zhang and J. Huang, *Chem. Eng. J.*, 2008, **141**, 354–361.

7 M. Bonnevide, A. M. Jimenez, D. Dhara, T. N. T. Phan, N. Malicki, Z. M. Abbas, B. Benicewicz, S. K. Kumar, M. Couty, D. Gigmes and J. Jestin, *Macromolecules*, 2019, **52**, 7638–7645.

8 G. H. Bogush, M. A. Tracy and C. F. Zukoski, *J. Non. Cryst. Solids*, 1988, **104**, 95–106.

9 G. H. Bogush and C. F. Zukoski IV, *J. Colloid Interface Sci.*, 1991, **142**, 1–18.

10 S. K. Kumar, N. Jouault, B. Benicewicz and T. Neely, *Macromolecules*, 2013, **46**, 3199–3214.

11 A. van Blaaderen and A. P. M. Kentgens, *J. Non. Cryst. Solids*, 1992, **149**, 161–178.

12 T. I. Suratwala, M. L. Hanna, E. L. Miller, P. K. Whitman, I. M. Thomas, P. R. Ehrmann, R. S. Maxwell and A. K. Burnham, *J. Non. Cryst. Solids*, 2003, **316**, 349–363.

13 E. Bourgeat-Lami and J. Lang, *J. Colloid Interface Sci.*, 1998, **197**, 293–308.

14 F. Kunc, V. Balhara, Y. Sun, M. Daroszewska, Z. J. Jakubek, M. Hill, A. Brinkmann and L. J. Johnston, *Analyst*, 2019, **144**, 5589–5599.

15 W. Yuan, F. Wang, Z. Chen, C. Gao, P. Liu, Y. Ding, S. Zhang and M. Yang, *Polym. (United Kingdom)*, 2018, **151**, 242–249.

16 P. Akcora, H. Liu, S. K. Kumar, J. Moll, Y. Li, B. C. Benicewicz, L. S. Schadler, D. Acehan, A. Z. Panagiotopoulos, V. Pryamitsyn, V. Ganesan, J. Ilavsky, P. Thiyagarajan, R. H. Colby and J. F. Douglas, *Nat. Mater.*, 2009, **8**, 354–359.

17 N. J. Fernandes, H. Koerner, E. P. Giannelis and R. A. Vaia, *MRS Commun.*, 2013, **3**, 13–29.

18 A. Chremos and J. F. Douglas, *Soft Matter*, 2016, **12**, 9527–9537.

19 V. Goel, J. Pietrasik, R. Poling-Skutvik, A. Jackson, K. Matyjaszewski and R. Krishnamoorti, *Polymer (Guildf).*, 2018, **159**, 138–145.

20 F. J. Sotomayor, K. A. Cychosz and M. Thommes, *Acc. Mater. Surf. Res*, 2018, **3**, 34–50.

21 A. Torabinejad, N. Nasirizadeh, M. E. Yazdanshenas and H.-A. Tayebi, *J. Nanostructure Chem.*, 2017, **7**, 217–229.

22 S. Li, Q. Wan, Z. Qin, Y. Fu and Y. Gu, *Langmuir*, 2016, **32**, 9180–9187.

23 S. Kachbouri, N. Mnasri, E. Elaloui and Y. Moussaoui, *J. Saudi Chem. Soc.*, 2018, **22**, 405–415.

24 C. Chevigny, F. Dalmas, E. Di Cola, D. Gigmes, D. Bertin, F. Boué and J. Jestin, *Macromolecules*, 2011, **44**, 122–133.

25 M. Bonnevide, T. N. T. Phan, N. Malicki, S. K. Kumar, M. Couty, D. Gigmes and J. Jestin, *Polymer (Guildf).*, 2020, **190**, 122190.

26 R. R. Madathingal and S. L. Wunder, *Thermochim. Acta*, 2011, **526**, 83–89.

27 A. I. Barabanova, T. A. Pryakhina, E. S. Afanas'Ev, B. G. Zavin, Y.

S. Vygodskii, A. A. Askadskii, O. E. Philippova and A. R. Khokhlov, *Appl. Surf. Sci.*, 2012, **258**, 3168–3172.

28 W. J. Brittain and S. Minko, *J. Polym. Sci. Part A Polym. Chem.*, 2007, **45**, 3505–3512.

29 M. Calovi, E. Callone, R. Ceccato, F. Deflorian, S. Rossi and S. Dirè, *Materials (Basel).*, 2019, 12, 3828.

30 M. D'Arienzo, S. Diré, V. Masneri, D. Rovera, B. Di Credico, E. Callone, S. Mascotto, A. Pegoretti, F. Ziarelli and R. Scotti, *ACS Appl. Nano Mater.*, 2018, **1**, 3817–3828.

31 R. Rengarajan, V. R. Parameswaran, S. Lee, M. Vicic and P. L. Rinaldi, *Polymer (Guildf).*, 1990, **31**, 1703–1706.

32 F. Parrino, M. D'Arienzo, E. Callone, R. Conta, B. Di Credico, S. Mascotto, A. Meyer, R. Scotti and S. Dirè, *Chem. Eng. J.*, 2021, **417**, 129135.

33 B. Di Credico, I. Tagliaro, E. Cobani, L. Conzatti, M. D'arienzo, L. Giannini, S. Mascotto, R. Scotti, P. Stagnaro and L. Tadiello, *Nanomaterials*, , DOI:10.3390/nano9010046.

34 W. Szczerba, R. Costo, S. Veintemillas-Verdaguer, M. Del Puerto Morales and A. F. Thünemann, *J. Appl. Crystallogr.*, 2017, **50**, 481–488.

35 T. Li, A. J. Senesi and B. Lee, *Chem. Rev.*, 2016, **116**, 11128–11180.

Chapter 3.

Rubber nanocomposites with SiO_2 HNPs

3.1. Overview

Chapter 3 reports the preparation and characterization of rubber NCs with SiO_2 HNPs. SiO_2 HNPs with different degrees of grafting density,[1] as reported in Chapter 2, were mixed with a SBR matrix in a tyre formulation to prepare rubber NCs Figure 3.1 Schematic representation of the preparation of rubber NCs with ex-situ functionalized SiO2-HNP and compared with standard NCs containing silica NPs. The approach to prepare SiO_2-Y/SBR NCs (Y = ST, APTES, HNP_X) is based on the so-called "*ex-situ"* preparation, in which filler NPs are compatibilized and functionalized with an organic molecule previously to their addition to the polymer matrix. Conversely, in the "in-situ" approach the organic coupling agent, typically a silane molecule, is added directly to the mixing chamber.

Although it entails an additional step in the rubber NCs preparation, the *"ex-situ"* approach offers some fundamental advantages: i) the optimal control of filler surface chemistry, ii) the improvement of the filler-polymer interaction and iii) the subsequent improvement of the filler-polymer interface and the formation of the filler network.[2,3]

The mechanical properties of the rubber NCs were analyzed by oscillatory rheometry and tensile tests, while the filler distribution and crosslinking density were analyzed by TEM and swelling tests respectively. By dispersing SiO_2 HNPs grafted with PB chains in a SBR matrix, the distribution of filler particles is accurately controlled, and self-assembly behaviors can be observed.[4–6] The control of filler distribution was reflected in an improvement of the mechanical properties of the materials,[7–10] showing increased reinforcement and lower Payne effect, strictly related to the self-organized SiO_2 HNPs superstructures.

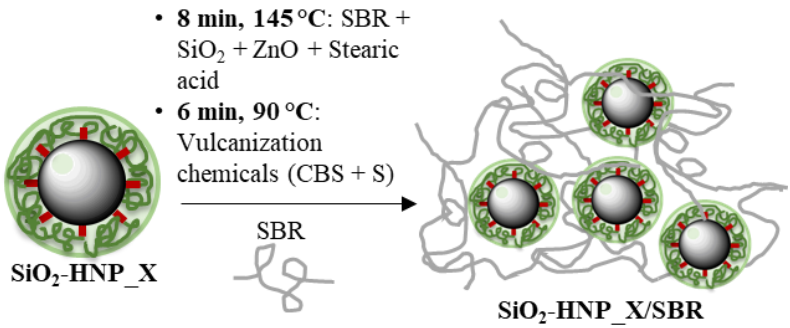

Figure 3.1 Schematic representation of the preparation of rubber NCs with ex-situ functionalized SiO_2-HNP_X.

3.2. Sample preparation

3.2.1. Materials

SiO_2-ST, SiO_2-APTES and SiO_2-HNP_X (X = 3, 4, 6) were synthesized according to the procedure reported in Chapter 2 and used as dry powders. SBR was Europrene SOL R C2525 from Versalis (26% styrene; 24% vinyl; 50% butadiene); stearic acid was Stearina TP8 from Undesa; sulfur was from Zolfoindustria; zinc oxide was from Zincol Ossidi; *N*-cyclohexyl-2-benzothiazole sulfenamide (CBS) was Vulkacit CZ/C from Lanxess.

3.2.2. Preparation of SiO_2-Y/SBR NCs

Uncured NCs were prepared in a Brabender Plasti-Corder lab station internal mixer (65 mL mixing chamber, 0.6 filling factor). Formulations of the NCs are reported in Table 3.1. The compounding procedure was composed of two mixing steps performed at different temperatures (145 and 90 °C), according to the thermal stability of the reactants.

Table 3.1 Formulations of the rubber NCs. All amounts are in phr.

Sample	Step 1 145 °C, 8 min				Step 2 90 °C, 6 min	
	SBR	**Filler**	**Stearic acid**	**ZnO**	**CBS**	**S**
SiO_2-ST/SBR	100	35	2	2	3	1
SiO_2-APTES/SBR	100	35	2	2	3	1
SiO_2-HNP_3/SBR	100	35	2	2	3	1
SiO_2-HNP_4/SBR	100	35	2	2	3	1
SiO_2-HNP_6/SBR	100	35	2	2	3	1

In the first step, SBR was masticated at 145 °C and 60 rpm rotor speed. 35 parts per hundred rubber (phr) of SiO_2, calculated by taking into account the degree of functionalization, were added in three subsequent portions to facilitate the incorporation of the filler. Two minutes after the last filler addition, zinc oxide (2 phr) and stearic acid (2 phr) were added; this lag time avoids the secondary reaction between ZnO and silica silanols.

In the second step, the compound was reloaded in the internal mixer operating at 90 °C at 60 rpm. CBS (3 phr) and sulfur (1 phr) were then added and mixed for 2 min. After unloading, composites were further molded for 2 min in a rolling mill to produce sheets of about 2 cm thick for vulcanization and mechanical testing. Uncured NCs are labelled SiO_2-Y/SBR (Y = ST, APTES, HNP_3, HNP_4, HNP_6).

Finally, cured composites were obtained by vulcanization performed in a hydraulic press at 170 °C and 100 bar for 30 min. Vulcanized NCs are labelled V-SiO_2-Y/SBR (Y = ST, APTES, HNP_3, HNP_4, HNP_6).

3.3. Results and discussion

Rheological and dynamic-mechanical analyses were performed in order to evaluate the effect of SiO_2-HNP fillers in comparison to bare SiO_2.

Dynamic-mechanical properties of the cured and uncured NCs, *i.e.* storage modulus G', loss modulus G'' and loss tangent tanδ, were tested by oscillatory shear rheometry. From these results, reinforcement, Payne effect and hysteresis of the materials were estimated and discussed. Tensile tests were performed to determine the behavior of the NCs under large deformations and to evaluate the stress and elongation at break.

The morphology of the cured NCs was evaluated by TEM analysis, with in-depth analysis of NPs dispersion, distribution and self-organization within the polymer matrix. The effect of PB grafting density on the organization of SiO_2 HNPs in superstructures was evaluated and related to the functional properties. Finally, swelling tests in toluene provided an estimation of the extractable rubber fraction and degree of bound rubber in each of the V-SiO_2-Y/SBR .

Experimental details of all characterization techniques are reported in Appendix A.

3.3.1. Mechanical testing

Vulcanization curves for the prepared NCs were acquired by Rubber Process Analyzer (RPA). The vulcanization curves for V-SiO_2-Y/SBR NCs, obtained by measuring the variation of viscosity over the time

with the torque requested to keep the rotor at a constant rate, are reported in in Figure 3.2.

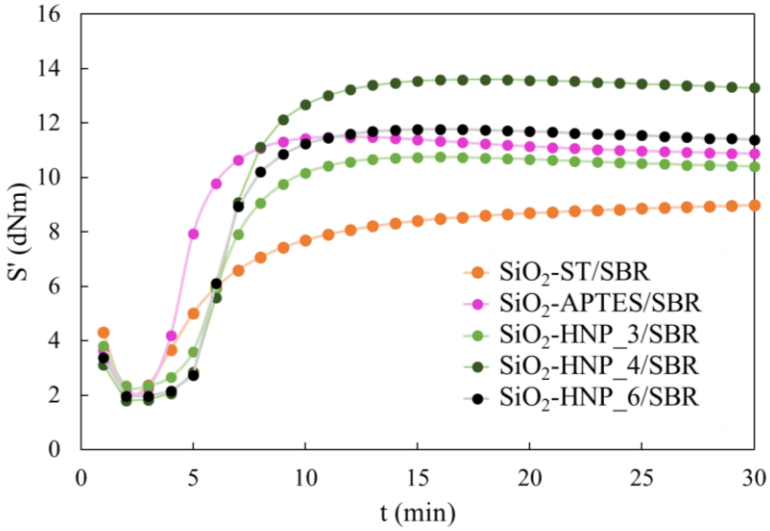

Figure 3.2 Vulcanization curves of V-SiO_2-Y/SBR NCs NCs.

The vulcanization characteristics of V-SiO_2-Y/SBR NCs are expressed in terms of the following parameters:

(i) the higher maximum torque (M_H, the torque measured when the sulfur reticulation is complete);

(ii) the lower minimum torque (M_L, the torque measured before the beginning of the crosslinking reaction);

(iii) the lower scorch time (t_S, the time to reach the first sign of incipient cross-linking).[11]

These values are reported in

Table 3.2.

Table 3.2 Vulcanization properties of V-SiO_2-Y/SBR NCs.

Sample	t_{s2} (min)	M_L (dNm)	M_H (dNm)	M_H-M_L (dNm)
SiO_2-ST/SBR	5	2.09	8.99	6.90
SiO_2-APTES/SBR	4	2.22	11.49	9.27
SiO_2-HNP_3/SBR	5	2.35	10.75	8.40
SiO_2-HNP_4/SBR	5	1.80	13.60	11.80
SiO_2-HNP_6/SBR	5	1.97	11.77	9.80

The scorch time t_S, defined as the time needed for the vulcanization to start, is a crucial parameter for the industrial moulding of the material.[12] As reported in Table 2, the scorch time of all the samples is about 5 min, except for SiO_2-APTES/SBR, which exhibits a shorter scorch time of 4 min.

The minimum torque M_L, related to the viscosity of the compounds, reflects the filler dispersion aptitude in the uncured samples. In V-SiO_2-Y/SBR NCs, the M_L values are in the range of 2.35-1.80 dNm, indicating a good dispersion of all filler NPs. In particular, the V-SiO_2-4/SBR and V-SiO_2-6/SBR NCs showed lower ML, likely due to the presence of higher density of PB polymer on the HNPs surface inducing a better interaction of the filler with polymer matrix and consequently a more efficient dispersion.

The incorporation of SiO_2 HNPs in SBR matrix gives satisfactory value of the maximum torque M_H, which is a measure of crosslink

density and stiffness of the rubber, [9,11] including also the contribution of filler-network. In particular, the enhanced M_H of V-SiO_2-4/SBR and V-SiO_2-6/SBR NCs with respect to both V-SiO_2-ST/SBR and V-SiO_2-APTES/SBR suggests excellent interaction between silica and rubber in modified SiO_2-HNP_X cured composites, due to the presence of the polymer shell. Therefore, the NCs containing SiO_2-HNP with higher polymer shell grafting density show not only better dispersibility and surface chemistry but also the best interaction with the sulfur-based vulcanization compounds, leading to enhanced mechanical properties in the rubber composition.

The high M_H-M_L values found for V-SiO_2-HNP_X/SBR with X = 3, 4 and 6 samples confirm the excellent interaction with the sulfur-based vulcanization compounds. With respect to these samples, the NCs containing silica or silica functionalized only with APTES show slightly lower values of about 2-4 dNm. In relation to the reference material containing Stöber silica, the M_H value indicates a low vulcanization grade, probably due to the presence of large amounts of acidic silanol groups on the surface of the SiO_2 NPs.

After evaluating the effectiveness of curing process, a detailed investigation of the dynamic-mechanical behavior of the composites was performed by RPA analysis, which allows to evaluate the effect of filler networking and of SiO_2-HNPs and polymer interaction.

Curves of the storage modulus G' before and after vulcanization for SiO_2-Y/SBR NCs are reported in Figure 3.3. Curves of loss modulus G'' and loss tangent tanδ of vulcanized samples are reported in Figure 3.4 and Figure 3.5 respectively. Values of G′(6%), Δ(G′(0.4%)-G′(10%)), and tanδ(6%), representative of the NCs reinforcement, Payne effect and hysteresis respectively,[7] are reported in Table 3.3.

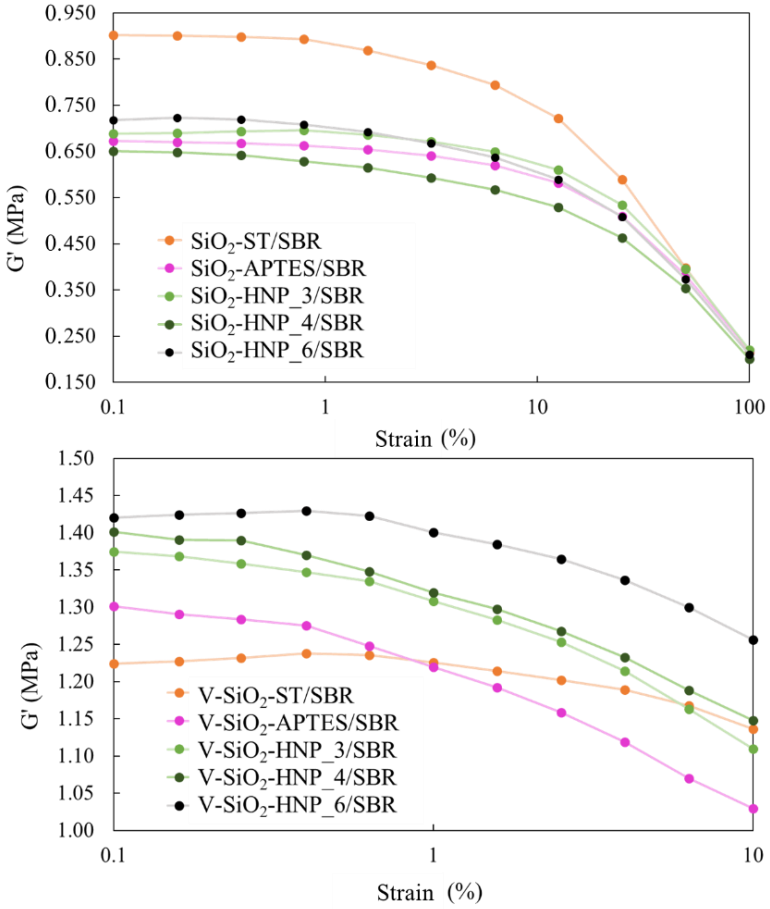

Figure 3.3 Storage modulus G' *vs* strain of uncured (top) and cured (bottom) SiO_2-Y/SBR NCs.

A pronounced nonlinear dependence of the modulus, known as Payne effect,[13] is observed in all cases. In fact, the G′ value at low strain decreases rapidly by increasing the strain amplitude and, at large strain, it approaches the lowest value. In details, before curing (top of

Figure 3.3), the modulus at low and high strain resulted very similar for all the composites, except for the reference material.

Table 3.3 Values of storage modulus G'(6%), Δ(G′(0.4%)-G′(10%)) and tanδ(6%) for V-SiO_2-Y/SBR NCs .

Sample	G′(6%) (MPa)	Δ(G′(0.4%)-G′(10%)) (MPa)	tanδ (6%)
V-SiO_2-ST/SBR	1.168	0.102	0.169
V-SiO_2-APTES/SBR	1.070	0.246	0.165
V-SiO_2-HNP_3/SBR	1.163	0.238	0.174
V-SiO_2-HNP_4/SBR	1.189	0.222	0.139
V-SiO_2-HNP_6/SBR	1.300	0.173	0.165

After curing (bottom of Figure 3.3), a remarkable increase of the modulus either at low or at high strain was observed for all the composites, except for the sample SiO_2-ST/SBR, due to very high filler aggregation.[13,14] In fact, the refence material V-SiO_2-ST/SBR shows a relatively flat curve, with the lowest reinforcement and lowest Δ(G′(0.4%)-G′(10%)), as reported in Table 3.3.

This indicates that filler NPs are too aggregated to result in effective percolation of the filler network.[15,16] The use of SiO_2-APTES results in a strong increase of Payne effect, while the reinforcement of V-SiO_2-APTES/SBR is still very low.

On the contrary, NCs samples containing HNPs show much higher reinforcement and lower Payne effect with respect to V-SiO_2-

APTES/SBR. This points to the positive impact of filler functionalization with macromolecules, such as PB, with respect to that of small silane molecules on the filler-rubber interaction and, in turn, on the mechanical properties. This suggests a strong immobilization of the polymer chains close to the nanofiller surfaces or within their network, which increases the mechanical reinforcement of the composites.

Evidently, after grafting the macromolecules on the filler surface, the interaction of the NPs with the polymer chains improves as well as the cross-linking coupling. In particular, V-SiO_2-HNP_6 clearly shows the best performance, exhibiting the highest value of G'(6%) (1.300 MPa) and the lowest Δ(G′(0.4%)-G′(10%)) (0.173 MPa) compared to all other samples.

The curves of loss modulus G'' (Figure 3.4) show the viscous contribution to the mechanical response of the materials. All samples show a broad maximum in the G'' curve at around 1% of strain. This maximum indicates the maximum strain at which the NC sustains the deformation without undergoing a breakdown of the filler network.[9]

The high value of G'' for the sample V-SiO_2-HNP_6/SBR may thus be rationalized by considering that higher loss moduli correspond to the breakdown of a stronger filler network due to the presence of higher amounts of rigid rubber. This is consistent with the higher values of reinforcement obtained from G' curve of V-SiO_2-HNP_6/SBR.

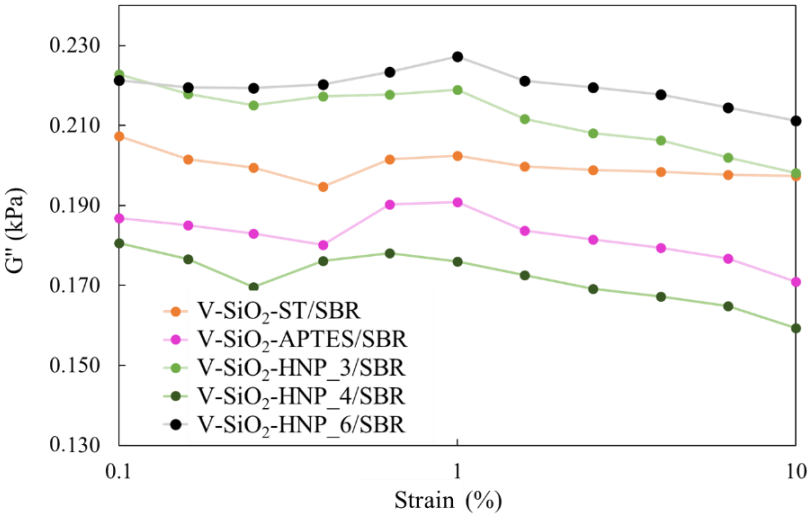

Figure 3.4 Curves of loss modulus G'' for V-SiO_2-Y/SBR NCs.

The curves of tanδ, obtained from the ratio between the storage and loss moduli, describe the dissipation of energy during the deformation of the sample, a parameter also known as hysteresis. The curves of tanδ vs. strain are reported in Figure 3.5. Values of tanδ (6%), reported in Table 3.3, are representative of the hysteresis of the samples and can be associated to hysteresis. The sample V-SiO_2-HNP_4/SBR shows the lowest values of tanδ across the whole deformation. Thus, the SiO_2-HNP_4 filler appears to significantly improve rolling resistance while maintaining a very high value of reinforcement.

Compared to V-SiO_2-HNP_4, NCs with SiO_2-HNP_X having both higher (X = 6) and lower (X= 3) polymer surface coverage show a slightly increased hysteresis, indicating that intermediate coverage

might compensate between filler-filler aggregation and dissipative effects due to the uncrosslinked chains of the polymer shell.

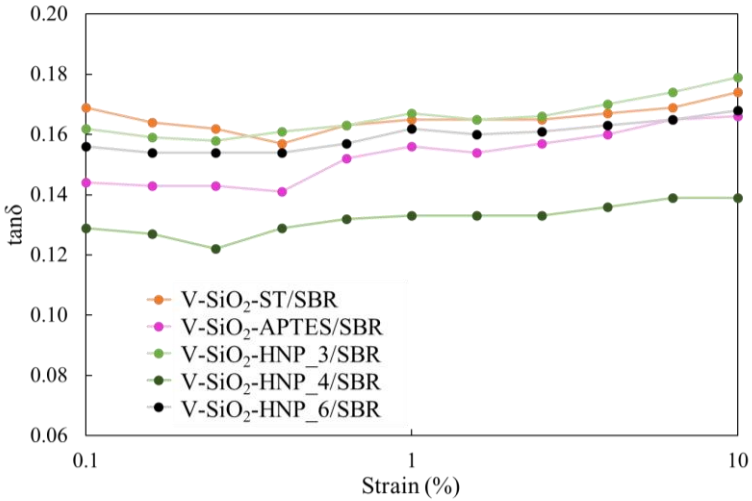

Figure 3.5 Curves of tanδ for V-SiO_2-Y/SBR NCs.

Tensile stress/strain tests were performed on all cured samples to study the performance of the materials at high strain. Stress/strain curves obtained from tensile tests are reported in Figure 3.6, while values of elongation at break E_B and stress at break S_B are reported in Table 3.4.

V-SiO_2-ST/SBR shows the lowest values of stress at all strain values, supporting the conclusion that high filler aggregation prevented the formation of the filler network. In V-SiO_2-HNP_X/SBR NCs, the slope of the stress/strain curves consistently increases by increasing functionalization. In particular, V-SiO_2-HNP_6/SBR shows the highest stress across the strain range, indicating the highest degree of reinforcement.[8] V-SiO_2-HNP_6/SBR also showed the highest value of S_B (5.3±0.2 MPa) and the lowest E_B (460±20%) suggesting that the

reinforcing filler network provided by the HNPs self-organization increases the amount of rigid rubber in the sample. This is consistent with the results obtained from dynamic-mechanical analysis.

Table 3.4 Values of S_B and E_B* for V-SiO_2-Y/SBR NCs.

Sample	S_B (MPa)	E_B (%)
V-SiO_2-ST/SBR	2.1±0.2	700±100
V-SiO_2-APTES/SBR	4.6±0.3	550±10
V-SiO_2-HNP_3/SBR	4.8±0.3	570±50
V-SiO_2-HNP_4/SBR	3.7±0.1	480±10
V-SiO_2-HNP_6/SBR	5.3±0.2	460±20

**Each value is the average of three tested specimens.*

3.3.2. Morphological characterization

The effect of silica functionalization with macromolecules on the dispersion of filler NPs was investigated by TEM analysis of V-SiO_2-Y/SBR NCs. Thus, morphological observations were correlated to the dynamic-mechanical data in order to highlight the role of the functionalization in enhancing the functional properties. TEM micrographs of the vulcanized NCs with bare and APTES-functionalized SiO_2 NPs are reported in Figure 3.7, while micrographs of NCs containing SiO_2 HNPs are in Figure 3.8.

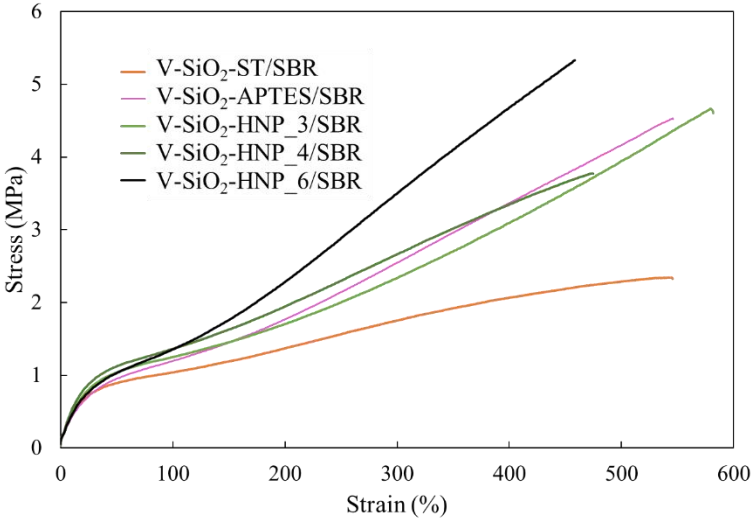

Figure 3.6 Stress-strain curves for V-SiO_2-Y/SBR NCs. For each sample, three specimens were tested. Here, only one representative curve per sample is reported.

V-SiO_2-ST/SBR (a and a' in Figure 3.7) shows very large micrometric clusters with very poor filler dispersion in the matrix.

SiO_2-ST clusters show no intercalation of rubber matrix between the particles. This morphological distribution is consistent with the results of the mechanical analysis of the sample, showing very low reinforcement and Payne effect, which indicate that no filler network occurs.

This effect of SiO_2-ST NPs aggregation is due to their high hydrophilicity attributable to the large amount of surface silanol and ethoxy groups, as discussed in Chapter 2.

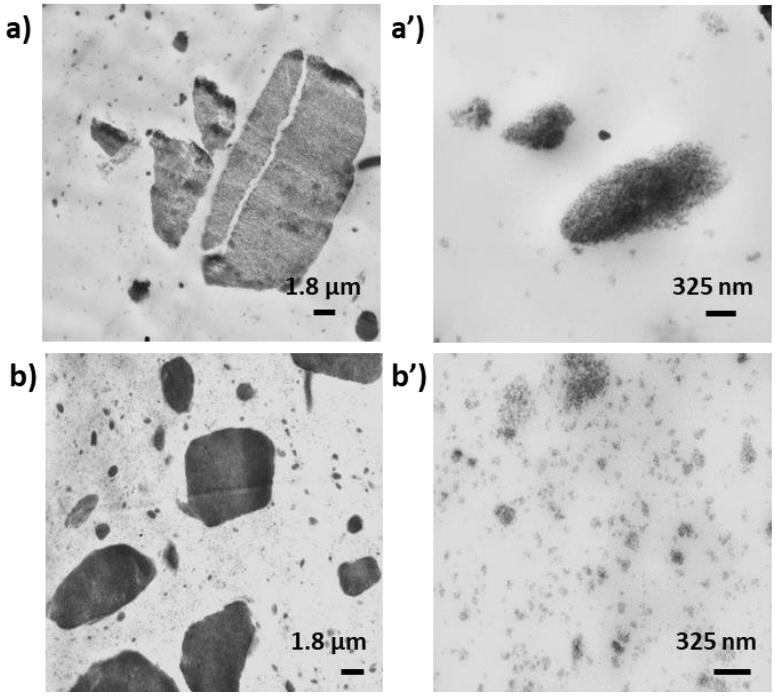

Figure 3.7 TEM micrographs at two different magnifications of V-SiO_2-ST/SBR (a and a') and V-SiO_2-APTES/SBR (b and b').

In NCs prepared with SiO_2-ST functionalized with APTES (b and b' in Figure 3.7), filler clusters appear smaller in size and the overall filler dispersion is improved due to surface silanization, which, as expected, increases the compatibilization with the rubber matrix. However, no rubber seems to be present between NPs inside the cluster, as highlighted by the darker color of NPs aggregates. NPs clusters appear spherical, and no evidence of self-organization is observed.

The samples V-SiO_2-HNP_3/SBR and V-SiO_2-HNP_4/SBR (a and b in Figure 3.8), containing HNPs, exhibit a partial aggregation of filler particles. The rubber matrix shows several zones poorer in filler particles: that is, the polymer network appears to be more discontinuous. However, images at higher magnification (a' and b' in Figure 3.8) reveal a more complex spatial distribution of filler. Indeed, the presence of enclosed rubber between each filler particle is clearly visible and the anisotropic structures consisting of HNPs aligned along a preferential orientation reveal the effective self-organization of NPs having a polymeric shell.[4,5]

Therefore, TEM images clearly show the presence of "filler network structures", consisting not only of directly interacting particles, but also of polymer chains bridging the particles. This filler-rubber interaction is evident by the rubber layer surrounding the particles aligned along a preferential orientation. This fiber organization occurs despite the mixing process used to obtain the composites and although no external or internal procedure was per- formed to drive the particle arrangement.[17]

The HNPs self-organization was previously reported in the literature[18,19] for HNPs based on polymers with high T_g, such as PS-grafted HNPs dispersed in an homopolymer matrix. Instead, HNPs functionalized with rubbery polymers having low T_g, such as PB[20,21] or polyisoprene[4,22] have been rarely reported. To the best of our knowledge, no work has yet systematically investigated the direct relationship between the synergic interaction of SiO_2-HNPs with PB shell in the rubber NCs and the final mechanical material properties.

Finally, the sample V-SiO_2-HNP_6 (c and c' in Figure 3.8) shows large micrometric superstructures, similar to the clusters of V-SiO_2-ST/SBR, although less dense. Nevertheless, these superstructures consist of HNPs with enclosed rubber between each filler particle.

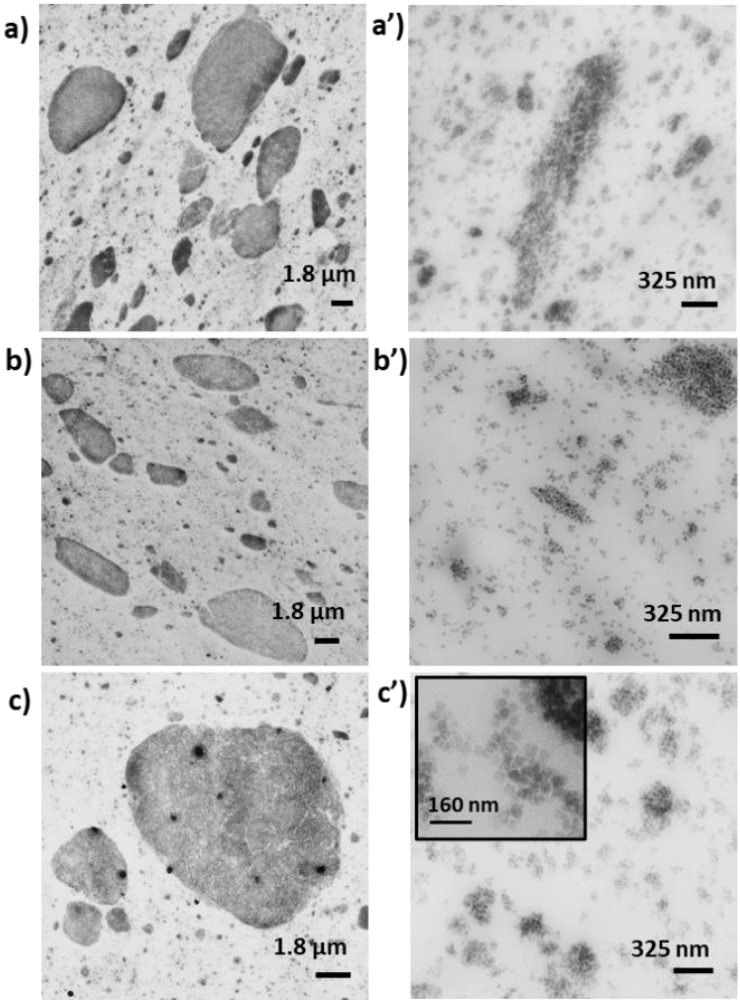

Figure 3.8 TEM micrographs at two different magnifications of V-SiO_2-HNP_3/SBR (a, a'), V-SiO_2-HNP_4/SBR (b, b'), V-SiO_2-HNP_6/SBR (c, c').

Differently from V-SiO_2-HNP_3/SBR and V-SiO_2-HNP_4/SBR, HNPs clusters appear spherical in shape. Anisotropic structures appear only at lower degrees of polymer grafting.[23] Nonetheless, at higher magnification the presence of "string-like" anisotropic structures of HNPs is clearly visible.

These string-like structures were also observed in matrix-free conditions,[1] as discussed in Chapter 2. Interestingly, the presence of such interconnected structures correlates with an improvement of the mechanical properties of the NC, leading to higher reinforcement and lower Payne effect, while also increasing stress and elongation at break.

Overall, TEM analysis confirmed that grafting PB chains onto spherical SiO_2 NPs leads to a controlled distribution of filler particles within the matrix, which provides control over the mechanical properties of the NC material.

Morphological analysis in combination with mechanical tests clearly shows that HNPs self-assembly results in an improvement of the mechanical properties of V-SiO_2-HNP_X/SBR, *i.e.* higher reinforcement and lower Payne effect as well as improved elongation and stress at break.

3.3.3. Swelling and extraction experiments

Swelling and extraction experiments in toluene were performed on cured V-SiO_2-Y/SBR samples to evaluate the effect of the filler on the degree of crosslinking in the samples.

The crosslink density (ν) in each sample was evaluated following the procedure reported in the Appendix. The values of ν for the V-SiO_2-Y/SBR NCs are illustrated in Figure 3.9 and reported in Table 3.5.

Table 3.5 Values of crosslink density *v* for V-SiO_2-Y/SBR.

Sample	Crosslink density *v* (mol/cm^3)
V-SiO_2-ST/SBR	4.88×10^{-6}
V-SiO_2-APTES/SBR	6.65×10^{-6}
V-SiO_2-HNP_3/SBR	4.97×10^{-6}
V-SiO_2-HNP_4/SBR	7.99×10^{-6}
V-SiO_2-HNP_6/SBR	14.28×10^{-6}

Swelling experiments on the cured V-SiO_2-Y/SBR samples confirm that the presence of the polymer shell tends to reduce bound rubber of the uncured NCs, namely the amount of non-crosslinked rubber loosely bound to the filler HNPs, resulting in a higher degree of crosslinking density. As expected, SiO_2-ST/SBR NC presents the lowest value of *v*, suggesting that i) the vulcanization efficiency is low due to the acidic silanol groups, as shown in Paragraph 3.3.1 and ii) the high aggregation and low compatibilization of filler NPs prevents the formation of effective filler-rubber interactions. Thus, the crosslink density of the control sample is relatively low. This is in line with both mechanical tests, showing very low reinforcement and stress at break, and TEM analysis, showing large and dense NPs aggregates.

SiO_2-APTES NPs functionalized with amino-silane when embedded in the SBR matrix improves the crosslinking density due to the improved dispersion of SiO_2-APTES NPs and their good interaction with the rubber matrix. On the other hand, as previously reported, V-

SiO_2-APTES/SBR sample shows higher Payne effect with respect to samples containing HNPs.

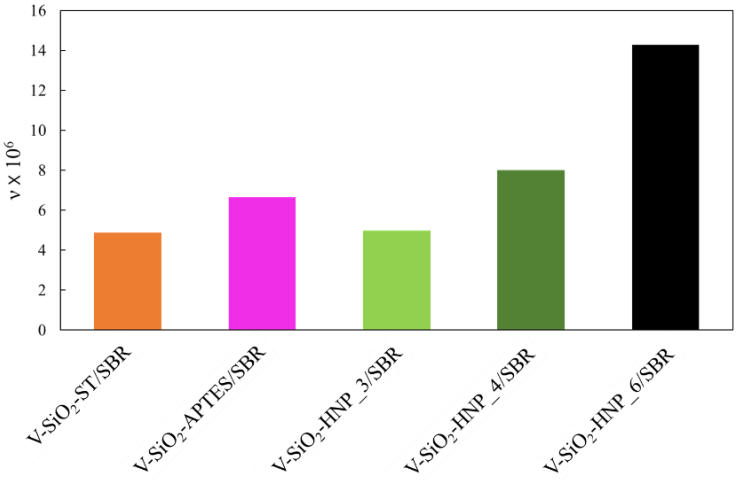

Figure 3.9 Graph illustrating the values of crosslinking density ν for the V-SiO_2-Y NCs.

Considering the case of HNPs, by increasing the grafting density of SiO_2 HNPs the crosslinking density increases accordingly, in particular for the sample V-SiO_2-HNP_6/SBR. This is indicative of a high interaction between the silica filler and the polymer matrix in modified SiO_2-HNP_X cured composites, due to the presence of the polymer shell. These outcomes may be explained by referring to the peculiar surface properties of HNPs for improved coupling with the non-crosslinked host elastomer, confirming the high reactivity of HNPs with vulcanizing compounds with respect to the conventional sulfur-bridged bis-alkoxy silanes.

Therefore, we can conclude that PB polymer partakes in the vulcanization process by forming chemical bonds with the SBR matrix.

These results are consistent with the mechanical and morphological characterization of the samples, showing that the sample V-SiO_2-HNP_6/SBR possesses the highest reinforcement, largest stress at break and lowest elongation at break.

Generally, the results demonstrate that for all V-SiO_2-HNP_X/SBR composites a satisfactory degree of crosslinking density is achieved.

3.4. Bibliography

1 L. Tripaldi, E. Callone, M. D'Arienzo, S. Dirè, L. Giannini, S. Mascotto, A. Meyer, R. Scotti, L. Tadiello and B. Di Credico, *Soft Matter*, 2021, **17**, 9434–9446.

2 Y. Song, J. Yu, D. Dai, L. Song and N. Jiang, *Mater. Des.*, 2014, **64**, 687–693.

3 L. Wahba, M. D'Arienzo, S. Dirè, R. Donetti, T. Hanel, F. Morazzoni, M. Niederberger, N. Santo, L. Tadiello and R. Scotti, *Soft Matter*, 2014, **10**, 2234–2244.

4 P. Akcora, H. Liu, S. K. Kumar, J. Moll, Y. Li, B. C. Benicewicz, L. S. Schadler, D. Acehan, A. Z. Panagiotopoulos, V. Pryamitsyn, V. Ganesan, J. Ilavsky, P. Thiyagarajan, R. H. Colby and J. F. Douglas, *Nat. Mater.*, 2009, **8**, 354–359.

5 M. Bonnevide, A. M. Jimenez, D. Dhara, T. N. T. Phan, N. Malicki, Z. M. Abbas, B. Benicewicz, S. K. Kumar, M. Couty, D. Gigmes and J. Jestin, *Macromolecules*, 2019, **52**, 7638–7645.

6 S. K. Kumar, N. Jouault, B. Benicewicz and T. Neely, .

7 B. Di Credico, E. Cobani, E. Callone, L. Conzatti, D. Cristofori, M. D'Arienzo, S. Dirè, L. Giannini, T. Hanel, R. Scotti, P. Stagnaro, L.

Tadiello and F. Morazzoni, *Appl. Clay Sci.*, 2018, **152**, 51–64.

8 L. Tadiello, M. D'Arienzo, B. Di Credico, T. Hanel, L. Matejka, M. Mauri, F. Morazzoni, R. Simonutti, M. Spirkova and R. Scotti, *Soft Matter*, 2015, **11**, 4022–4033.

9 R. Scotti, L. Conzatti, M. D'Arienzo, B. Di Credico, L. Giannini, T. Hanel, P. Stagnaro, A. Susanna, L. Tadiello and F. Morazzoni, *Polymer (Guildf).*, 2014, **55**, 1497–1506.

10 E. Cobani, I. Tagliaro, M. Geppi, L. Giannini, P. Leclère, F. Martini, T. C. Nguyen, R. Lazzaroni, R. Scotti, L. Tadiello and B. Di Credico, *Nanomaterials*, 2019, **9**, 486.

11 S. Mostoni, M. D'Arienzo, B. Di Credico, L. Armelao, M. Rancan, S. Dirè, E. Callone, R. Donetti, A. Susanna and R. Scotti, *Ind. Eng. Chem. Res.*, 2021, **60**, 10180–10192.

12 A. Susanna, M. D'Arienzo, B. Di Credico, L. Giannini, T. Hanel, R. Grandori, F. Morazzoni, S. Mostoni, C. Santambrogio and R. Scotti, *Eur. Polym. J.*, 2017, **93**, 63–74.

13 A. R. Payne, *J. Appl. Polym. Sci.*, 1962, **6**, 368–372.

14 G. Heinrich and M. Klüppel, *Adv. Polym. Sci.*, 2002, **160**, 1–44.

15 S. M. Nagaraja, S. Henning, S. Ilisch and M. Beiner, *Polymers (Basel).*, 2021, **13**, 1–16.

16 J. B. Donnet and E. Custodero, *Sci. Technol. Rubber*, 2013, 383–416.

17 R. A. Vaia and J. F. Maguire, *Chem. Mater.*, 2007, **19**, 2736–2751.

18 J. J. Park, J. Y. Lee and Y. G. Hong, *Polymer (Guildf).*, 2020, **197**, 122493.

19 M. Aakyiir, S. Araby, A. Michelmore, Q. Meng, Y. Amer, Y. Yao, M. Li, X. Wu, L. Zhang and J. Ma, *Nanotechnology*, 2020, **31**, 315715.

20 W. K. J. Mosse, M. L. Koppens, S. L. Gras and W. A. Ducker, *Langmuir*, 2010, **26**, 1013–1018.

21 S. Tang, J. M. Horton, B. Zhao and L. Zhu, *Polymer (Guildf).*, 2016, **90**, 9–17.

22 M. Giovino, J. Pribyl, B. Benicewicz and R. Bucinell, *Nanocomposites*, 2019, **4**, 244–252.

23 S. K. Kumar, N. Jouault, B. Benicewicz and T. Neely, *Macromolecules*, 2013, **46**, 3199–3214.

24 N. Suzuki, F. Yatsuyanagi, M. Ito and H. Kaidou, *J. Appl. Polym. Sci.*, 2002, **86**, 1622–1629.

25 J. L. Leblanc, *Prog. Polym. Sci.*, 2002, **27**, 627–687.

26 B. B. Boonstra, *Polymer (Guildf).*, 1979, **20**, 691–704.

27 L. Conzatti, G. Costa, L. Falqui and A. Turturro, 1–28.

28 S. H. El-Sabbagh, N. M. Ahmed, G. M. Turky and M. M. Selim, *Prog. Rubber Nanocomposites*, 2017, 249–283.

Chapter 4.

Rubber nanocomposites for technological applications

4.1. Overview

A study of the parameters controlling the self-assembly of SiO_2 NPs in NCs requires the use of well-dispersed HNPs prepared by a colloidal approach (see Chapter 2 and 3). SiO_2 HNPs prepared *ex-situ*, i.e., functionalized previously to their addition within the polymer matrix, offer precise control of aggregation phenomena and allow an accurate evaluation of surface chemistry. However, such fillers are unsuitable for large-scale production and technological applications due to the long and laborious synthesis process.

The *in-situ* functionalization of fillers is a standard approach in the tyre industry in which the coupling agents are added directly during the rubber mixing process. This approach allows the preparation of rubber NCs on a larger scale, avoiding the functionalization step, although it prevents the optimal control of the coupling reaction of organic molecules on the filler's surface.

Therefore, to achieve a technological transfer of the results obtained with HNPs, an easily scalable model system was developed by using a macromolecular silane, the commercial Shin Etsu BR Mono-silyl type (MacroSil, a in Figure 4.1), composed of a PB chain with a single triethoxysilane group. The effect of different degrees of in-situ functionalization was also evaluated. This macromolecular silane can directly react with the SiO_2 surface during the rubber mixing process, creating a homogenous polymer shell around the NPs core and effectively producing in-situ HNPs.

In this system, commercial precipitated SiO_2 was used. To isolate the influence of the macromolecular silane and distinguish it from that of a traditional, short chain coupling agent, a bimodal grafting approach was followed by adding TESPT (b in Figure 4.1). The NPs surface coverage ratio between TESPT and MacroSil was varied between

100% and 70% while keeping the total theoretical grafting density constant (c in Figure 4.1).

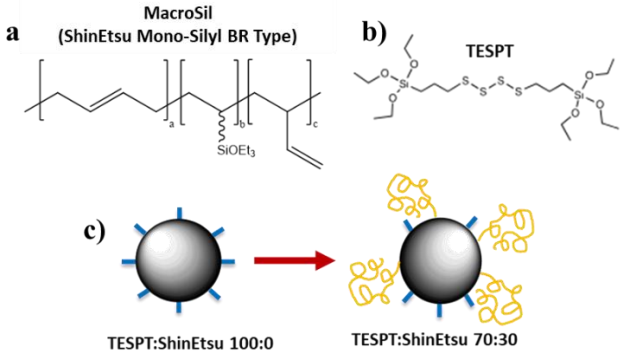

Figure 4.1 a) Molecular structure of MacroSil, b) molecular structure of TESPT and c) schematic representation of the bimodal grafting approach.

The addition of a macromolecular coupling agent increases the degree of free oligomer chains, also referred to as "dangling chains". As Xia and coworkers[1] have reported, the presence of dangling chains in vulcanized rubber impacts the mechanical properties of the material by increasing energy dissipation. For this reason, to keep the total amount of dangling chains constant in every formulation, the presence of the MacroSil chains was balanced by the addition of non-functionalized liquid polybutadiene (L-PB, Polyvest 130).

The mechanical properties of the in-situ rubber NCs were tested by conventional oscillatory rheometry, tensile tests, hardness tests and Large Amplitude Oscillatory Shear analysis (LAOS). The dispersion and distribution of filler particles was studied by TEM analysis.

4.2. Sample preparation

4.2.1. Materials

Precipitated SiO_2 Zeosil 1115 MP (BET SSA 125 m^2/g) was from Solvay; Bis[3-(triethoxysilyl)propyl] tetrasulfide (TESPT) was from Aldrich; Shin Etsu BR silane mono-silyl type X-12-1267T (MacroSil, $M_n \approx 4500$, $M_w \approx 5100$, $Si(OEt)_3 \approx 4$ wt%) was from Shin Etsu; Polyvest 130 (non-functionalized liquid polybutadiene) was from Evonik; styrene-butadiene rubber (SBR) was Europrene SOL R C2525 was from Versalis (26% styrene; 24% vinyl; 50% butadiene); stearic acid (SA) was Stearina TP8 from Undesa; sulfur was from Zolfoindustria; zinc oxide was from Zincol Ossidi; N-cyclohexyl-2-benzothiazole sulfenamide (CBS) was Vulkacit CZ/C from Lanxess.

4.2.2. Preparation of SiO_2-TSX/SBR NCs

The total grafting density (σ) of SiO_2 was estimated based on the ideal amount of TESPT silane added to rubber NCs. This value typically ranges from 3 to 8 phf (parts per hundred filler).[2,3] The maximum amount of TESPT was fixed at 5 phf, from which the σ was calculated by Equation 4.1, assuming that the silane molecule reacts with one silane group per silica particle.

$$\sigma\left(\frac{chains}{nm^2}\right) = \frac{\frac{phf}{MW_{TESPT}\left(\frac{g}{mol}\right)} N_A\ (chains/mol)}{100\ \cdot SSA\left(\frac{m^2}{g}\right) \cdot \frac{10^{18}\ nm^2}{m^2}} \qquad (4.1)$$

where MW_{TESPT} is the molecular weight of the silane before grafting, SSA is the specific surface area of SiO_2 and N_A is the Avogadro number. The resulting σ was 0.045 chains/nm^2. Herein, technological

NCs will be labelled SiO_2-TSX/SBR, where X is the TESPT/MacroSil grafting density ratio, as reported in Table 4.1.

Uncured NCs were prepared in a Brabender Plasti-Corder lab station internal mixer (65 mL mixing chamber, 0.6 filling factor). Formulations of the NCs are reported in Table 4.2. The compounding procedure was composed of two mixing steps at different temperatures (145 and 90 °C), according to the thermal stability of the reactants. In the first step, SBR was masticated at 145 °C and 60 rpm rotor speed. 60 phr of SiO_2 were manually mixed with the TESPT and MacroSil coupling agents until a homogeneous mixture was formed and added in three subsequent portions. Two minutes after the last filler addition, zinc oxide (2 phr) and stearic acid (2 phr) were added; this lag time avoids secondary reaction between ZnO and silica silanols.

Table 4.1 Grafting density ratio, TESPT grafting density and MacroSil grafting density for SiO_2-TSX/SBR NCs.

Sample	σ ratio (TESPT:MacroSil)	σ_{TESPT} (chains/nm^2)	$\sigma_{MacroSil}$ (chains/nm^2)
SiO_2-TS100/SBR	100:0	$4.47 \cdot 10^{-2}$	0
SiO_2-TS95/SBR	95:5	$4.25 \cdot 10^{-2}$	$2.23 \cdot 10^{-3}$
SiO_2-TS90/SBR	90:10	$4.02 \cdot 10^{-2}$	$4.47 \cdot 10^{-3}$
SiO_2-TS85/SBR	85:15	$3.80 \cdot 10^{-2}$	$6.70 \cdot 10^{-3}$
SiO_2-TS80/SBR	80:20	$3.58 \cdot 10^{-2}$	$8.94 \cdot 10^{-3}$
SiO_2-TS75/SBR	75:25	$3.35 \cdot 10^{-2}$	$1.12 \cdot 10^{-2}$
SiO_2-TS70/SBR	70:30	$3.13 \cdot 10^{-2}$	$1.34 \cdot 10^{-2}$
SiO_2-TS0/SBR	n.a.	0	0

In the second step, the compound was reloaded in the internal mixer operating at 90 °C at 60 rpm. CBS (3 phr) and sulfur (1 phr) were then added and mixed for 2 min. After unloading, composites were further molded for 2 min in a rolling mill to produce sheets of about 2 cm thick for vulcanization and mechanical testing. Finally, cured composites were obtained by vulcanization performed in a hydraulic press at 170 °C and 100 bar for 30 min. Vulcanized NCs are labelled V-SiO_2TSX/SBR.

Table 4.2 Formulations of technological SiO_2-TSX/SBR NCs. Amounts in phr.

Sample	SBR	SiO_2	TESPT	MacroSil	L-PB	ZnO	SA	CBS	S
SiO_2-TS100/SBR	100	60	3.00	0.00	8.35	2	2	3	1
SiO_2-TS95/SBR	100	60	2.85	1.39	6.96	2	2	3	1
SiO_2-TS90/SBR	100	60	2.70	2.78	5.57	2	2	3	1
SiO_2-TS85/SBR	100	60	2.55	4.17	4.17	2	2	3	1
SiO_2-TS80/SBR	100	60	2.40	5.57	2.78	2	2	3	1
SiO_2-TS75/SBR	100	60	2.25	6.96	1.39	2	2	3	1
SiO_2-TS70/SBR	100	60	2.10	8.35	0.00	2	2	3	1
SiO_2-TS0/SBR	100	60	0.00	0.00	9.48	2	2	3	1

For the further scale-up, the same procedure was repeated in an internal tangential rotor mixer, namely Banbury®. In this case, the vulcanization was carried out at 170 °C and 100 bar for 10 min, according to the industrial standard and the samples are labelled V10-SiO_2-TSX/SBR, where X is the TESPT/MacroSil grafting density ratio.

4.3. Results and discussion

In this paragraph, the mechanical and morphological characterization of technological NCs is reported. First, dynamic mechanical characterization is reported. The vulcanization curves of NCs are described, as well as G', G'' and tanδ obtained from oscillatory rheometry. Stress-strain curves from tensile tests are reported and commented. For the scaled-up compounds, tensile tests, hardness measurements and measurements of dynamic storage modulus E', loss modulus E'' and tan δ are presented.

The uncured rubber NCs were also tested by LAOS analysis to study the non-linear behavior of the materials at high deformations and gain additional information on the effect of the macromolecular silane on filler-matrix interactions.

Finally, the morphology of technological NCs was investigated by TEM to determine the relationship between mechanical properties and filler dispersion and distribution in the rubber matrix. Experimental details of all characterization techniques are reported in Appendix A.

4.3.1. Dynamic mechanical characterization

Vulcanization curves for the technological NCs are reported in Figure 4.2. The values of scortch time t_{s2}, minimum torque M_L, maximum torque M_H, and their difference M_H-M_L, are reported in Table 4.3.

The torque curves confirm that vulcanization for all samples was successfully achieved, and that the use of the macromolecular silane gives satisfactory M_H values. The scorch times are comparable for all samples and in line with the standard time required in the rubber industry. The torque values are consistent and in line with values expected for technological formulations. The high values of torque obtained for the reference V-SiO_2-TS0/SBR (prepared without coupling agents) are due to very high filler aggregation.

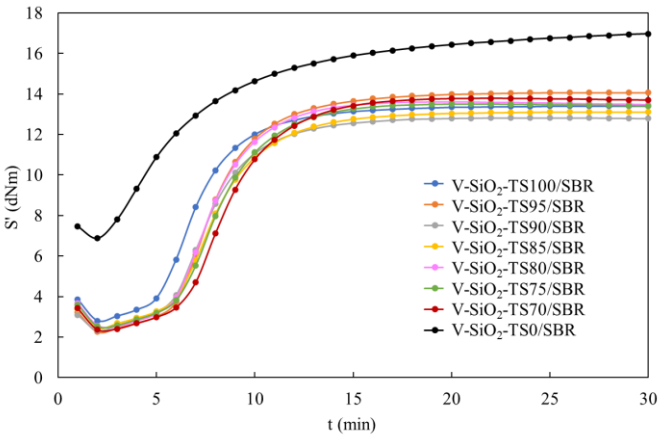

Figure 4.2 Vulcanization curves of the NC materials

Storage modulus G' *vs*. strain curves for both cured and uncured NCs are reported in Figure 4.3, while loss modulus G'' and tanδ curves are reported in Figure 4.4. The values of G' (6%), $\Delta(G'_0\text{-}G'_\infty)$ and tanδ (6%) are reported in Table 4.4. Values of G' (6%), representative of the reinforcement of the NCs, show no clear trend as the TESPT:MacroSil ratio is varied, first decreasing with increasing the amount of macromolecular silane and then increasing as more

MacroSil is added. Similarly, no trend is identified in the ΔG' (0.4%-10%), indicative of the Payne effect. The reference sample SiO_2-TS0/SBR shows the highest reinforcement but, due to poor filler dispersion, has the highest ΔG'.

Table 4.3 Curing properties of SiO_2-TSx/SBR NCs.

Sample	t_{s2} (min)	M_L (dNm)	t_{MH} (min)	M_H (dNm)	M_H-M_L (dNm)
SiO_2-TS100/SBR	6	2.80	25	13.40	10.60
SiO_2-TS95/SBR	6	2.26	25	14.07	11.81
SiO_2-TS90/SBR	6	2.32	22	12.82	10.50
SiO_2-TS85/SBR	7	2.46	25	13.11	10.65
SiO_2-TS80/SBR	6	2.57	19	13.60	11.03
SiO_2-TS75/SBR	7	2.53	20	13.51	10.98
SiO_2-TS70/SBR	7	2.37	22	13.79	11.42
SiO_2-TS0/SBR	8	6.87	30	16.97	10.10

Values of tanδ (6%), measuring the energy dissipation of SiO_2-TSX/SBR NCs over the course of deformation, suggest that increasing the amount of MacroSil over 10% of grafting density determines a reduction of hysteresis effects. The sample showing the best mechanical performance is V-SiO_2-TS75/SBR.

Overall, small amounts of macromolecular silane appear to reduce the mechanical performance of the materials in terms of reinforcement,

Payne Effect and hysteresis, while larger degrees of surface coverage produce an improvement of the dynamic mechanical properties.

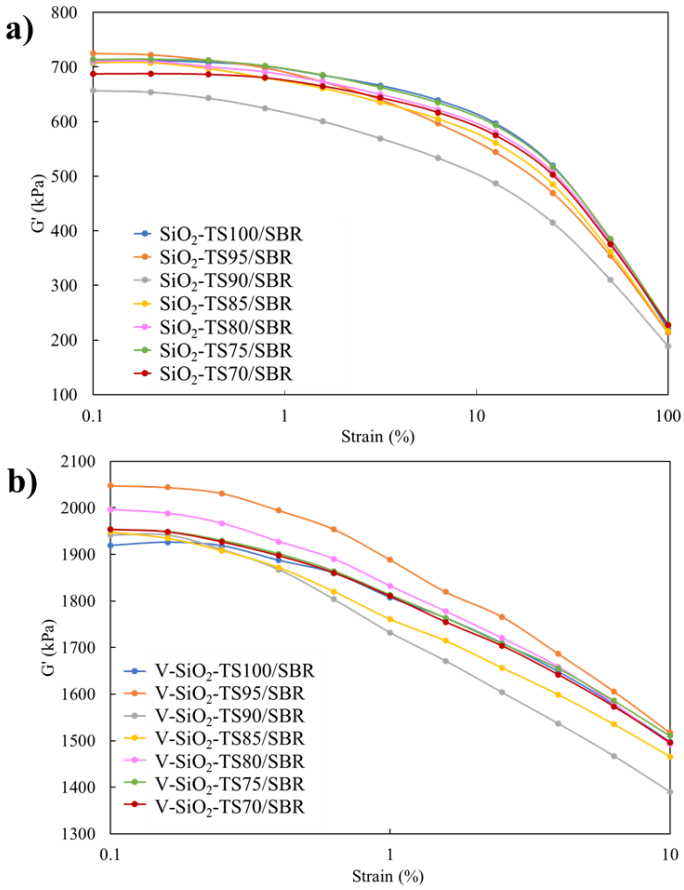

Figure 4.3 G' vs. strain for a) uncured and b) cured SiO_2-TSX/SBR NCs. The reference SiO_2-TS0/SBR was excluded for scale.

Table 4.4 Values of G' (6%), ΔG' (0.4%-10%) and tanδ (6%) for SiO_2-TSX/SBR NCs.

Sample	G' (6%) (kPa)	ΔG' (0.4%-10%) (kPa)	tanδ (6%)
V-SiO_2-TS100/SBR	1577.55	389.49	0.168
V-SiO_2-TS95/SBR	1605.99	477.02	0.166
V-SiO_2-TS90/SBR	1467.00	477.27	0.179
V-SiO_2-TS85/SBR	1535.09	406.01	0.171
V-SiO_2-TS80/SBR	1579.60	434.12	0.164
V-SiO_2-TS75/SBR	1585.85	390.17	0.163
V- SiO_2-TS70/SBR	1573.27	400.97	0.159
V-SiO_2-TS0/SBR	2507.65	1508.18	0.206

4.3.2. Tensile tests

A selection of V-SiO_2-TSX/SBR NCs were further analyzed by tensile testing. Stress-strain curves of the materials, acquired at a constant temperature of 23 °C, are reported in Figure 4.5, while values of stress at break S_B and elongation at break E_B are reported in Table 4.5. For each NC sample, three different specimens were tested. The reported curves are representative of the three measurements, while the values of stress and elongation at break are the average of three measurements.

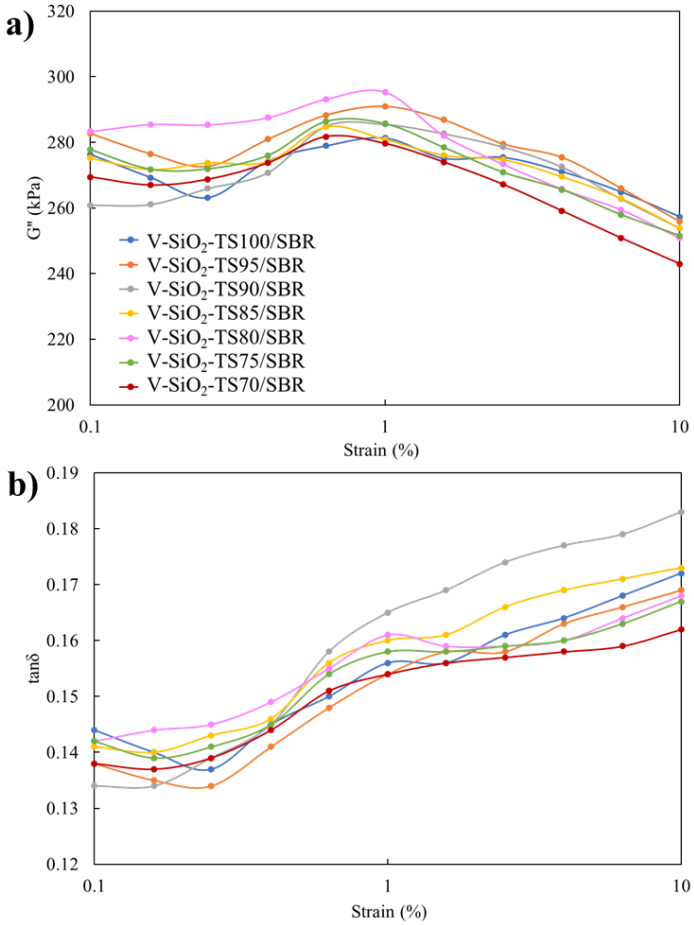

Figure 4.4 a) Loss modulus G'' and b) tanδ vs. strain of the cured NCs. The reference SiO_2-TS0/SBR was excluded for scale.

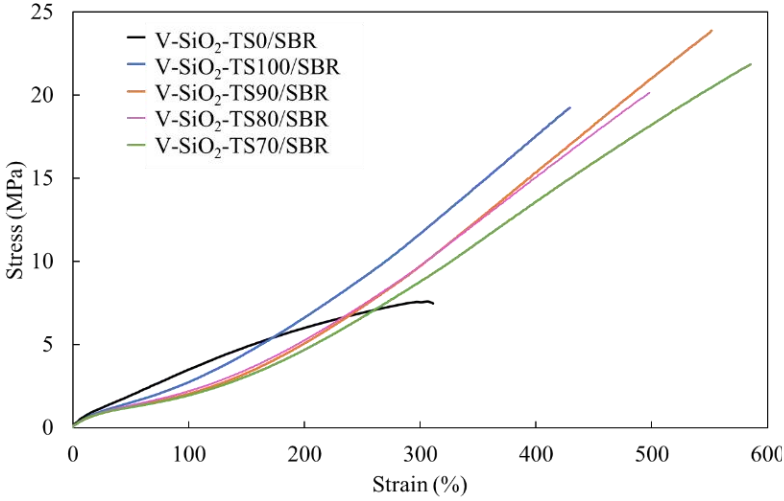

Figure 4.5 Stress-strain curves of technological V-SiO_2-TSX/SBR NCs.

Table 4.5 Values of elongation at break and stress at break for the technological NCs obtained by tensile testing.

Sample	E_B (%)	S_B (MPa)
V-SiO_2-TS0/SBR	320±40	7.3±0.2
V-SiO_2-TS100/SBR	437±6	19.7±0.5
V-SiO_2-TS90/SBR	544±8	23.5±0.5
V-SiO_2-TS80/SBR	540±40	23±2
V-SiO_2-TS70/SBR	590±50	22±3

The V-SiO_2-TS0/SBR reference sample shows very low elongation at break and stress at break. Interestingly, the values of both elongation and stress at break appear to increase as the amount of MacroSil macromolecular silane in the system is increased. The sample with the highest values of elongation is V-SiO_2-TS70/SBR, with the highest degree of MacroSil surface coverage, showing an elongation of 590±50% upon breaking and a stress at break value of 22±3 MPa.

These results suggest that the addition of the macromolecular silane improves the filler-rubber interaction with respect to the short-chain silane, thus producing NCs with improved rigidity.

4.3.3. Mechanical characterization of the scaled-up NCs

Vulcanization parameters for the scaled-up composites are reported in Table 4.6. Parameter *tx* indicates the time (in minutes) at which the torque S' has reached x% of the maximum value M_H. *%Ret* is the percentage of reversion, indicating the decrease of torque after the maximum value was reached. These results suggest that 90% of the vulcanization process was completed in approximately 10 minutes, while %Ret is negligible. For this reason, the scaled-up composites V10-SiO_2-TSX/SBR are comparable to the V-SiO_2-TSX/SBR analyzed in the previous paragraph.

Scaled-up composites were tested by Internal Rubber Hardness Degree (IRHD) measurements both at room temperature and at 100 °C. The resulting hardness values, dynamic elastic moduli E', E'' and loss tangent tanδ measured at 70 °C, 10 Hz and 5.0% of strain are reported in Table 4.7.

The results indicate a slight but non-negligible increase in hardness following the addition of MacroSil. Similarly, values of dynamic storage modulus E' indicate an increase in reinforcement as the amount of MacroSil is increased.

Table 4.6 Vulcanization parameters for the scaled-up NCs. t30-100 the time required to reach 30-100% of M_H and %Ret the reversion percentage.

Sample	M_L (dNm)	M_H (dNm)	t_{s2} (min)	t30 (min)	t90 (min)	t100 (min)	%Ret (%)
V10-SiO_2-TS100/SBR	1.99	15.47	3.84	5.71	9.50	18.92	0.07
V10-SiO_2-TS90/SBR	2.28	17.17	2.98	5.22	8.87	18.81	0.07
V10-SiO_2-TS80/SBR	2.13	17.31	2.54	5.17	8.77	18.27	0.07
V10-SiO_2-TS70/SBR	2.40	16.77	3.46	5.36	8.96	17.81	0.14

Table 4.7 Values of IRHD and E', E'' and tanδ measured at 70 °C and 5.0% of strain for V10-SiO_2-TSX/SBR samples.

Sample	IRHD (r.t.)	IRHD (100 °C)	E' (MPa)	E'' (MPa)	tanδ
V10-SiO_2-TS100/SBR	63.00	59.30	3.75	0.94	0.25
V10-SiO_2-TS90/SBR	66.20	61.30	4.70	1.05	0.22
V10-SiO_2-TS80/SBR	67.70	62.20	4.76	0.96	0.20
V10-SiO_2-TS70/SBR	65.40	60.30	4.91	1.01	0.21

The V10-SiO_2-TSX/SBR composites were further characterized by tensile tests and the resulting values of stress S at 10, 50, 100 and 300% of elongation, as well as values of S_B and E_B, are reported in Table 4.8. Interestingly, these results suggest an improvement of both

S_B and E_B, confirming the results previously observed for the small-scale composites.

Comparing these results with hardness measurements and dynamic elastic moduli suggests that the addition of the macromolecular silane promotes both the reinforcement and the elongability of the NCs. Furthermore, it is important to note that the presence of additional sulfur in high-TESPT NCs was not compensated upon substitution with MacroSil. This might account for the non-monotonic behavior of hardness and elastic moduli.

Table 4.8 Values of stress at different degrees of elongation, S_B and E_B for V10-SiO_2-TSX/SBR samples.

Sample	S(10%) MPa	S(50%) MPa	S(100%) MPa	S(300%) MPa	S_B MPa	E_B %
V10-SiO_2-TS100/SBR	0.54	1.41	2.37	9.65	10.36	299.75
V10-SiO_2-TS90/SBR	0.60	1.44	2.29	9.12	11.59	371.67
V10-SiO_2-TS80/SBR	0.60	1.42	2.23	9.12	13.21	412.73
V10-SiO_2-TS70/SBR	0.58	1.34	2.07	8.46	12.29	408.95

4.3.4. Large amplitude oscillatory shear (LAOS) analysis

4.3.4.1. Basic introduction to the theory of LAOS

In conventional dynamic oscillatory shear tests, the tested material undergoes a sinusoidal deformation, and the response of the material

is measured as a function of time, producing two distinct regimes: the linear regime and the non-linear regime.

In the linear regime, the tested material undergoes small deformations and is therefore in the SAOS (Small Amplitude Oscillatory Shear) regime. Conversely, when the material is deformed beyond a certain threshold, the material is in the LAOS range.

In the SAOS regime, G' and G'' at a fixed frequency ω are both independent of strain amplitude. The oscillatory stress response of the material to a sinusoidal applied strain is also sinusoidal, as shown in Figure 4.6. In the LAOS regime, G' and G'' are dependent on strain amplitude, and the stress response of the material is no longer a sinusoidal function.[4,5]

The aim of LAOS analysis is to determine the nonlinear stress response to gain additional information on the nonlinear behavior of the tested materials. In fact, although linear oscillatory shear analysis can provide useful information, the theory is valid only at small deformations. In most applications, NCs may undergo large and rapid deformations. In general, the study of filled rubber NCs depends on the understanding of nonlinear mechanical properties, namely the Payne effect.[6] LAOS can provide more insight to correlate the microstructural differences of the tested materials, such as filler aggregation, distribution and self-assembly, with their mechanical behavior.

In oscillatory shear tests, samples are measured in a biconical chamber. This ensures that during the deformation, the strain $\gamma(t)$ is constant in every point of the specimen. Thus, the shape of the chamber ensures homogeneous shear strain and strain history on the whole specimen. Similarly, the shear stress $\tau(t)$ is the same everywhere. The applied shear strain is sinusoidal, and it is given by Equation 4.2.

$$\gamma(t) = \gamma_0 \sin(\omega t) \tag{4.2}$$

The response measured by the instrument is the torque S(t), which is related to the stress τ(t) by the simple relation given in Equation 4.3.

$$\tau = \frac{3S}{2\pi R^3} \tag{4.3}$$

where R is the radius of the specimen chamber.

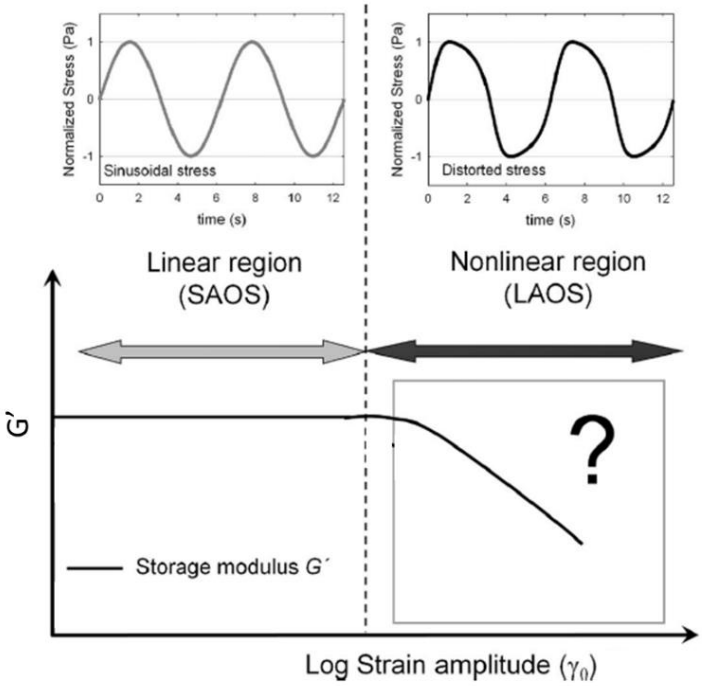

Figure 4.6 Schematic representation of the stress and G' response in the linear SAOS region and non-linear LAOS region. Adapted from Hyun *et al.*.[4]

In the case of a linear response, the stress response will be sinusoidal, expressed by another sinusoidal function with a phase difference δ, $\tau(t) = \tau_0 \sin(\omega t + \delta)$.[7] In LAOS, the stress function $\tau(t)$ has a distorted shape; in this case, τ(t) is not given explicitly, but a Fourier transform (FT) approach is required. The Fourier coefficients τ'_k, τ''_k up to the 9th harmonic are measured (Equation 4.4).

$$\tau(t) = \sum_k \tau'_k \cdot sin(k\omega t) + \sum_k \tau''_k \cdot cos(k\omega t) \tag{4.4}$$

From this equation, the normalized stress G(t) can be obtained, which in turn can be split into $G'_k(t)$ and $G''_k(t)$, the non-linear elastic and viscous terms, as shown in Equation 4.5.

$$\begin{aligned} G(t) = \tau(t)/\gamma_0 = &\sum_k G'_k \cdot \sin(k\omega t) \\ &+ \sum_k G''_k \cdot \cos(k\omega t) \end{aligned} \tag{4.5}$$

It is worth noting that only coefficients of the odd harmonics are non-zero, due to the symmetry of the deformation. The coefficients G'_k are usually normalized by the first harmonic and indicated as $I_{k/1}$ (Equation 4.6):[5,5]

$$I_{k/1} = G'_k / G'_1 \tag{4.6}$$

Typically, the $I_{3/1}$ parameter, *i.e.* the normalized intensity of the third harmonic, has the highest values, therefore has the largest influence on the non-linear behavior of the material.

4.3.4.2. LAOS of filled rubber: interpretation approaches

Due to its versatility in the analysis of the non-linear response of materials, LAOS was applied to the study of filled rubber NCs. Different interpretation approaches were emerged, proposing a correlation between the LAOS response and the microstructure of materials.

Schwab, Wilhelm *et al.*[5] studied the effect of filler on LAOS in carbon black (CB) filled rubber. SBR/CB NCs were tested with different kinds of CB and at different volume ratio of filler without the addition of coupling agents. They found that the effect of the filler was maximized when the parameter $I_{3/1}$ was measured at a strain γ_0=32%. Increasing the volume ratio of filler induced an increase in $I_{3/1}$, corresponding to an increase of nonlinear effects which was attributed to the breakdown of CB aggregates.

Following this approach, Nie and co-workers[8] studied the effect of silanization on SiO_2-filled rubber NCs. Rubber NCs with 50 phr of SiO_2 and different amounts of 3,3′-tetrathiobis(propyltriethoxysilane) (Si-69), ranging from 0 phr to 5.6 phr, were analyzed. In this study, the $I_{3/1}$ parameter at γ_0=32% obtained from LAOS of the uncured composites was evaluated, highliting a good correlation with the Payne effect measured for the cured composites with conventional SAOS analysis (Figure 4.7). The conclusion was that $I_{3/1}$(32%) decreased with the silane amount due to a reduction of nonlinearity.

An alternative approach was proposed by Leblanc et *al.*, who studied both unfilled,[9] SiO_2-[10] and CB-filled[11,12] rubber compounds by a LAOS FT-rheology approach. For unfilled rubber, the normalized intensity of the third harmonic $I_{3/1}$ is a sigmoid curve with asymptotic behavior at high strain. Conversely, filled rubbers show a «bump»

resulting from the superposition of two contributions: the unfilled polymer and the strain-sensitive filler network (Figure 4.8).

Recently, Pole and Isayev[13] studied SiO_2-filled star-shaped SBR NCs with LAOS. They measured the effect of SiO_2 with different surface areas on the nonlinear rheological properties of the materials. In addition to the approach proposed by Leblanc,[14] they also examined the Lissajous figures, closed loop plots of stress *vs*. strain.

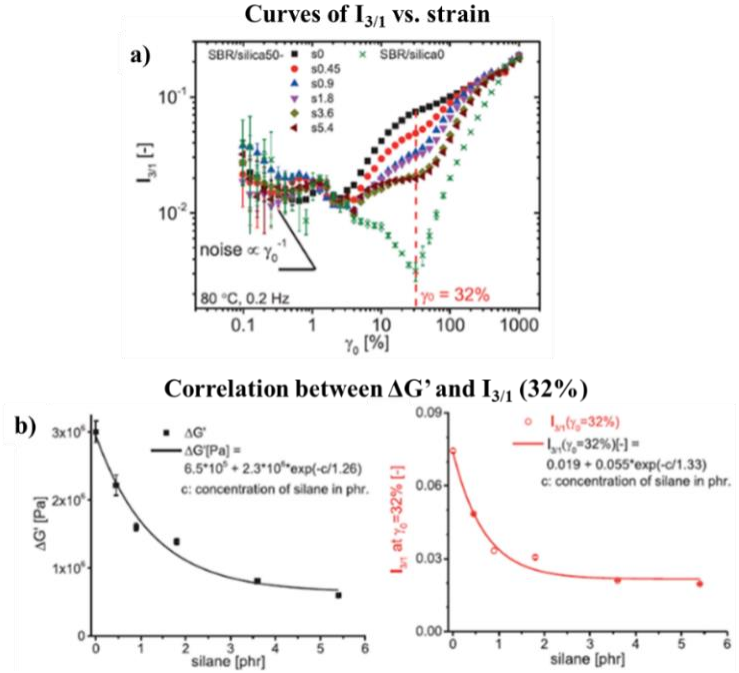

Figure 4.7 a) Curves of $I_{3/1}$ *vs.* strain obtained from LAOS showing the γ_0=32% threshold and b) correlation between Payne effect and $I_{3/1}$ parameter. Samples are labelled *sX*, where *X* is the amount of silane in phr. Adapted from Nie *et al*.[8]

These plots are a visual demonstration of the effect of higher harmonic contributions, especially the 3rd harmonic, on the rheological behavior of the material.[4] Increasing the surface area of SiO_2 increased the NCs nonlinear response, producing more distorted Lissajous figures. Examples of typical Lissajous plots for different types of materials are reported in Figure 4.9.[15]

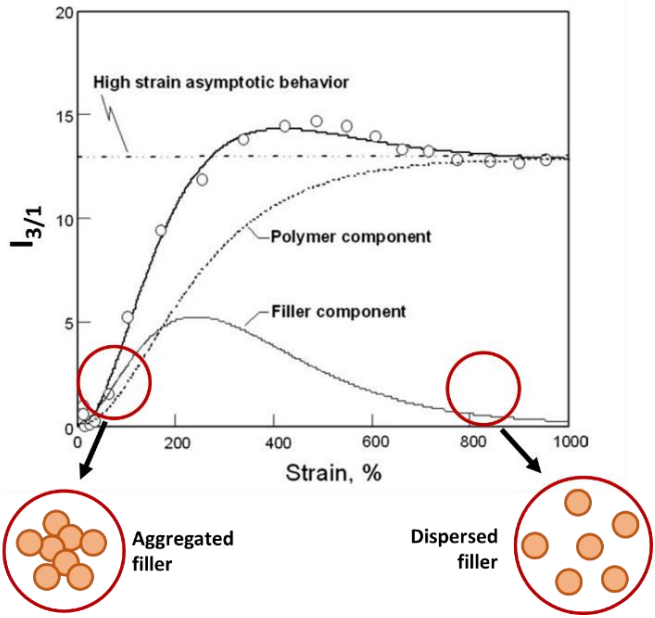

Figure 4.8 Polymer and filler contributions to the $I_{3/1}$ *vs.* strain curve obtained from LAOS of filled rubber. Adapted from Leblanc *et al.*[11]

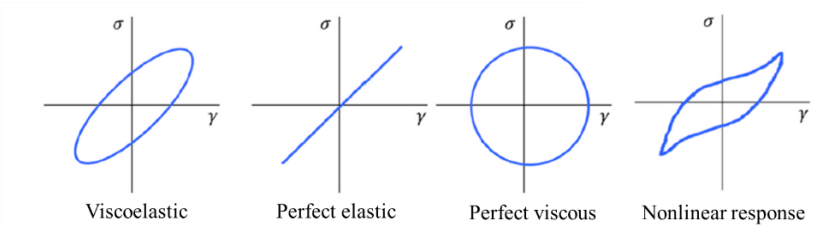

Figure 4.9 Lissajous figures for different types of rheological response. Adapted from Schreuders et al.[15]

4.3.4.3. Results and discussion on LAOS of SiO_2-TSX/SBR NCs

The curves of the normalized intensity of the third harmonic $I_{3/1}$ *vs.* strain for SiO2-TSX/SBR NCs based on LAOS approach are reported in Figure 4.10. All samples exhibit the "bump" at high strain at around 400%, except for the SiO_2-TS0/SBR reference sample, which shows an inflection at lower strain. This behavior is associated with the breakdown of filler aggregates due to very poor dispersion. Following the model proposed by Leblanc,[11] the sample with no macromolecular silane, namely SiO_2-TS100/SBR, shows the most pronounced effect of filler aggregation. As the amount of macromolecular silane is increased, the curves become closer to a sigmoid shape, suggesting an improvement of filler/polymer interaction.

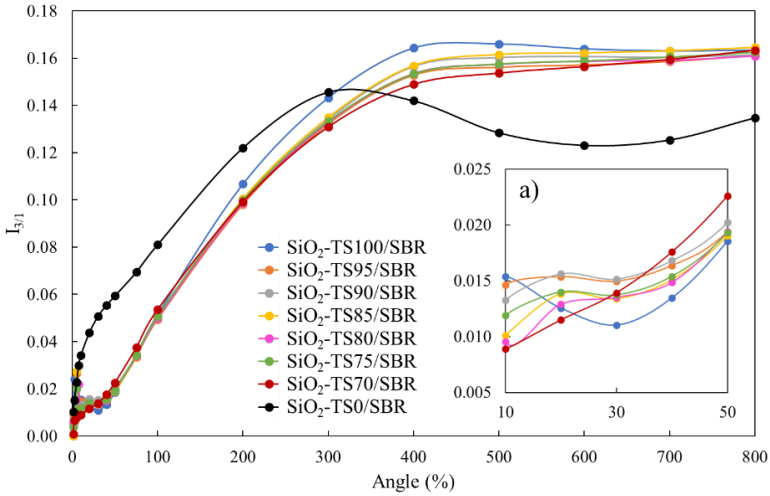

Figure 4.10 Plot of the normalized intensity of $I_{3/1}$ vs. strain for SiO_2-TSX/SBR NCs. Inset a) shows the enlargement of the plot around the 30% threshold.

The $I_{3/1}$ curves were also analyzed with the approach of Nie *et al.*[5] (a in Figure 4.10). The values of $I_{3/1}$ (30%) are reported in Table 4.9. Interestingly, all samples exhibit a minimum of $I_{3/1}$ at 30% strain except SiO_2-TS70/SBR, while the sample with the lowest $I_{3/1}$ (30%) is the NC with only TESPT. However, no clear trend in these values can be established, suggesting that this interpretation of LAOS curves is not suitable for the analyzed system.

Finally, Lissajous patterns of a selection of samples were plotted and compared, as shown in Figure 4.11. Based on the $I_{3/1}$ *vs.* strain plot, the selected strain amplitude was 400% to highlight filler effects.

Table 4.9 Values of $I_{3/1}$ based on LAOS analysis for SiO_2-TSX/SBR NCs measured at 30% of strain.

Sample	$I_{3/1}$ (30%)
SiO_2-TS100/SBR	0.0111
SiO_2-TS95/SBR	0.0150
SiO_2-TS90/SBR	0.0152
SiO_2-TS85/SBR	0.0134
SiO_2-TS80/SBR	0.0135
SiO_2-TS75/SBR	0.0137
SiO_2-TS70/SBR	0.0139
SiO_2-TS0/SBR	0.0506

All samples show a deviation from the elliptical shape expected for the linear viscoelastic behavior. Interestingly, as the amount of macromolecular silane is increased, the shape of the Lissajous figure gradually changes, becoming less elongated.

This clear trend suggests that the LAOS properties of the NCs are related to a microstructural change of filler distribution induced by the addition of the macromolecular silane.

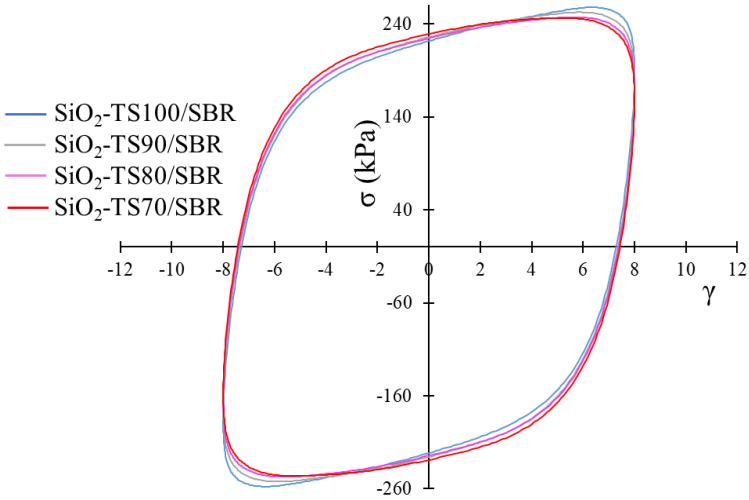

Figure 4.11 Lissajous figures of a selection of NCs showing the plot of stress σ vs. strain γ at a strain amplitude of 400%, obtained from LAOS analysis.

4.3.4.4. Morphological characterization

Morphological characterization of V10-SiO_2-TSX/SBR NCs was performed by TEM analysis. TEM micrographs of a selection of the samples are reported in Figure 4.12. Increasing the degree of surface coverage with the macromolecular silane shows an improvement of filler dispersion, a decrease in the size of NPs aggregates and the formation of a more extended filler network.

This morphological transition may be correlated to the self-organization effects observed in the ex-situ rubber NCs prepared with SiO_2 HNPs (see Paragraph 3.3.2 of Chapter 3). The formation of self-organized aggregates induces an increase of the amount of rigid

enclosed rubber, thus improving the mechanical properties of the materials, as reported before.[16,17]

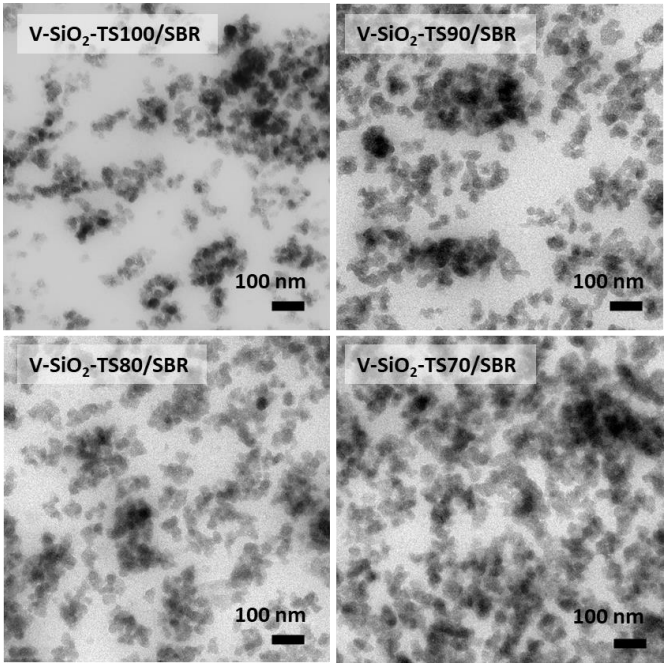

Figure 4.12 TEM micrographs of the V10-SiO_2-TSX/SBR NCs with increasing degree of macromolecular silane surface coverage.

4.4. Bibliography

1 L. Xia, C. Li, X. Zhang, J. Wang, H. Wu and S. Guo, *Polymer (Guildf).*, 2018, **141**, 70–78.

2 L. Tadiello, M. D'Arienzo, B. Di Credico, T. Hanel, L. Matejka, M. Mauri, F. Morazzoni, R. Simonutti, M. Spirkova and R. Scotti, *Soft Matter*, 2015, **11**, 4022–4033.

3 A. Susanna, L. Armelao, E. Callone, S. Dirè, M. D'Arienzo, B. Di Credico, L. Giannini, T. Hanel, F. Morazzoni and R. Scotti, *Chem.*

Eng. J., 2015, **275**, 245–252.

4 K. Hyun, M. Wilhelm, C. O. Klein, K. S. Cho, J. G. Nam, K. H. Ahn, S. J. Lee, R. H. Ewoldt and G. H. McKinley, *Prog. Polym. Sci.*, 2011, **36**, 1697–1753.

5 L. Schwab, N. Hojdis, J. Lacayo and M. Wilhelm, *Macromol. Mater. Eng.*, 2016, **301**, 457–468.

6 A. R. Payne, *J. Appl. Polym. Sci.*, 1962, **6**, 368–372.

7 R. Lakes, *Viscoelastic materials*, Cambridge University Press, New York, 2009.

8 S. Nie, J. Lacayo-Pineda and M. Wilhelm, *Soft Mater.*, 2019, **17**, 269–282.

9 J. L. Leblanc, *J. Appl. Polym. Sci.*, 2005, **95**, 90–106.

10 J. L. Leblanc and G. Nijman, *J. Appl. Polym. Sci.*, 2009, **112**, 1128–1141.

11 J. L. Leblanc, *J. Appl. Polym. Sci.*, 2012, **126**, 408–422.

12 J. L. Leblanc, *Rubber Chem. Technol.*, 2005, **78**, 54–75.

13 S. S. Pole and A. I. Isayev, *J. Appl. Polym. Sci.*, , DOI:10.1002/app.50660.

14 C. Perge, N. Taberlet, T. Gibaud and S. Manneville, *J. Rheol. (N. Y. N. Y).*, 2014, **58**, 1331–1357.

15 F. K. G. Schreuders, L. M. C. Sagis, I. Bodnár, P. Erni, R. M. Boom and A. J. van der Goot, *Food Hydrocoll.*, 2021, **110**, 106172.

16 E. Cobani, I. Tagliaro, M. Geppi, L. Giannini, P. Leclère, F. Martini, T. C. Nguyen, R. Lazzaroni, R. Scotti, L. Tadiello and B. Di Credico, *Nanomaterials*, 2019, **9**, 486.

17 R. Scotti, L. Conzatti, M. D'Arienzo, B. Di Credico, L. Giannini, T. Hanel, P. Stagnaro, A. Susanna, L. Tadiello and F. Morazzoni, *Polymer (Guildf).*, 2014, **55**, 1497–1506.

Chapter 5.

In-depth study of HNPs self-assembly

5.1. Overview

Understanding the forces that determine the self-organization of HNPs is crucial to control the distribution of particles in PNCs at the local scale. To this end, several studies have investigated the self-assembly of HNPs by following a variety of theoretical approaches combined with experimental data.[1–6] These demonstrate that the self-assembly of HNPs is strongly dependent on polymer grafting density, and that the self-organization of spherical nano-objects in anisotropic structures results from a balance of attractive and repulsive forces arising from the interaction of the polymer shells.

Theoretical models on HNPs self-assembly have mainly focused on NPs having PS shells due to the large availability of experimental data. To our knowledge, no theoretical study of the self-assembly of PB-grafted SiO_2 HNPs has been performed so far. This chapter reports more-in depth understanding on PB-grafted SiO_2 HNPs thanks to a combination of SAXS analysis and theoretical calculations.

SAXS analysis of bare SiO_2 NPs and PB-functionalized SiO_2 HNPs allowed to determine critical parameters for the theoretical model, in collaboration with Prof. Simone Mascotto and of Dr. Andreas Meyer from Hamburg University.

Snapshots resulting from Monte Carlo simulations of HNPs dispersions in THF were compared to experimental data resulting from TEM analysis (Chapter 2) to provide a theoretical framework for the observed self-assembly behavior. This investigation was performed in collaboration with Prof. Arturo Moncho of the University of Granada and Prof. Gerardo Odriozola of Universidad Autónoma Metropolitana-Azcapotzalco (UAM, Mexico City).

5.2. SAXS analysis of SiO_2 HNPs dispersions

Characterization is crucial for synthesizing HNPs with specific molecular parameters, revealing their structures, understanding their behavior and properties, and using them in specific applications. The HNPs structures, behavior, and properties are fundamentally governed by molecular weights, dispersity, grafting density, polymer topology, size and geometry of core NPs, etc. Accurate characterization of basic defining parameters and other aspects of HNPs requires the use of a broad range of characterization techniques.

By DLS, the hydrodynamic size of HNPs in a good solvent, can be measured, but is usually much larger than that of core NPs because of the swelling of polymer brushes and the polydispersity of grafted chains. The characterization of sparsely grafted HNPs with conventional methods such as DLS is often difficult due to sample aggregation issues. In fact, it is challenging to achieve a perfect dispersion of HNPs in any solvent due to the coexistence of attractive and repulsive interactions, as discussed below in Paragraph 5.3. Electron microscopy, on the other hand, can only provide information on the behavior of HNPs in the dry state.

Because of this, SAXS analysis can be a useful tool for the investigation of the HNPs behavior in solution, from the precise evaluation of structural parameters (core radius, polymer shell thickness) to the study of self-assembly.[3,7,8]

To investigate the PB-grafted SiO_2-HNPs, THF was selected as the solvent due to the high solubility of PB and good dispersion of both bare and functionalized SiO_2.

5.2.1. Sample preparation

Bare SiO_2-ST and SiO_2-HNP_X, where X = 5, 8, 11 is the weight percentage of PB polymer coating, were prepared according to the

procedure described in Chapter 2. Different degrees of surface coating are due to increased functionalization yields resulting from the replication of the synthesis on a smaller scale.

Dispersions of SiO_2-ST and SiO_2-HNP_X in THF were prepared by suspending 5 wt% of SiO_2 cores in THF by ultrasonication for 1 h.

5.2.2. Results and discussion

SAXS curves of SiO_2-ST and SiO_2-HNP_X suspensions in THF are reported in Figure 5.1. All samples show the typical oscillation of spherical NPs. Peaks are sharper in SiO_2-ST due to the increased polydispersity and loss of spherical shape in the case of SiO_2-HNPs.

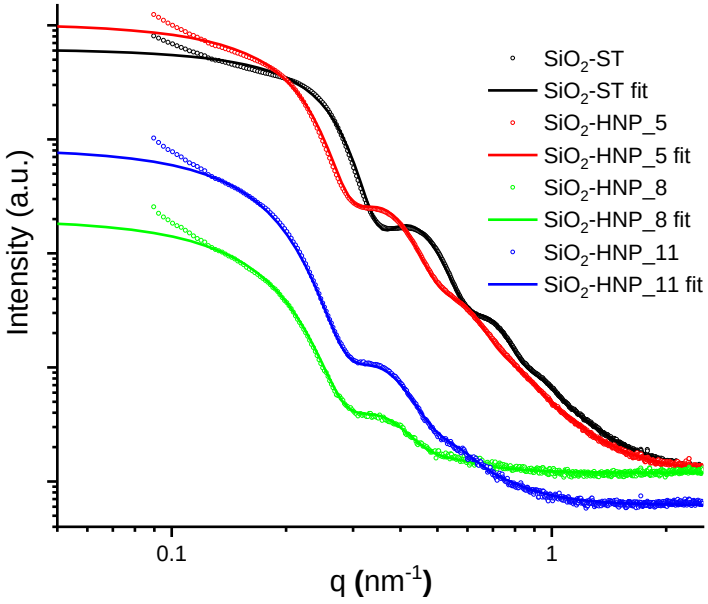

Figure 5.1 SAXS curves and fitting of bare SiO_2-ST and SiO_2-HNP_X.

The slope of the SAXS curve at low q values suggests the presence of aggregation or the formation of assemblies. Due to the large size of the NPs, additional information on the morphology of aggregates requires access to lower q values which can only be provided by synchrotron experiments (data not reported).

The values of radius and standard deviation for the samples are reported in Table 5.1. The radius as well as the standard deviation increase as surface coverage is increased because of the polymer shell. The values confirm the experimental data from TEM, DLS and SAXS analysis on dry powders discussed above in Chapter 2. Interestingly, the radius of HNPs increases more rapidly from SiO_2-HNP_5 to SiO_2-HNP_8 than from SiO_2-HNP_8 to SiO_2-HNP_11, suggesting that after a certain grafting density, saturation of the surface is reached.

Table 5.1 Radius and standard deviation values for SiO_2-ST and SiO_2-HNP_X samples.

Sample	Radius (nm)	St. Dev. (%)
SiO_2-ST	13.5	11.3
SiO_2-HNP_5	16.1	12.8
SiO_2-HNP_8	16.6	14.0
SiO_2-HNP_11	16.7	14.1

The thickness δ of the polymer shell in THF, required for the theoretical calculations, as illustrated in Paragraph 5.3, was obtained by subtracting the radius of bare SiO_2-ST to the radius of SiO_2-HNP_X. From these data, the average value of $\delta = 3.0$ nm is obtained.

5.3. Theoretical model of SiO_2 HNPs interactions

The self-assembly behavior of PB-grafted SiO_2 HNPs in tetrahydrofuran (THF) is explained by means of a theoretical model, starting from experimental evidence reported in this Thesis. These support that:

i) SiO_2-ST aggregate forming clusters of particles;

ii) SiO_2 HNPs are uncharged;

iii) if the particles are covered with PB chains, HNPs self-assemble to form anisotropic domains increasing concentration of grafted polymer.

As discussed in Chapter 1, there are several possibilities to produce anisotropic self-assembly of NPs. The possible explanations for the observed self-assembly behavior of HNPs are the following.

i) The coverage at the top of the silica particle is not uniform. That is, the grafted chains are concentrated into certain regions or patches. This kind of non-uniform distribution of polymer coils will lead to the formation of asymmetric structures due to directional interactions. However, in our case, the experimental results show that the particle coverage is uniform in all cases, so the formation of chains cannot be justified in this way.

ii) The particles possess anisotropic shapes. For instance, if the nanoparticles are cube-shaped, the aggregation will mainly occur on the faces of the particles, which in turn will lead to anisotropic clusters. Depletion effects lead to the assembly of NRs and nanofibers. In this case, however, SiO_2 NPs are spherical.

iii) Existence of flow or other non-equilibrium effects. However, HNPs assemblies are formed in equilibrium conditions (static self-assembly).

iv) The surface coverage is uniform, but the particle interactions are affected by three body contributions. Three-body interactions reflect the fact that the interaction between two neighboring particles is affected by the presence of a third particle. This is the case of HNPs discussed in this Chapter.

Indeed, previous computer simulations and experiments of spherical NPs uniformly grafted with polymer chains have recently been shown to assemble into anisotropic phases like strings and sheets.[1,9,10] The resulting three-body contribution is found to be highly repulsive and anisotropic with the degree of repulsion rising with increasing angular deviation from the dimer axis.

This effect can be explained in terms of free energy. Indeed, the free energy is determined by a competition between favorable enthalpic energy gained by forming contacts between NPs and the entropic cost associated with compressing the polymer grafts to form such contacts. When two particles covered by long polymer brushes aggregate, a redistribution of the polymer chains occurs, resulting in an increase of polymer concentration outside the contact region. This density increase makes the 'dimer' more protected against aggregation with another particle, with it being most susceptible to aggregation with another particle at the point diametrically opposite to the first contact point.

This effect is illustrated in Figure 5.2. On the left, a dimer formed by the aggregation of two HNPs is shown. When the dimer is created, the enthalpic (attractive) energy must overcome the entropic and elastic repulsion exerted by the compressed polymer shells in the region between both particles, where both polymer shells overlap. The resulting dimer has a region where the polymer concentration is larger (dark gray region).

On the right panel of Figure 5.2, a third HNP approaches the dimer. If this particle approaches the dimer following direction A, it will experience and enhanced steric repulsion induced by the already compressed polymer layers of the dimer. This repulsion goes beyond the pairwise additive interaction: it arises from a three-body contribution. However, if the third particle tries to aggregate in the opposite corner (following direction B), the three-body repulsion will be negligible. Therefore, this mechanism favors the assembly of HNPs into linear structures, such as chains.

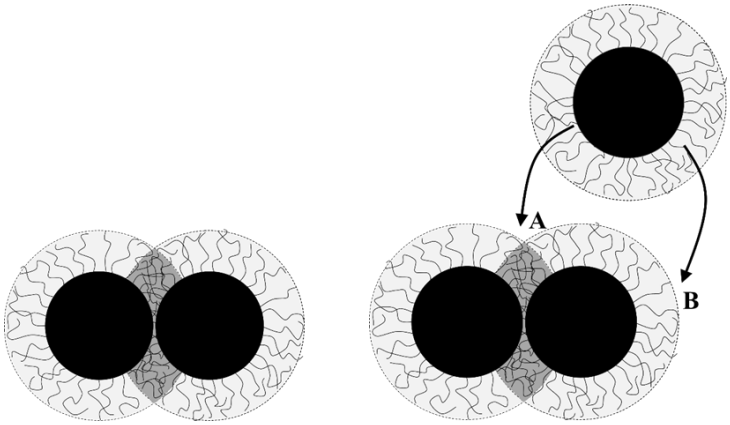

Figure 5.2 On the left, interaction of two HNPs forming a dimer. On the right, schematic representation of a three-body interaction of HNPs. The third particle preferentially aggregates in region B. The darker grey region indicates higher PB concentration.

5.3.1. Theory

A simplified coarse-grained model for particle interactions between HNPs is now discussed. If the system has *N* particles, the total

interaction potential up to third order contribution is given by Equation 5.1.

$$U_T(\mathbf{r}_1,\ldots\mathbf{r}_N) = \sum_{j>i=1}^{N} U_2(r_{ij}) + \sum_{k>j>i=1}^{N} U_3(r_{ij}, r_{ik}, r_{jk}) \qquad (5.1)$$

Where $U_2(r_{ij})$ indicates the pairwise additive particle-particle interactions and $U_3(r_{ij},r_{ik},r_{jk})$ is the three-body interaction term. For spherical HNPs uniformly grafted with polymer chains, U_2 only depends on the interparticle distance. The three-body energetic contribution depends on the distance and orientation of the three particles, so it represents a more complex interaction term. In the following we propose an analytical model for these particle interactions. For this purpose, we split the analysis considering two situations, namely uncoated NPs and coated HNPs.

5.3.1.1. Uncoated SiO_2 NPs

Here, we suppose that the silica beads are not covered by any grafted polymer (see Figure 5.3).

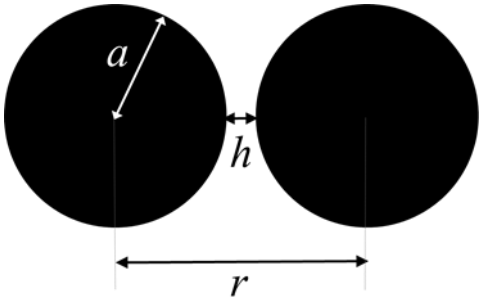

Figure 5.3 Scheme of two SiO_2-ST NPs.

In this particular case, three-body interaction in Equation 5.1 is zero ($U_3 = 0$). In addition, since the particles are uncharged, the only interaction between a pair of particles is the van der Waals potential, given by Equation 5.2.

$$U_2(r) = U_{vdW}(r) = \begin{cases} \infty & r < r_0 \\ -\frac{A_H}{12}\left[\frac{(2a)^2}{r^2} + \frac{(2a)^2}{r^2-(2a)^2} + 2\ln\left(\frac{r^2-(2a)^2}{r^2}\right)\right] & r \geq r_0 \end{cases} \quad (5.2)$$

Where a is the NPs radius, the short-range distance r_0 represents the distance of maximum approximation between particle surfaces, which is given by the surface roughness, of about $r_0 = 0.1$ nm, and A_H is the Hamaker constant of silica immersed in THF. Its value can be determined from Equation 5.3.

$$A_H = A_{212} \simeq \left(\sqrt{A_{22}} - \sqrt{A_{11}}\right)^2 \quad (5.3)$$

where A_{11} is the Hamaker constant of THF in vacuum, and A_{22} is the Hamaker constant of silica in vacuum. From physical-chemistry handbooks, we know that $A_{22} = 8.53\times10^{-20}$ J. A_{11} can be determined from the expression reported in Equation 5.4.

$$A_{11} = \gamma_{LW} 32\pi l_0^2 \quad (5.4)$$

Where γ_{LW} is the surface tension of THF, given by $\gamma_{LW} = 27.4$ mJ/m^2, and $l_0 = 1.36\times10^{-10}$ m, which leads to $A_{11} = 5.095\times10^{-20}$ J. Therefore, the value of the Hamaker constant of SiO_2 in THF is reported in Equation 5.5:

$$A_H = 4.402\times10^{-21} \text{ J} \quad (5.5)$$

Normalizing by the thermal energy (k_BT), with T=298 K we find the value in Equation 5.6.

$$A_H / k_BT = \beta A_H = 1.07 \tag{5.5}$$

The resulting interaction potential is depicted in Figure 5.4**.**

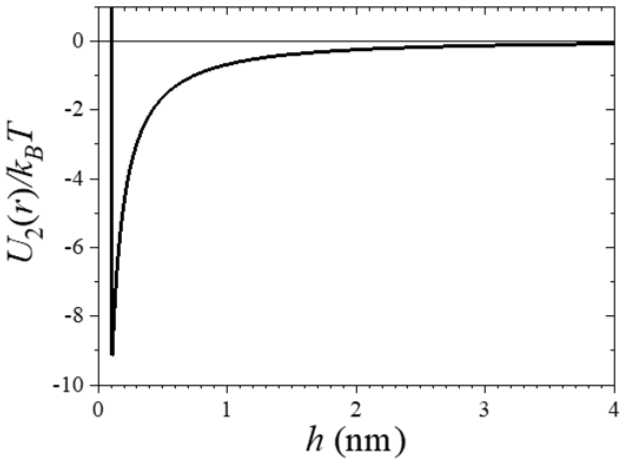

Figure 5.4 Van der Waals attractive interaction between two SiO_2-ST NPs as a function of the surface-surface separation, h. The interaction is normalized by the thermal energy, k_BT.

The van der Waals force is attractive and reaches the minimum value A_{vdW} = –9.12 times the thermal energy. In order to quantify the total amount of attraction, we calculate the normalized second virial coefficient of this pair potential, defined as (Equation 5.6):

$$B_2^* = -\frac{3}{\sigma^3}\int_0^\infty (e^{-\beta U_2(r)} - 1) r^2 dr \tag{5.6}$$

If $B_2^* < -1.5$, the attraction is usually strong enough to phase separate the system in stable aggregates. In this particular case, the van der Waals attraction leads to $B_2^* = -24.21$, which implies a large amount of attraction that is able to join together particles to create stable clusters.

It is important to remark that the van der Waals attraction is a very short-ranged interaction. Hence, SiO_2-ST NPs will only feel the mutual attraction when they are very close to contact.

If a third particle gets close to the dimer, it will naturally tend to aggregate in the region nearby both particles. Indeed, the total attraction is larger due to the addition of the pairwise attractions of the third particle with both particles of the dimer (see Figure 5.5). Consequently, the particles tend to aggregate into an assembled state of particles with an isotropic structure for the three-particle system. With the subsequent aggregation of more colloids, it leads to the formation of compact isotropic clusters, very similar to the ones observed in the TEM micrographs, as shown in Figure 5.6.

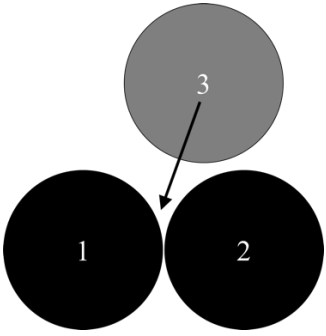

Figure 5.5 When a third particle (gray sphere) of SiO_2-ST approaches the dimer (black spheres), it tends to aggregate in the region nearby both particles of the dimer.

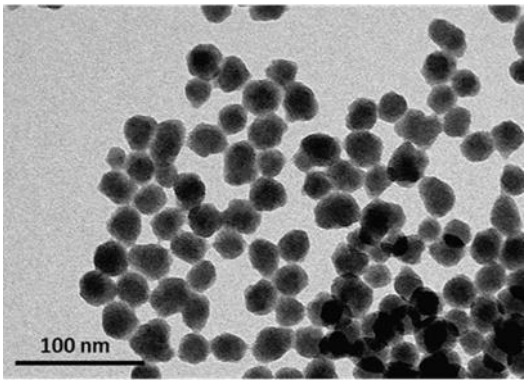

Figure 5.6 TEM micrograph of SiO_2-ST NPs showing the formation of clusters.

5.3.1.2. SiO_2 HNPs

For silica particles grafted with PB polymer chains, the pairwise interaction between two SiO_2-HNPs must include, in addition to the van der Waals attraction, the steric repulsion induced by the overlapping of the PB polymer chains when approaching the two HNPs. Considering a thickness of the polymer layer equal to δ, the steric repulsion splits in two additive contributions:

- Mixing interaction. It has an osmotic origin. It is caused by the interpenetration of the adsorbed polymer chains corresponding to each interacting surface. These chains "mix" in the region of overlap, generating a high density of polymer. Depending on the affinity between the polymer and the solvent, the solvent molecules can migrate toward or away from the region of overlap. In the case of a good solvent, the high concentration of polymer generates a flux of solvent molecules toward the overlapping region causing

the separation of the interacting particles (repulsion). This effect occurs as soon as the polymer shells of the approaching particles overlap, i.e., for a surface-surface interparticle distance *h* below twice the width of the adsorbed polymer layers, 2δ.

- Elastic interaction. It has an entropic origin. It results from the elastic compression of the adsorbed chains. This limitation of the available volume leads to a loss in the configurational entropy of the chains, which is most significant when $h < \delta$.

Hence, the potential is given by the sum of three components, as shown in Equation 5.7.

$$U_2(r) = U_{vdW}(r) + U_{mix}(r) + U_{el}(r) \tag{5.7}$$

At this point, we need analytic expressions for the mixing and elastic contributions. For this purpose, it will assume that the polymer shell has a uniform density, with a constant polymer volume fraction given by ϕ. The thickness of the polymer shell is δ = 3 nm as estimated from the SAXS analysis (see Paragraph 5.2).

The mixing interaction $U_{mix}(r)$ is given by Equation 5.8:[11]

$$\frac{U_{mix}(r)}{k_B T} = \begin{cases} \dfrac{4\pi a}{v_{THF}} \phi^2 \left(\dfrac{1}{2} - \chi\right)\left(\dfrac{h}{2\delta} - \dfrac{1}{4} - \ln\dfrac{h}{\delta}\right)^2 & 0 < h < \delta \\ \dfrac{4\pi a}{v_{THF}} \phi^2 \left(\dfrac{1}{2} - \chi\right)\left(\delta - \dfrac{h}{2}\right)^2 & \delta < h < 2\delta \end{cases} \tag{5.8}$$

where v_{THF} is the molar volume of the THF solvent. It can be obtained from its molecular weight and its density (Equation 5.9):

$$v_{THF} = \frac{\mathrm{MW}_{THF}}{N_A \rho_{THF}} = \frac{72.11\ \mathrm{g/mol}}{(6.023\times10^{23})(0.89\ \mathrm{g/cm^3})} = 0.135\ \mathrm{nm^3} \qquad (5.9)$$

χ denotes the Flory-Huggens of the polymer in the solvent. It provides an estimate of the solvent quality. The value of χ for PB polymers at 25 ºC is obtained from linear extrapolation of the values at 40 ºC and 100 ºC, leading to $\chi \approx 0.365$.

The polymer volume fraction in the shell, ϕ, is related to the surface density of chains attached to the SiO_2-ST NP, σ, by Equation 5.10:

$$\phi \simeq \pi s^2 \sigma \qquad (5.10)$$

where s is the average radius of the PB chain, of about $s \approx 0.3$ nm.

The elastic interaction comes into play for $h < \delta$, due to the deformation of the chains. For a polymer shell with uniform density, it is given by Equation 5.11:

$$\frac{U_{el}(r)}{k_B T} = \frac{2\pi a \delta^2}{v_{PBD}} \phi \left[\frac{h}{\delta} \ln\left(\frac{h}{\delta} \left(\frac{3 - h/\delta}{2} \right)^2 \right) - 6\ln\left(\frac{3 - h/\delta}{2} \right) + 3\left(1 - \frac{h}{\delta} \right) \right] \qquad 0 < h < \delta \qquad (5.11)$$

The molar volume of PB chains, v_{PBD}, is again obtained from the values of molecular weight and its density (Equation 5.12).

$$v_{PBD} = \frac{\mathrm{MW}_{PBD}}{N_A \rho_{PBD}} = \frac{3000\ \mathrm{g/mol}}{(6.023\times10^{23})(0.95\ \mathrm{g/cm^3})} = 5.24\ \mathrm{nm^3} \qquad (5.12)$$

It is important to note that both the mixing and elastic contributions are repulsive, and both increase with the polymer density. The elastic term grows linearly, $U_{el} \sim \phi$, whereas the mixing term scales with the square of the polymer density, $U_{mix} \sim \phi^2$. Consequently, an increase

of the polymer concentration of grafted chains can produce a significant increase of this repulsive force. For large enough ϕ, the steric repulsion can become so large that it even compensates the van der Waals attraction, leading to the so-called steric stabilization of the colloidal dispersion.

Figure 5.7 shows the total interaction pair potential between two SiO_2 HNPs together with the three contributions (mixing, elastic and van der Waals), calculated for a surface coverage of polymer of $\sigma = 0.03$ chains/nm^2 (this number corresponds to a total amount of 54 grafted chains per silica particle), which leads to a volume fraction of $\phi = 0.0151$.

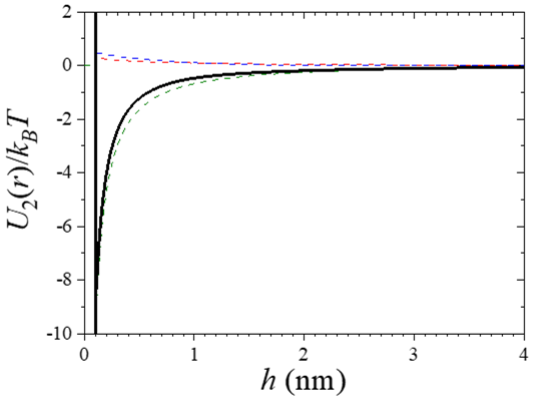

Figure 5.7 The plot shows the mixing contribution (pink dashed line), elastic (blue dashed line), van der Waals (green dashed line), and the total pair potential $U_2(r)$ between two PB-grafted SiO_2 HNPs.

As observed by comparison with Figure 5.4, the steric repulsion exerted by polymer shell reduces the range and strength of the particle-particle attraction. In particular, the depth of the potential minimum now equals $U_2 = -8.34k_BT$, while the second virial is given by $B_2^* =$

−10.83. Even though this attraction is weaker than the one obtained for uncoated SiO_2 NPs, it is still strong enough to induce the formation of stable clusters. We emphasize again that this potential has a very short interaction range.

Once the pairwise interaction has been described, the three-body additional steric repulsion of HNPs needs to be introduced. This repulsion depends on the angular orientation of the particles. As already discussed, the physical origin of this three-body interaction is due to the increase of polymer density in the region between two particles forming a dimer. This three-body term depends on the orientation of the particles forming the dimer. We define θ as the angle subtended by the line connecting the centers of two SiO_2-HNPs forming a dimer with the line connecting the position of the third particle, as shown in Figure 5.8.

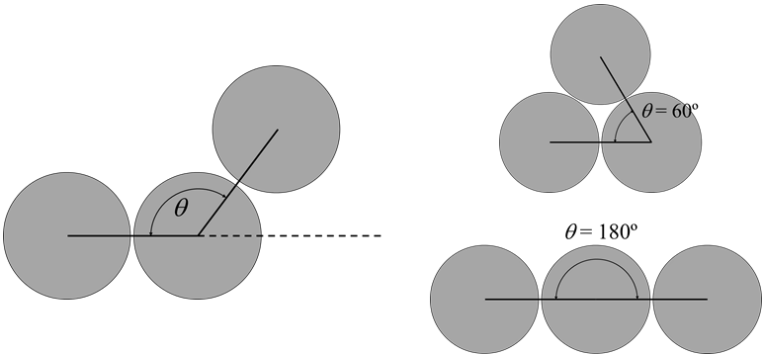

Figure 5.8 Orientation of the three SiO_2-HNPs forming a trimer.

In order to include the three-body repulsive interaction, the following simplified expression is proposed (Equation 5.13):

$$\frac{U_3(r_{12},r_{13},r_{23})}{k_BT}=\begin{cases}\Delta\left(\frac{2}{3}\right)^n(\cos\theta+1)^n & r_{12},r_{13}<r_c \text{ or } r_{12},r_{23}<r_c \text{ or } r_{13},r_{23}<r_c\\ 0 & \text{any other case}\end{cases} \tag{5.13}$$

where $\Delta > 0$ represents the energy cost of putting together the three SiO_2-HNPs in close contact, and r_c is the range of the three-body repulsion, which we chose $r_c = 1.1a$. Despite its simplicity, this expression gathers the most important physical features required to reproduce the observed structures:

1) U_3 is always repulsive and short-ranged, as expected for the short-range interactions between particles.

2) If one of the particles is separated by a distance larger that r_c, then we consider that these three particles are not forming a trimer, so $U_3 = 0$.

3) The maximum value of this potential is reached when $\theta = 60^o$, for which $U_3 = \Delta$. Therefore, creating an isotropic cluster has an additional energy cost (see illustration at the top right of Figure 5.8).

4) U_3 decreases to zero as the location of the third particle goes from $\theta = 60^o$ to 180^o. This interaction promotes the assembly into more linear asymmetric structures (chains). (see illustration at the bottom right of Figure 5.8).

5) Exponent n controls the decay of the three-body repulsion with the angle, θ. As observed from Figure 5.9, the decay of this repulsion is faster for larger values of n. Conversely, we obtain a slower decay of the range of U_3 by decreasing n below 1. For the particular choice of the polymer-grafted silica NPs with $a = 12$ nm and $\delta = 3$ nm, the polymer shell is rather small,

so we expect a short range three body interaction. We found that n = 8 represents this system fairly well.

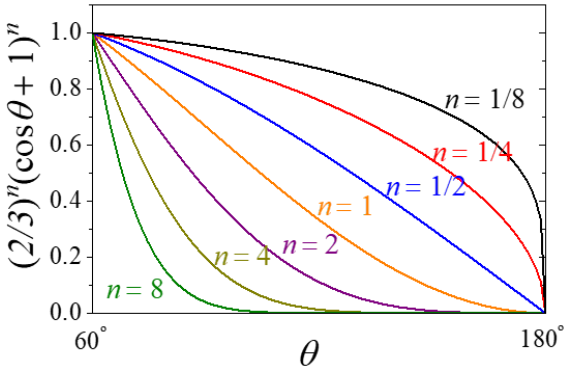

Figure 5.9 Angular dependence of the three-body contribution for different values of exponent n.

Finally, in order to simplify the simulations, we take advantage of the fact that the pair interactions have all a very short range compared to the particle size (see Figure 5.4 and Figure 5.7, where the range of the interactions do not extend more than 1 nm range). In this particular situation, particle interactions can be represented by the simple square-well potential (Equation 5.14):

$$\frac{U_2(r)}{k_B T} = \begin{cases} \infty & r < 2a + r_0 \\ -\varepsilon & 2a + r_0 < r < r_c \\ 0 & r > r_c \end{cases} \qquad (5.14)$$

where ε is the depth of the attractive well. In our calculation we fix r_c=2.1a, which corresponds to an interaction range of 1.2 nm between particle surfaces. Regarding ε, it is very important to emphasize that the value of ε cannot be chosen arbitrarily. It must be selected to

correctly represent the real particle-particle interaction, U_2. It orders to establish such correspondence, the normalized second virial coefficient B_2^* of the real U_2 and the one obtained from the square-well approximation must be the same.

- For naked silica NPs (B_2^*= −24.21) we find ε = 5.08.
- For grafted silica particles with 0.03 chains/nm^2 (B_2^* = −10.83) we find ε = 4.33.

Now we ready to describe the simulations and present the results, comparing them with the experimental data reported in Chapter 2 of this Thesis.

The experiments were performed at a mass fraction of silica particles of 5%. Knowing that the density of silica is 2.65 g/cm^3 and the density of THF is 0.889 g/cm^3, we found that the corresponding volume fraction of silica particles is ϕ_{part} = 0.0173.

5.3.2. Simulations

The replica-exchange Monte Carlo (REMC) method[12–14] was employed to obtain equilibrium configurations of our system as a function of the reduced temperature, T*=k_BT/ε. It is custom with simulations to fix ε and vary T* instead, but it must be noted that it produces the same result. A single run considers M = 16 cubic simulation cells containing N = 500 particles, with a fixed volume V so that the volume fraction of particles ϕ_{part} = $(4/3)\pi a^3 N/V$ equals 0.0173. The method sets different temperatures for each replica while considering swap trial moves. In other words, we perform 16 computer simulations at 16 different temperatures, so we have 16 replicas. In order to achieve the equilibrium between the 16 copies at different temperatures, the simulation procedure swaps temperature among

them. These trials allow the replicas to sample from an expanded ensemble defined in Equation 5.15:

$$Q_{expanded} = \prod_{i=1}^{M} Q_{NVT,i} \tag{5.15}$$

where $Q_{NVT,i}$ is the partition function of the ensemble at temperature T_i. By so doing, replicas at high temperatures travel long distances in configuration space, improving the sampling of the complete expanded ensemble. To guarantee the fulfillment of the detailed balance condition, the swap trials between replicas must have the following acceptance probability (Equation 5.16):

$$P_{acc} = \min\left\{1, e^{-(\beta_i-\beta_j)(U_i-U_j)}\right\} \tag{5.15}$$

where $U_i - U_j$ is the potential energy difference between replicas *i* and *j*, and $\beta_i - \beta_j$ the difference between the reciprocal temperatures of replicas *i* and *j* ($\beta = 1/(k_B T)$).

We start all simulation cells from randomly dispersed configurations and apply periodic boundary conditions for all directions. Verlet lists are considered to improve performance. In addition, we implemented a CUDA code where these neighbor lists are calculated by the GPUs, while the standard cores make the remaining calculations. Once the energy reaches a steady state, we proceed to capture some system snapshots. In this stage, we have only focused on this feature to try matching qualitatively the TEM images from the experimental system.

5.3.2.1. Results

T^* was varied in the range 0.1 to 0.3 by fixing ε=1.0 and the cutoff distance was set to r_c =2.1*a*. In addition, we explore Δ in the range 0

to 1.6. Δ represents the strength of the three-body energy repulsion between grafted silica particles. Two possible situations can be found:

1) $\Delta = 0$. In this case, the three-body interaction doesn't exist, so particles interact with purely pair-wise additive interactions. This is the case of naked SiO_2-ST NPs (without polymer coverage), which interact through a van der Waals attractive pair-wise potential.

2) $\Delta > 0$. This case corresponds to SiO_2-HNPs, having PB polymeric shell, leading to three-body repulsive interactions. As we already mentioned, the three-body interaction potential also depends on the exponent *n*. From Figure 5.2 and from the fact that $\delta/a = 0.25$, one may expect the three-body contribution to be important only for angles below $\theta < 100^o$. The value $n = 8$ represents quite well such behavior of the three-body repulsion for the experimental system. It is worth noting that *n* should decrease with increasing thickness of the polymer shell.

For the system in case 1), bare SiO_2-ST, the snapshots given in Figure 5.10 were obtained. The figure shows, from left to right, snapshots for T^*=0.3, 0.25, and 0.2, highlighting that an aggregation phenomenon occurs in all cases, but aggregates grow, and the population of monomers decreases from left to right. Note that $\varepsilon/k_BT = 1/T^*$, and so, one can think of fixing the temperature *T* and varying the well-depth ε.

According to the estimations from the theoretical analysis shown before, we expect the panel at the right of Figure 5.10 to behave as the experimental system, as it corresponds to $\varepsilon = 5$ (snapshot inside the red frame). In fact, the resemblance between the TEM images and the computer simulation is remarkable. However, differences between

experiments and simulations arise because in the simulations a perfectly monodisperse system is considered. It is well-known that attractive monodisperse systems crystalize at low temperatures, explaining the crystal-like shapes of our clusters that contrast with the less ordered structures shown by the TEM images (Figure 5.6).

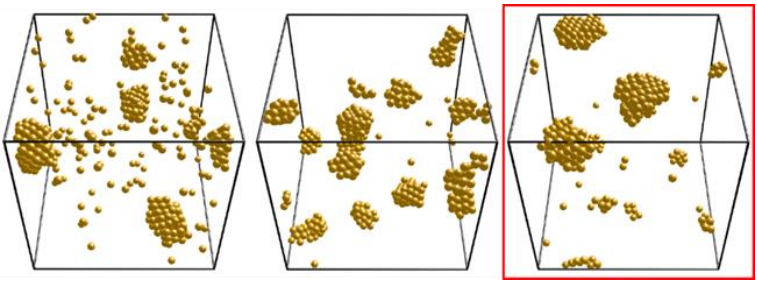

Figure 5.10 System snapshots at equilibrium for σ = 0 (bare SiO_2-ST). Temperature decreases from left to right, T^*=0.3, 0.25, and 0.2, which translates into well-depths of -3.33 k_BT, -4 k_BT, and -5 k_BT.

For the system in case 2) i.e. SiO_2 HNPs, the snapshots corresponding to Δ = 0.4 are reported in Figure 5.11. It should be noted that this Δ value hinders the formation of closed trimers, as they now have an energy of $-3+3\times0.4= -1.8k_BT$ to be compared with the $-2.0k_BT$ of a linear trimer (see the right panel of Figure 5.8). Besides, the $-1.8k_BT$ can be compared with the value $-3k_BT$ they had for Δ = 0. These changes have two important consequences.

First, aggregates turn much open and fractal-like than before, which can be corroborated by comparing the radial distribution function of the structures (not shown). Second, we need lower temperatures to grow clusters, since they are now based on single bonds contrasting with the multiple bond-forming bare systems. Note that a central

particle inside a crystallite can have up to 12 bonds when achieving an FCC or HCP structure, which strongly lowers the energy.

Conversely, open clusters can have a much smaller number of bonds. Hence, T^*=0.3 is not low enough to grow clusters and the system keeps outside the vapor-liquid (solid) binodal. Open structures are clearly observed at T^*= 0.23, which correspond to ε = 4.34. The assembled clusters are very similar to the aggregates observed in the TEM images (see snapshot inside the red frame, and the TEM picture in Figure 5.12). Larger aggregates appear only lowering the temperature at T^*= 0.15.

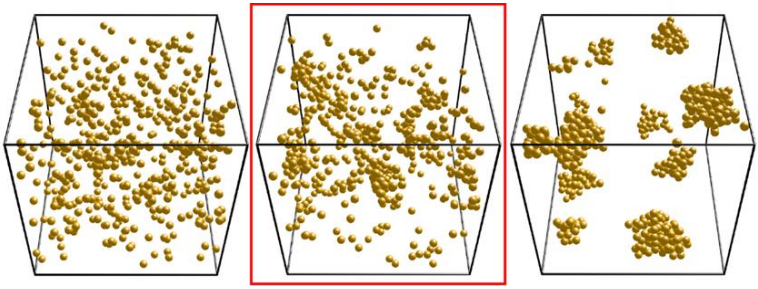

Figure 5.11 System snapshots at equilibrium for Δ = 0.4. Temperature decreases from left to right, T^*=0.3, 0.23, and 0.15, which translates into well-depths of -3.33 k_BT, -4.34 k_BT, and -6.7 k_BT.

Increasing Δ has little effect on the system structure because the clusters already grow by avoiding the formation of bond pairs forming less than 90º between them. Figure 5.13 shows equilibrium snapshots for systems with Δ = 1.0, which despite being much larger than Δ = 0.4, produces similar configurations at the same temperatures. Some differences can be highlighted. At T^*=0.3, the system is more monodisperse, at T^*=0.2 aggregates are a slightly smaller and more open, and at T^*=0.15 the system has more small oligomers (including

monomers), and clusters show some short fibrils. Further increasing the three-body repulsive strength (Δ) leads to no significant differences. To get a different system behavior one needs to decrease exponent *n*.

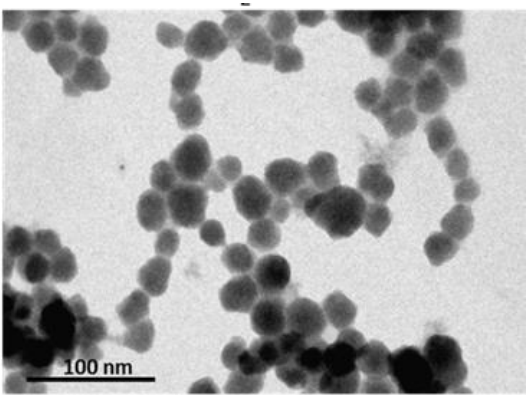

Figure 5.12 TEM micrograph of SiO_2-HNP_3, showing the self-assembly of HNPs in string-like structures.

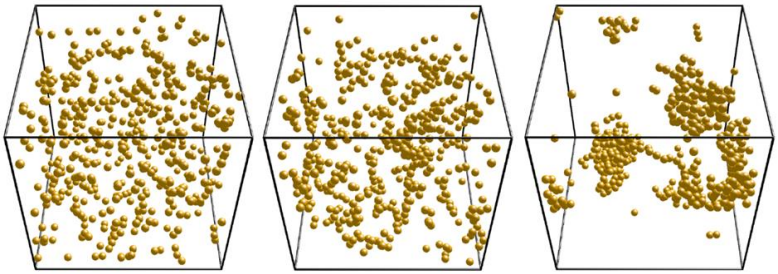

Figure 5.13 System snapshots at equilibrium for Δ = 1.0. Temperature decreases from left to right, T^*=0.3, 0.2, and 0.15, which translates into well-depths of -3.33 k_BT, -5 k_BT, and -6.7 k_BT.

Now let us consider a case in which the three-body contribution to the energy behaves as given by our U_3 function but with a smaller n value. Experimentally, this is expected to happen when increasing δ/a, i.e. with HNPs with smaller cores and larger polymer shells. Let us assume we can go as further as $n = 2$. This value, as shown in the graph in Figure 5.9, still shows significant contributions for bond-pair angles as large as 120º, and practically vanishes beyond 160º. Snapshots in Figure 5.14 illustrate the predicted behavior of this system. The figure depicts system snapshots for $r_c = 1.15(2a)$, $\Delta = 1.5$, and $n = 2$, for $T^* = 0.2$, 0.15 and 0.1. Here we observe that, upon aggregation, the particles align to form fibrils that ramify to form a percolating network (a gel). This behavior is similar to that found for low-valence patchy particles.

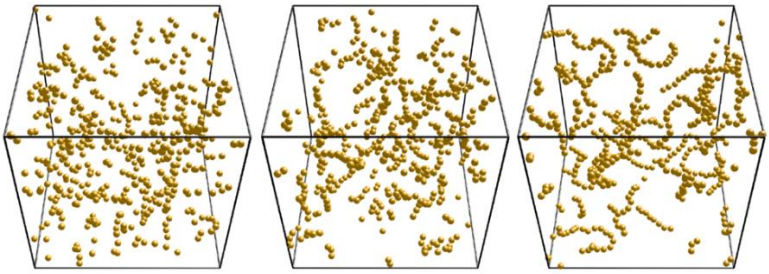

Figure 5.14 System snapshots at equilibrium for $\Delta = 1.5$ and a cutoff radius of $r_c=1.15(2a)=2.3a$. Temperature decreases from left to right, $T^*=0.2$, 0.15, and 0.1, which translates into well-depths of $-5k_BT$, $-6.7k_BT$, and $-10k_BT$.

5.4. Bibliography

1 P. Akcora, H. Liu, S. K. Kumar, J. Moll, Y. Li, B. C. Benicewicz, L. S. Schadler, D. Acehan, A. Z. Panagiotopoulos, V. Pryamitsyn, V. Ganesan, J. Ilavsky, P. Thiyagarajan, R. H. Colby and J. F. Douglas, *Nat. Mater.*, 2009, **8**, 354–359.

2 D. Meng, S. K. Kumar, J. M. D. Lane and G. S. Grest, *Soft Matter*, 2012, **8**, 5002.

3 A. J. Chancellor, B. T. Seymour and B. Zhao, *Anal. Chem.*, 2019, **91**, 6391–6402.

4 V. V. Ginzburg, *Macromolecules*, 2013, **46**, 9798–9805.

5 A. Chremos and J. F. Douglas, *Soft Matter*, 2016, **12**, 9527–9537.

6 A. Chremos, A. Z. Panagiotopoulos, H. Y. Yu and D. L. Koch, *J. Chem. Phys.*, 2011, **135**, 114901.

7 S. K. Kumar, N. Jouault, B. Benicewicz and T. Neely, *Macromolecules*, 2013, **46**, 3199–3214.

8 L. Tripaldi, E. Callone, M. D'Arienzo, S. Dirè, L. Giannini, S. Mascotto, A. Meyer, R. Scotti, L. Tadiello and B. Di Credico, *Soft Matter*, 2021, **17**, 9434–9446.

9 N. Bachhar, Y. Jiao, M. Asai, P. Akcora, R. Bandyopadhyaya and S. K. Kumar, *Macromolecules*, 2017, **50**, 7730–7738.

10 H. Koerner, L. F. Drummy, B. Benicewicz, Y. Li and R. A. Vaia, *ACS Macro Lett.*, 2013, **2**, 670–676.

11 B. Vincent, J. Edwards, S. Emmett and A. Jones, *Colloids and Surfaces*, 1986, **18**, 261–281.

12 A. P. Lyubartsev, A. A. Martsinovski, S. V Shevkunov and P. N. Vorontsov-Velyaminov, *J. Chem. Phys.*, 1992, **96**, 194110.

13 E. Marinari and G. Parisi, *Europhys. Lett.*, 1992, **19**, 451.

14 K. Hukushima and K. Nemoto, *J. Phys. Soc. Japan*, 2013, **65**, 1604–1608.

Conclusions

The precise control of the mechanical properties of rubber NCs is crucial to design materials not only highly performing but also increasingly sustainable in the perspective of a green rubber technology. These properties strongly depend on both the dispersion and distribution at the local scale of inorganic filler NPs within the rubber matrix, and thus on their morphological characteristics and interaction with the polymer matrix. It has been well-established that the self-assembly of anisotropic NPs in rubber NCs gives rise to organized domains with a consequent remarkable enhancement of reinforcement and consistent reduction of energy dissipation. On the other hand, the control of the distribution of spherical filler NPs in rubber NCs remains an open challenge.

In this framework, the aim of the present Thesis was to evaluate a new strategy for producing advanced rubber NCs , taking advantage of the self-assembly of SiO_2-based hybrid fillers. To address this challenge, the inspiration was to refer to a new class of hybrid building blocks, namely HNPs, consisting of SiO_2 functionalized with organic macromolecules. Therefore, the objectives were to: i) develop an efficient synthesis of SiO_2 HNPs having tunable size, controlled morphology, and tailored surface chemistry; ii) prepare highly-performing rubber NC based on SiO_2 HNPs as new functional fillers; iii) assess the self-organization effects of SiO_2 HNPs on the materials mechanical performance and finally iv) study their self-assembly behavior in correlation with the mechanical properties of rubber NCs.

The first part of the work, therefore, was dedicated to develop an efficient synthesis of SiO_2 HNPs, having a PB polymeric shell. To this end, a three-step grafting-to approach was devised. First, size- and shape-controlled colloidal SiO_2 NPs were prepared by a modified Stöber synthesis. The SiO_2 NPs were then functionalized with APTES, a short-chain aminosilane, which was used to anchor succinic anhydride-modified PB chains onto the surface of silica.

The obtained core-shell NPs were thoroughly characterized, confirming that the proposed SiO_2 HNPs preparation strategy is a simple and multi-gram scale synthesis, with an optimal control of surface chemistry and applicable to different kind of NPs and polymer shells, in particular rubbery polymers, rarely considered until now. Notably, by changing the concentration of polymer chains in the reaction mixture, SiO_2 HNPs with different grafting densities can be obtained. Morphological characterization by TEM, SEM and SAXS analysis also highlighted the spontaneous self-organization of SiO_2 HNPs in string-like anisotropic structures, both in matrix free conditions and in solvent cast cis-PB films.

To test the impact of NPs self-assembly on the mechanical properties, the synthesized SiO_2 HNPs were used to prepare rubber NC s in a typical tyre formulation. Bare, APTES-functionalized, and PB-coated silica NPs were mixed in a closed mixer with an SBR matrix. The resulting NCs, both uncured and cured, were subjected to dynamic mechanical analysis. NCs prepared with HNPs clearly showed increased reinforcement and reduced Payne effect as the PB coating was increased, highlighting the improvement of the filler-rubber interaction. Furthermore, the NC containing HNPs with intermediate grafting density showed the minimum degree of hysteresis compared to all other composites. Tensile tests showed increased rigidity of the NCs as the polymer shell density increased.

Morphological characterization of the cured NCs by TEM analysis enabled the correlation between the mechanical properties and self-assembly of filler NPs. In detail, bare SiO_2 NPs were highly aggregated while the particles functionalized with APTES showed no evidence of self-organization, although improved filler dispersion was observed. On the other hand, PB-grafted SiO_2 HNPs were shown to self-assemble in aligned anisotropic superstructures, although no external directing force was exerted. At each degree of grafting

density, the presence of string-like HNP superstructures was observed. Interestingly, a fraction of rubber was enclosed within the self-organized filler structures, which can be correlated to the improved rigidity and reduced hysteresis. This was further confirmed by the study of the NCs crosslinking density derived from swelling tests.

Successively, the applicability of the HNPs strategy to an easily scalable industrial system was tested. NCs were prepared on the basis of a technical formulation using commercial precipitated SiO_2 with an in-situ functionalization approach. In detail, a commercial macromolecular silane, namely MacroSil, was added in different proportions directly during the rubber mixing process to prepare "in-situ" HNPs. To compare the effect of MacroSil with that of a typical short-chain silane, TESPT was also added in varying proportions while keeping the total grafting density constant. These NCs showed mechanical properties in line with those expected for technical formulations. Interestingly, the presence of the macromolecular silane affected the tensile properties of the NCs by significantly increasing both elongation and stress at break compared to the reference NC containing only TESPT. The hardness and dynamic storage modulus of the cured NCs was also shown to increase with the grafting density of MacroSil. The nonlinear mechanical behavior of the uncured NCs at large strain was investigated by LAOS analysis. The results suggest that increasing the MacroSil coverage significantly improves the filler-rubber interaction by reducing the nonlinear effects due to filler-filler aggregation.

Lastly, the physical forces underlying the observed self-assembly of SiO_2 HNPs were investigated by devising a theoretical model. Crucial parameters for the formulation of the model were obtained from SAXS analysis of HNPs suspensions in THF. The model highlights that self-assembly of HNPs depends on PB grafting density and arises from a balance of attractive van der Waals forces and repulsive forces

resulting from elastic and mixing (osmotic) contributions. Interestingly, the experimentally observed string-like assembly behavior of SiO_2 HNPs may be explained based on three-body HNPs interactions. Monte Carlo simulations based on the model confirm the tendency of SiO_2 HNPs to self-organize in solution forming string-like structures, comparable to those observed in TEM analysis of both matrix-free HNPs and rubber NCs.

To sum up, the use of SiO_2 HNPs as new fillers in rubber NCs was shown to significantly improve the mechanical properties of the final materials, increasing reinforcement while reducing both hysteresis and Payne effect compared to typical short-chain coupling agents. The improvement of the mechanical properties was related to the self-organization behavior of HNPs, observable both in matrix-free conditions and in rubber matrices. This self-assembly behavior arises from a balance of attractive and repulsive interactions and may be controlled by tuning the surface chemistry of the HNPs.

These outcomes indicate the suitability of the adopted strategy based on self-assembly of HNPs as an effective approach for developing advanced functional rubber NCs. However, the relationship between NP spatial distribution and macroscopic properties remains not completely understood. Further work will be needed to solve this issue and lead to a quantum leap in the property improvements and to the more ubiquitous application of these materials.

Appendix A.
Characterization methods

In this Appendix, the main techniques used in this Thesis are described and the measurement conditions are illustrated.

A.1. Dynamic Light Scattering (DLS)

The morphology and dispersion of SiO_2-ST powders synthesized at different temperatures were investigated by DLS using a Malvern Zetasizer Nano S instrument on 100 ppm ethanol dispersions of the dried samples. The samples were ultrasonicated for 30 minutes before analysis and DLS measurements were carried out within 60 minutes from the preparation of the sample. Each curve is the average of three subsequent measurements with an equilibration time of 30 s. The resulting values of diameter and standard deviation were obtained from six experiments on the same specimen. The results of DLS analysis were provided as number-based distributions.

A.2. Scanning Electron Microscopy (SEM)

SEM analysis was used to investigate the morphology of SiO_2-ST, SiO_2-APTES and SiO_2-HNP_3 dry powders and to study the dispersion of SiO_2-ST, SiO_2-APTES and SiO_2-HNP_3 within solvent cast cis-PB films. The analysis was performed by a Zeiss Gemini SEM 500 microscope. The electron beam excitation was 10 kV at a beam current of 25 pA. For the analysis, 100 ppm dispersions of the powders in ethanol were deposited directly on the sample holder. Prior to SEM analysis, samples were gold sputtered. ImageJ processing program (Image Processing and Analysis in Java) was utilized to measure the size of NPs.

A.3. Thermogravimetric analysis (TGA)

TGA was employed to evaluate the surface functionalization of the SiO_2-ST, SiO_2-APTES and SiO_2-HNP_X (X=3, 4, 6), SiO_2-PS_HNP, SiO_2-PP_HNP powders by using a TGA/DCS1 STARe SYSTEM (Mettler Toledo). The thermal degradation profile of SiO_2-ST, SiO_2-

APTES and SiO_2-HNP_X was obtained from TGA under the following conditions: constant air flow (50 mL/min) and heating rate of 5 °C/min in the range 30–150 °C, constant air flow (50 mL/min) at 150 °C for 10 min, constant air flow (50 mL/min) and heating rate of 10 °C/min in the range 150–1000 °C. The 10 min interval at constant T = 150 °C was used to remove physisorbed water and solvents from the samples.

A.4. CHNS elemental analysis

CHNS elemental analysis was performed in a heating furnace (CHNS analyzer PerkinElmer Instruments) for the combustion of small amounts of the sample (few mg, up to 1000°C); in this technique, typically used for organic materials, the main elements of organic structures (carbon, nitrogen, oxygen and sulfur) are converted into volatile molecules, that are separated through gas- chromatography, identified and quantified. This measurement was used to evaluate the amount of surface ethoxy groups on bare SiO_2-ST NPs and, in combination with TGA, to evaluate the surface silanol density and degree of functionalization of the SiO_2-ST, SiO_2-APTES, SiO_2-HNP_X, SiO_2-PS_HNP and SiO_2-PP_HNP powders.

A.5. Attenuated Total Reflection Fourier-Transform Infrared Spectroscopy (ATR-FTIR)

Chemical surface modification of SiO_2-ST, SiO_2-APTES and SiO_2-HNP_3 was studied by ATR-FTIR, performed on a PerkinElmer Spectrum 100 instrument acquiring spectra with 1 cm^{-1} resolution in the 550-4000 cm^{-1} region. Each spectrum is the result of 16 subsequent scans. The transmittance of the reported spectra was normalized in the range 0-1. ATR-FTIR was used to confirm the effective functionalization of the powders.

A.6. Transmission Electron Microscopy (TEM)

The morphological characterization of SiO_2-ST, SiO_2-APTES, SiO_2-HNP_X, SiO_2-PS_HNP and SiO_2-PP_HNP, as well as of cis-PB solvent cast films containing SiO_2-ST, SiO_2-APTES and SiO_2-HNP_3, was carried out by High TEM using a JEOL JEM 2100+ equipped with a LaB6 cathode. Images were taken at different magnifications with the TEM operated in bright-field parallel imaging mode at 200 keV. TEM analysis was used to assess NPs sizes via ImageJ processing program and for a preliminary study of the NPs self-organization.

The morphological investigation of all cured rubber NCs was carried out by TEM using the Zeiss EM 900 microscope. Ultrathin slices (about 50 nm thick) of NCs were acquired with a Leica EM FCS cryo-ultramicrotome 254 equipped with a diamond knife, by maintaining the samples at -130°C. The thickness of the specimens was of about ~40 nm. TEM of the rubber NCs was used to study the distribution, dispersion and assembly behavior of filler NPs in the rubber matrix.

A.7. N_2 physisorption

N2 physisorption isotherms of SiO_2-ST, SiO_2-APTES and SiO2-HNP_3 powders were recorded at 77 K in a liquid N2 bath by using a MicroActive TriStar II Plus apparatus.

The specific surface area (SSA) was measured after evacuation of the samples at 100 °C for 12 h using the Brunauer-Emmett-Teller (BET) method.[1] The total pore volume was obtained from the maximal nitrogen adsorbed volume at p/p0 = 1 using

the instrument software. N_2 physisorption was used to evaluate the surface area of the samples and the microporosity. It was also used to investigate the presence of interparticle pores in bare functionalized NPs.

A.8. Gel Permeation Chromatography (GPC)

To characterize the PB oligomer used for the polymer shell in SiO_2-HNP_X, polydispersity index and R_g values were determined by Gel Permeation Chromatography (GPC) and reported in Fig. S1c. The analysis was carried out using a WATER 1515 isocratic HPLC Pump, a WATER 2414 refractive index detector, four Styragel columns (HR2, HR3, HR4, HR5). PB was dissolved in THF and its chromatograms were recorded with a flow of 1.0 mL/min at 35 °C. Calibration was performed with a PS standard (Merck).

A.9. Solid State Nuclear Magnetic Resonance Spectroscopy (SS-NMR)

SiO_2-ST, SiO_2-APTES and SiO_2-HNP_3 samples were characterized by SS-NMR using a Bruker 400WB spectrometer at a proton frequency of 400.13 MHz. Magic angle spinning (MAS) NMR spectra were obtained with cross polarization (CP) and single pulse (SP) sequences using the following experimental conditions. ^{13}C frequency: 100.48 MHz, contact time: 2 ms, decoupling length: 5.9 ms, recycle delay: 5 s, 2k scans. ^{29}Si frequency: 79.48 MHz, contact time: 10 ms, decoupling length: 6.3 ms, recycle delay: 10 s, 2k scans. Single pulse sequence: p/4 pulse 3.9 ms, recycle delay: 300 s, 2k scans. Samples were packed in 4 mm zirconia rotors, spun at 8 kHz under flow of air. External secondary references were adamantane and Q_8M_8. SS-NMR analysis was used to investigate the surface chemistry of the samples, confirm effective functionalization and evaluate the relative amounts of different surface silanol groups on the filler powders.

A.10. Small-Angle X-Ray Scattering (SAXS)

SAXS measurements of SiO_2-ST, SiO_2-APTES and SiO_2-HNP_X were conducted both on dry powders and 5 wt% THF dispersions with

an Incoatect X-Ray source IμS with Quazar Montel optics at a wavelength of 0.154 nm. The focal spot size diameter at the sample was 700 mm. Sample to detector distance was 1.6 m with an evacuated flight tube installed, yielding maximum resolution (d-spacing) of 120 nm. For detection of the 2D scattering patterns a CCD-Detector Rayonixt SX165 was used. The regular measurement time per sample was 20 min. The control software used was SPEC (ver. 5.32) by Certified Scientific Software, Cambridge, MA, USA. Since dry SiO_2-HNP_X consist of a three-phase system made of SiO2, PB coating and the surrounding voids, precise analysis was not achievable, because in general the SAXS analysis assumes the presence of a two-phase system with uniform electron density.[2,3] However, since the scattering difference between SiO_2 and the polymer is minimal with respect to the contrast with the voids (rC = 15.31 _ 10_6 Å_2; rSiO2 = 18.89 _ 10_6 Å_2),[4] the functionalized HNPs were treated as a single-phase body. The analysis and fitting of the SAXS data were carried out using Scatter (ver. 2.5) software.[5,6] The curves were modeled by combining a spherical form factor with a fcc structure factor component, originated by the NPs aggregation.

A.11. Dynamic oscillatory shear measurements

Dynamic mechanical properties of the cured and uncured rubber NCs were tested by strain sweep tests by using a Rubber Process Analyzer (RPA 2000, Alpha Technologies) in a shear stress mode. Each uncured sample was tested at 70 °C and 1.6 Hz, from 0.1% to 100% of elongation. The same specimen was then vulcanized at 170 °C for 30 minutes, during which the torque S was measured to acquire vulcanization the curves. The cured specimens were then tested again after cooling to 70 °C at 10 Hz from 0.1% to 10% of strain. Samples for RPA analysis were cut by using a Constant Volume Rubber Sample Cutter (CUTTER 2000, Alpha Technologies) with a

dimension of 3.5 cm diameter and 0.2 cm of thickness. The weight of the sample was maintained within the range of 5.0 ± 0.5 g.

A.12. Tensile tests

To acquire stress-strain curves of the cured rubber NCs at high deformation and to determine stress and elongation at break, tensile test was carried out on a Zwick/Roell model Z010 testing system. The cured samples were cut in dog bone specimens as shown in Figure A.1. The strain rate applied on the dog bone samples was 10 mm/min at 23 °C. For each sample, three specimens were tested.

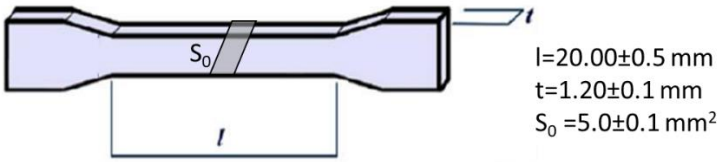

Figure A.1 Dog bone specimens used for tensile testing.

A.13. Swelling tests

Swelling experiments were performed to evaluate the cross-linking density in cured rubber NCs. Samples of 10x10x1 mm^3 were weighted to determine the initial mass m_0 and immersed in closed vessels filled with 10 mL of toluene at room temperature. The samples were swollen for 72 h, changing the solvent daily with fresh toluene to eliminate all the extracted fractions. At the end of the last day, the swollen sample was weighted to determine the mass of the swollen sample m_S. Then, the samples were dried for 24 hours at room temperature and weighted again to measure the mass of the dried samples (m_D). The volumetric

fraction of the swelled rubber V_R was calculated according to Equation A.1:

$$V_R = \frac{(m_D - f \cdot m_0) \cdot \rho_p^{-1}}{(m_D - f m_0) \cdot \rho_p^{-1} + m_{SO} \cdot \rho_s^{-1}} \quad \text{(A.1)}$$

where m_{SO} is the weight of the solvent in the swollen sample, $m_{SO} = m_S - m_D$), $\rho_p = 0.98$ g·cm^{-3} is the SBR density, $\rho_s = 0.87$ g·cm^{-3} is the toluene density and *f* is the fraction of the filler in the composites determined from TGA. Using this value, the cross-linking density ν (mol/cm^3) was evaluated according to the Flory-Rehner equation (Equation A.2):

$$\nu = \frac{ln(1 - V_R) + V_R + \chi \cdot {V_R}^2}{-2 \cdot \rho_p \cdot V_S \cdot {V_R}^{1/3}} \quad \text{(A.2)}$$

where VS = 105.91 is the molar volume of toluene and χ is the Flory solvent- polymer interaction term[7] equal to 0.49 for the toluene-SBR system.[8]

A.14. Measurements of compression modulus

Dynamic mechanical properties of scaled-up V10-SiO_2-TSX/SBR (X = 100, 90, 80, 70) NCs were evaluated by compression modules using a Instron dynamic device. Specimens with cylindrical shape (length = 25 mm and diameter = 14 mm) were pre-loaded in compression up to a longitudinal strain of 20% and maintained at a temperature of 70 °C. The samples were subjected to a dynamic sinusoidal strain of ±5.0 % in amplitude with respect to the length under pre-load at a frequency of 10 Hz. The dynamic mechanical properties are expressed in terms of dynamic elastic modulus (E'), loss modulus (E'') and tanδ.

A.15. Hardness measurements

Hardness measurements were performed following the IRHD procedure (ASTM D1415, ISO standard). In the IRHD method, hardness of the rubber NCs is obtained by penetration of a probe with specified dimension. The probe is tested under two conditions of contact with the rubber, namely with a small initial test force and with a larger force used for testing the sample. Difference in penetration of the probe in the two conditions is used as measurements of the rubber hardness.

A.16. Large-Amplitude Oscillatory Shear (LAOS) analysis

To study the large strain nonlinear behavior of the rubber NCs, the prepared samples were tested by Large Amplitude Oscillatory Shear (LAOS) analysis using the Rubber Process Analyzer (RPA 2000, Alpha Technologies) equipped for Fourier Transform (FT) Rheology. Uncured samples, cut with a Constant Volume Rubber Sample Cutter (CUTTER 2000, Alpha Technologies) with a dimension of 3.5 cm diameter and 0.2 cm of thickness, were tested at a constant temperature of 110 °C. Dynamic strain sweeps from 0.1% to 800% strain at a frequency of 0.5 Hz were performed.

A.17. Bibliography

1 S. Brunauer, P. H. Emmett and E. Teller, *J. Am. Chem. Soc.*, 1938, **60**, 309–319.

2 J. Scholz, B. Kayaalp, A. C. Juhl, D. Clemens, M. Fröba and S. Mascotto, *ACS Energy Lett.*, 2018, **3**, 387–392.

3 B. M. Smarsly, H. Kaper, S. Mascotto and C. Weidmann, *Chemie-Ingenieur-Technik*, 2010, **82**, 823–828.

4 S. Mascotto, D. Wallacher, A. Kuschel, S. Polarz, G. A. Zickler, A. Timmann and B. M. Smarsly, *Langmuir*, 2010, **26**,

6583–6592.

5 S. Förster, L. Apostol and W. Bras, *J. Appl. Crystallogr.*, 2010, **43**, 639–646.

6 S. Förster, A. Timmann, M. Konrad, C. Schellbach, A. Meyer, S. S. Funari, P. Mulvaney and R. Knott, *J. Phys. Chem. B*, 2005, **109**, 1347–1360.

7 P. J. Flory, *J. Chem. Phys.*, 1941, 9, 660–661.

8 A. J. Marzocca, *Eur. Polym. J.*, 2007, **43**, 2682–2689.